Emerging Nanophotonic Applications Explored with Advanced Scientific Parallel Computing

Xiang Meng

Submitted in partial fulfillment of the

requirements for the degree of

Doctor of Philosophy

in the Graduate School of Arts and Sciences

COLUMBIA UNIVERSITY

2017

ABSTRACT

Emerging Nanophotonic Applications Explored with Advanced Scientific Parallel Computing

Xiang Meng

The domain of nanoscale optical science and technology is a combination of the classical world of electromagnetics and the quantum mechanical regime of atoms and molecules. Recent advancements in fabrication technology allows the optical structures to be scaled down to nanoscale size or even to the atomic level, which are far smaller than the wavelength they are designed for. These nanostructures can have unique, controllable, and tunable optical properties and their interactions with quantum materials can have important near-field and far-field optical response. Undoubtedly, these optical properties can have many important applications, ranging from the efficient and tunable light sources, detectors, filters, modulators, high-speed all-optical switches; to the next-generation classical and quantum computation, and biophotonic medical sensors. This emerging research of nanoscience, known as nanophotonics, is a highly interdisciplinary field requiring expertise in materials science, physics, electrical engineering, and scientific computing, modeling and simulation. It has also become an important research field for investigating the science and engineering of light-matter interactions that take place on wavelength and subwavelength scales where the nature of the nanostructured matter controls the interactions.

In addition, the fast advancements in the computing capabilities, such as parallel computing, also become as a critical element for investigating advanced nanophotonic devices. This role has taken on even greater urgency with the scale-down of device

dimensions, and the design for these devices require extensive memory and extremely long core hours. Thus distributed computing platforms associated with parallel computing are required for faster designs processes. Scientific parallel computing constructs mathematical models and quantitative analysis techniques, and uses the computing machines to analyze and solve otherwise intractable scientific challenges. In particular, parallel computing are forms of computation operating on the principle that large problems can often be divided into smaller ones, which are then solved concurrently.

In this dissertation, we report a series of new nanophotonic developments using the advanced parallel computing techniques. The applications include the structure optimizations at the nanoscale to control both the electromagnetic response of materials, and to manipulate nanoscale structures for enhanced field concentration, which enable breakthroughs in imaging, sensing systems (chapter 3 and 4) and improve the spatial-temporal resolutions of spectroscopies (chapter 5). We also report the investigations on the confinement study of optical-matter interactions at the quantum mechanical regime, where the size-dependent novel properties enhanced a wide range of technologies from the tunable and efficient light sources, detectors, to other nanophotonic elements with enhanced functionality (chapter 6 and 7).

Contents

List of Figures

This page intentionally left blank

Acknowledgments

There have been many people who have walked alongside me during the past few years and I would like to thank every one of them. Foremost, I would like to give my sincerest thanks to my advisor, Prof. Richard Osgood, for his continuous support of my Ph.D. study, and for his passion, enthusiasm and immense knowledge that has deeply inspired me. I would also like to thank Prof. Nathaniel Osgood, not only for the great skills he taught me about computers, but also for the strong and solid bridge he built me to New York City. I feel incredibly fortunate to work with both Prof. Osgoods for their enlightenment and encouragement.

I would also like to thank the rest of my thesis committee: Prof. Irving Herman, Prof. John Kymissis, Prof. Christine Hendon and Dr. Nicholas Camillone, for their time, interest, and insightful comments. I am also deeply appreciated Nicolae Panoiu, Nicholas Camillone, Jerry Dadap and Svitlana Simoilina for their generous help on my research and academic life. Meanwhile, it was a great pleasure to meet all the fabulous colleagues at Columbia University over the unforgettable years and my life in New York City is full of joy and happiness with Stan Huang, Wencan Jin, Zhisheng Li, Sheng Wang, Datong Zhang and many other friends. At last, in looking forward to the moment which is intended to terminate my twenty-five years long career officially as a student, I must express my very profound gratitude to my parents and to my sister for providing me with unfailing support and continuous encouragement throughout all the years of my study, and beyond.

This page intentionally left blank

Dedication

To my beloved parents,

for their wisdom and open-mindedness.

謹以此書送給

我的爸爸，孟繁磊

爲他的智慧與廣闊的視野

我的媽媽，馬桂菊

爲她的體貼與細膩的感情

This page intentionally left blank

Chapter 1

Introduction

1.1 Nanophotonics

Recent advances have enabled the fabrication and characterization of nanometer scale photonic devices that allow us to concentrate and channel light on length scales much smaller than the wavelength of the light. In the meantime, the fast improvements in computing and simulation platforms also provide us a superior environment for the rapid and accurate design and development. In this chapter, we first provide an overview of the properties of surface plasmons, followed by a brief review of important plasmon-based nanophotonic applications. We also briefly review important technological advances in the fields of nanofabrication that provide the foundation for realizing the nanophotonic applications reported in this dissertation.

Surface plasmons (SP) or plasmonics is a very important concept in the field of nanophotonics, where we are concerned primarily with the manipulation of light at the nanoscale. Surface plasmons are essentially light waves that are trapped on a surface of a conductor due to their interaction with free electrons near the surface. In this interaction, the free electrons respond collectively by oscillating in resonance with the light wave. The resonant interaction between the surface charge oscillation and the electromagnetic field of the light constitutes the SP and gives rise to its unique properties [1]. The surface plasmon has a propagation vector parallel to the interface, while its amplitude decays exponentially in the direction orthogonal to the surface. Unlike pure electromagnetic waves, surface plasmons can be localized to

subwavelength dimensions in the plane perpendicular to the propagation direction, providing a viable route to nanoscale optics. Much of today's research is aimed at structures that provide additional localization, such as localized surface plasmons of single metal particles [2] or between metal particles [3]. Localization of the electromagnetic fields at the nanoscale also yields a dramatic increase in the field intensity, thus suggesting the use of surface plasmons in application, such as photoluminescence enhancement of quantum emitters [4], Raman spectroscopy of single molecules [5] and atomic clusters [6], and even coherent control of a single molecule quantum dynamics [7]. Nanophotonic applications based on the use of surface plasmons can be applied for a large variety of tasks, through the design and manipulation of the geometry of metallic structures, and consequently their specific plasmon-resonant or plasmon-propagating properties.

1.2 Scope of the Thesis

Rigorously, the plasmon is the quasi-particle resulting from the quantization of plasma oscillations, a hybrid of the electron plasma and the photon. Although plasmons are quantum mechanical in nature, their properties, most specifically with respect to their coupling to light, can be described rigorously by classical electrodynamics. Detailed methods for analyzing the properties of surface plasmons are discussed in Chapter 2. While many metals support surface plasmons, gold and silver have thus far dominated experimental work due to their low ohmic loss at the operating wavelength. With the unique properties of surface plasmons, several key research directions have been established in this dissertation. These applications range from the enhanced near-field optics for sensing and detection of biomolecules [8, 9], to scanning microscopies employing metallic probe tips [10], to enhanced photoluminescence processes in solid-state lasers [11], modulators and detectors [12], to the propagation

of signals and information on metal-based waveguides [13]. In this dissertation, three main categories of plasmon-based nanophotonic applications are reported.

Surface Plasmon Enhanced Fluorescence and Sensing The excitation of conduction electrons by light is denoted as a surface plasmon resonance for planar surfaces or localized surface plasmon resonance for nanometer-sized metallic structures. The plasmon resonant frequency is determined by the dielectric properties of the metal, and specifically for nanoscale metallic structures by the size, shape, and local environment of the nanostructure. On the other hand, fluorescence is the emission of photons as a quantum emitter relaxes from an excited electronic state to the ground state. The presence of a vicinal metallic nanostructure to a quantum emitter strongly influences both the radiative and nonradiative decay of the quantum emitter and its lifetime. In Chapters 3 and 4, we discuss their influence on the radiative rate, nonradiative decay rate, and lifetime of the quantum emitters. Specifically, we address the distance dependence of these characteristics on wavelength and from shape of the metal nanostructures. Our results point the way to nanoantenna engineering, offering new ways to increase the intensity of low-quantum-yield quantum emitters and improve fluorescence stability in biological imaging. In addition, the wavelength shift of the plasmon resonance is a good figure-of-merit criterion for sensing applications, which monitor changes of the refractive index of the environment surrounding the metal nanoparticles. Furthermore, the high sensitivity that can be achieved through the design principles we illustrate can be used to advantage for real-time detection of binding events studied using localized surface plasmon resonance spectroscopy.

Surface-Enhanced Spectroscopy Recent advances have pushed high-spatial-resolution surface probes into picosecond and femtosecond regimes [14], however, an approach that can be applied generally to surface physics and chemistry investigations remains to be developed. A two-photon-photoemission-based approach has the potential to address this need with the field enhancement at the metallic tip and

surface. When an electromagnetic wave interacts with a metallic surface or a metallic tip, the electromagnetic fields in the vicinity of the surface are greatly enhanced as compared to the incident electromagnetic field. This phenomenon has been attributed to the excitation of surface plasmons at the metallic interface. In Chapter 5, we report on our recently developed photoemission technique based on this phenomenon that is a significant step toward joint subnanometer subpicosecond surface imaging. This work breaks new ground by establishing conditions where photocurrents depend exponentially on the tip–surface gap width and by correlating the signal to field enhancements in the gap.

Plasmon-Based Active Devices Going beyond the passive applications, active generation, amplification and modulation can also be done based on surface plasmons. Enhancing the performance of ultracompact solid-state light sources is of great current importance due to concerns for integrated on-chip photonic devices. For mid-IR detectors or modulators, reducing the volume of the semiconductor sensing element also has the important effect of reducing the thermal noise. Using the intensely concentrated plasmonic near-field, it is possible to concentrate light from a large area to enhance absorption by a small volume of material. In Chapter 6, we describe development of a theoretical model to design a direct bandgap optically-pumped nanophotonic integrated laser. Our device utilizes a gap-surface-plasmon optical mode to achieve subwavelength optical confinement in conjunction with a monolayer transition-metal dichalcogenide semiconductor as the active medium. In Chapter 7, we also provide an experimental demonstration of a modulation based on plasmon from graphene nanoribbon. Note that the plasmon frequency of graphene easily extends into the terahertz, which opens up the possibility of creating a variety of devices, and the possibility for nanoscale high-speed devices.

1.3 References

[1] W. L. Barnes, A. Dereux, and T. W. Ebbesen, "Surface plasmon subwavelength optics," *Nature (London)*, vol. 424, no. 6950, pp. 824–830, 2003.

[2] S. A. Maier and H. A. Atwater, "Plasmonics: Localization and guiding of electromagnetic energy in metal/dielectric structures," *J. Appl. Phys.*, vol. 98, no. 1, p. 10, 2005.

[3] P. Nordlander, C. Oubre, E. Prodan, K. Li, and M. Stockman, "Plasmon hybridization in nanoparticle dimers," *Nano Lett.*, vol. 4, no. 5, pp. 899–903, 2004.

[4] K. Okamoto, I. Niki, A. Shvartser, Y. Narukawa, T. Mukai, and A. Scherer, "Surface-plasmon-enhanced light emitters based on ingan quantum wells," *Nat. Mater.*, vol. 3, no. 9, pp. 601–605, 2004.

[5] S. Nie and S. R. Emory, "Probing single molecules and single nanoparticles by surface-enhanced raman scattering," *Science*, vol. 275, no. 5303, pp. 1102–1106, 1997.

[6] P. L. Stiles, J. A. Dieringer, N. C. Shah, and R. P. Van Duyne, "Surface-enhanced raman spectroscopy," *Annu. Rev. Anal. Chem.*, vol. 1, pp. 601–626, 2008.

[7] M. S. Tame, K. McEnery, Ş. Özdemir, J. Lee, S. Maier, and M. Kim, "Quantum plasmonics," *Nature Phys.*, vol. 9, no. 6, pp. 329–340, 2013.

[8] X. Meng, H. Yang, R. R. Grote, J. I. Dadap, N. C. Panoiu, and R. M. Osgood, "Designer metal-nanoantennae/dye complexes for maximum fluorescence enhancement," in *SPIE Nanoscience+ Engineering*, pp. 95473B–95473B, International Society for Optics and Photonics, 2015.

[9] X. Meng, R. R. Grote, J. I. Dadap, N. C. Panoiu, and R. M. Osgood, "Engineering metal-nanoantennae/dye complexes for maximum fluorescence enhancement," *Opt. Express*, vol. 22, no. 18, pp. 22018–22030, 2014.

[10] X. Meng, J. I. Dadap, N. Camillone, and R. M. Osgood, "Plasmonic enhancement for two-color ultrafast time-resolved photoemission," in *JSAP-OSA Joint Symposia*, p. 14a_C302_5, Optical Society of America, 2016.

[11] X. Meng, R. R. Grote, W. Jin, J. I. Dadap, N. C. Panoiu, and R. M. Osgood, "Rigorous theoretical analysis of a surface-plasmon nanolaser with monolayer mos 2 gain medium," *Opt. Lett.*, vol. 41, no. 11, pp. 2636–2639, 2016.

[12] Y. Li, H. Yan, D. B. Farmer, X. Meng, W. Zhu, R. M. Osgood, T. F. Heinz, and P. Avouris, "Graphene plasmon enhanced vibrational sensing of surface-adsorbed layers," *Nano Lett.*, vol. 14, no. 3, pp. 1573–1577, 2014.

[13] X. Meng, A. Ahmed, J. Dadap, K. Bergman, and R. Osgood, "Dispersion engineering of silicon/plasmonics hybrid optical interconnections," in *Integrated Photonics Research, Silicon and Nanophotonics*, pp. IW2A–2, Optical Society of America, 2015.

[14] H. Petek, "Photoemission electron microscopy: Photovoltaics in action," *Nat. Nanotechnol.*, vol. 12, no. 1, pp. 3–4, 2017.

Chapter 2

Numerical Methods

2.1 Numerical Methods in Nanophotonics

Due to the complex nature of the light wave interaction and the ultra-small scale of the photonic components, analytical solutions of the Maxwell′s equations in most cases may not exist. Thus experimental studies rely heavily on numerical analysis to provide guidance both for the design of the photonic components as well as for the interpretation of their performance prior to fabrications. In most cases, one should first develop a quantitative theoretical description of the photonic systems using advanced computational techniques, which requires solving the corresponding partial differential equations numerically. In a broad sense, there are two categories of modeling methods: *finite-difference* method and *finite-element* method, as well as two categories of equation solving techniques: *frequency-domain* solver, and *time-domain* simulations. In this section, we briefly present an overview of the modeling methods and solving techniques.

2.1.1 Finite-Difference vs. Finite-Element

In mathematical modeling, finite-difference methods (FDM) are popular methods for solving differential equations by approximating them with difference equations and using finite difference grids to approximate the derivatives. Due to the simple discretization process, the development time for FDM is very short and it is easily understandable and directly follows from the differential equations. The stability

and dispersion and inhomogeneous characteristics also follow from a simple, intuitive understanding of the updating procedure. However, the orthogonal grid structure of the FDM results in the edges of the model structures have stair-stepped edges, which can become a problem when high accuracy is desired and curved surfaces are involved. Some special treatments have been developed to overcome this limitation, including non-uniform grids, but other methods, such as finite-element method, are generally better suited for complex irregular geometries.

The finite-element method (FEM) subdivides a large problem into smaller, simpler parts that are called finite elements, which are based on triangular or tetrahedral subregions. The simple equations that model these finite elements are then assembled into a larger system of equations that models the entire problem. FEM then uses the variational methods to approximate a solution by minimizing an associated error function. Note that developing a FEM is not as straightforward as FDM. For example, creating the numerical grid along for FEM could require an entire software package, and understanding of the discretization procedure can be quite convoluted.

2.1.2 Time-Domain vs. Frequency-Domain

The solution based on the time-domain can be computed by time stepping, whereas the problem in the frequency-domain can be solved only through a linear system of equations. Using the time-domain solver, the time step at which we advance the solution is limited by the spatial size. Thus for simulations with large spaces, the simulation must be run for a very long time. On the other hand, frequency-domain solvers are generally required linear algebra or matrix inversions, so that there is an inherent limit to the size of a simulation, especially for a large three dimensional systems.

The popular numerical methods for solving Maxwell′s equations or the wave equation are mainly the combinations of the discretization methods and solving techniques,

as illustrated in Fig. 2.1, namely, Finite-Difference Time-Domain (FDTD), Finite-Difference Frequency-Domain (FDFD), Finite-Element Frequency-Domain (FEFD) and Finite-Element Time-Domain (FETD). In this following chapter, we will provide a brief overview of each major techniques used in photonics design with an illustration of its use.

2.2 Finite-Difference Time-Domain Method

Finite-difference time-domain (FDTD) is a well-known numerical technique in electrodynamics to compute the Maxwell′s equations. It translates the differential form of Maxwell′s equations into difference equations that can be solved numerically by computer. However, before the 1990s, the FDTD method was limited by the need to discretize the simulation space on sub-wavelength scales, with relatively small time steps. Thus, a typical photonics modeling would require a large amount of computer memory that exceed the technology limits at that time. However, since the 1990s, the FDTD became more affordable with the fast increases in computer memory and speed.

There are several advantages for using FDTD. First, the method is accurate and robust, such that approximations are minimized and detailed solutions are provided with accuracy determined by the grid resolution. Second, the method is naturally includes the effects such as polarization, dispersion, and nonlinearities. Furthermore, FDTD is able to calculate the full-wave response, which includes the transient behavior of an electromagnetic system.

In this section, we first introduce Yee′s unique, yet highly powerful, FDTD scheme for solving Maxwell′s equations. Taking the advantage of the simplicity of one-dimensional problems, we demonstrate the basic principle and formulation of the FDTD method for analysis of electrodynamic problems. We then discuss stability

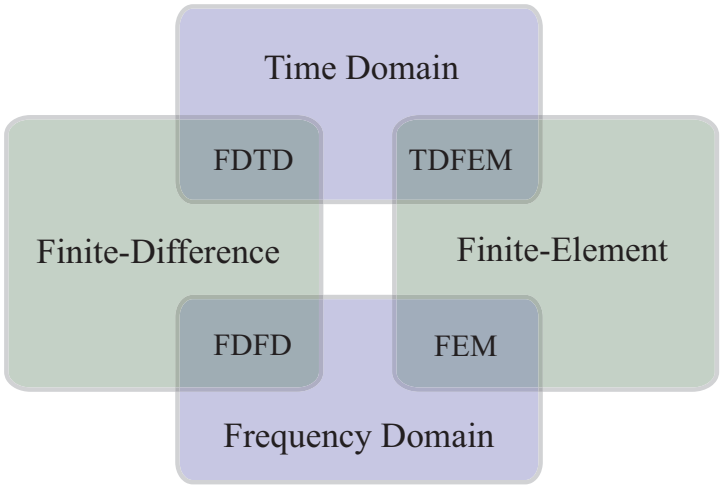

Figure 2.1: The different numerical methods for solving the electromagnetic problems.

analysis, boundary conditions and extensions to the analysis of 2D/3D problems.

2.2.1 Yee′s algorithm

Yee′s algorithm, introduced in 1966, established a set of finite-difference equations for the time-dependent Maxwell′s curl equations system [1]. In this algorithm, the continuous derivatives in space and time are approximated to second-order accuracy with two-point centered difference forms. The resulting finite-difference equations are solved in a leapfrog manner: the electric field vector components in the modeled space are solved at a given instant in time; then the magnetic field vector components in the same spatial volume are solved at the next instant in time using the previously stored electric field data. This process is repeating until the desired transient or steady-state electrodynamic behavior is full evolved.

The fundamental unit of the 3D grid, known as the Yee lattice, is shown in Fig. 2.2, which discretizes and solves the six components of E and H fields that satisfy the six coupled scalar Maxwell curl equations in free space:

$$\begin{aligned}
\frac{\partial E_x}{\partial t} &= \frac{1}{\epsilon_0}\left(\frac{\partial H_z}{\partial y} - \frac{\partial H_y}{\partial z}\right) \qquad \frac{\partial H_x}{\partial t} = \frac{1}{\mu_0}\left(\frac{\partial E_y}{\partial z} - \frac{\partial E_z}{\partial y}\right) \\
\frac{\partial E_y}{\partial t} &= \frac{1}{\epsilon_0}\left(\frac{\partial H_x}{\partial z} - \frac{\partial H_z}{\partial x}\right) \qquad \frac{\partial H_y}{\partial t} = \frac{1}{\mu_0}\left(\frac{\partial E_z}{\partial x} - \frac{\partial E_x}{\partial z}\right) \\
\frac{\partial E_z}{\partial t} &= \frac{1}{\epsilon_0}\left(\frac{\partial H_y}{\partial x} - \frac{\partial H_x}{\partial y}\right) \qquad \frac{\partial H_z}{\partial t} = \frac{1}{\mu_0}\left(\frac{\partial E_x}{\partial y} - \frac{\partial E_y}{\partial x}\right)
\end{aligned} \tag{2.1}$$

Rather than solving for the electric field alone with a wave equation, the Yee algorithm solves the coupled Maxwell′s curl equations directly. In which way, both electric and magnetic material properties can be modeled in a straightforward manner. This is especially important when modeling the inhomogeneous materials and a full-wave response of a dispersive medium.

Here we demonstrate an example of using finite-difference method to calculate the fundamental TE mode profile of a channel waveguide. In details we illustrate

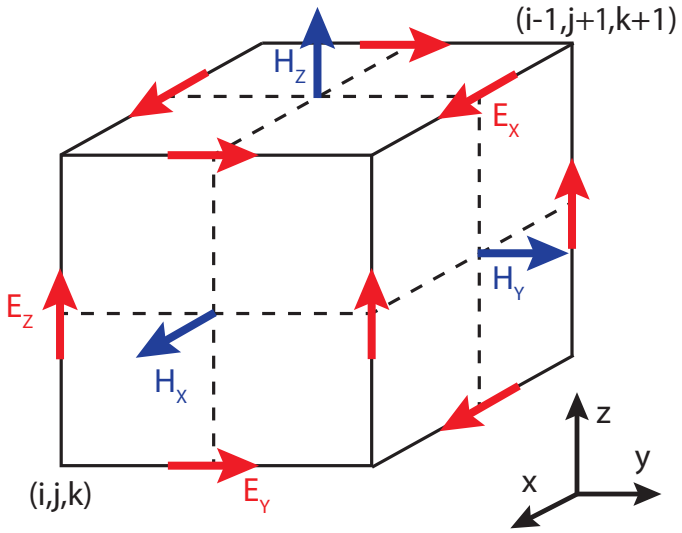

Figure 2.2: Position of electric and magnetic vector components in a 3D staggered unit cell known as Yee lattice. The vectors are placed at the point in the mesh at which they are defined and stored.

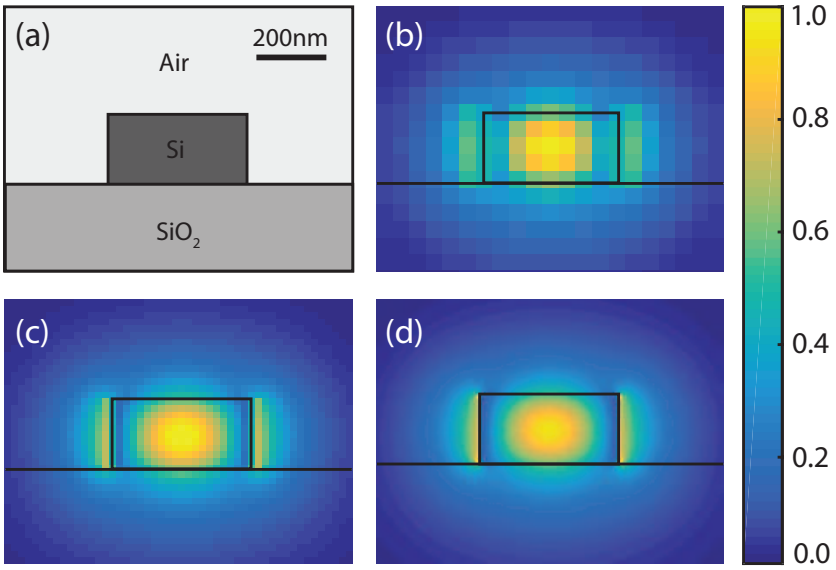

Figure 2.3: Demonstration of the calculated mode profile with different computing grid size: (a) The structure of a Si channel waveguide (*400nm* in width and *200nm* in height) on top of the SiO_2 substrate. The fundamental TE mode profile was calculated using different grid size of (b) *50nm*, (c) *20nm*, and (d) *5nm*.

how the computing grid size can affect the calculated mode profile. Figure 2.3(a) shows the structure we calculated with a Si channel waveguide sitting on top of the SiO_2 substrate. The channel waveguide is 400nm in width and 200nm in height. Figure 2.3(b)-(d) shows the calculated TE mode profile with difference grid size of 50nm, 20nm, and 5nm respectively.

2.2.2 FDTD: 1D Example

In this section, we demonstrate the basic implementation of FDTD method in one-dimensional case, with details on discretization of the Maxwell′s Equations. To solve a specific problem of pulse propagation, we demonstrated a 1D model with details on discretization of Maxwell equation. Taking the advantages of the simplicity of 1D example, we also illustrate the stability criterion for the FDTD simulations. This discretized equation and stability criterion can be easily expanded to 2D and 3D models.

In one dimension model, the medium extends to infinity in the y-direction and z-direction. This translational symmetry then leads to $\frac{\partial}{\partial x} = \frac{\partial}{\partial y} = 0$. For a free space situation, the Maxwell′s curl equations take the form:

$$\frac{\partial H_z}{\partial t} = -\frac{1}{\mu_0}\frac{\partial E_y}{\partial x} \quad \text{and} \quad \frac{\partial E_y}{\partial t} = -\frac{1}{\epsilon_0}\frac{\partial H_z}{\partial x} \tag{2.2}$$

In order to introduce 1D Yee discretization, we use the following notation:

$$\begin{aligned} E_y(m \cdot \Delta x, n \cdot \Delta t) &\equiv (E_y)_m^n \\ H_z(m \cdot \Delta x, n \cdot \Delta t) &\equiv (H_z)_m^n \end{aligned} \tag{2.3}$$

where m and n are the index of the spatial and temporal grid. Using the central-difference approximation with second-order accuracy for space and time derivatives, the equations can be discretized as:

$$\begin{aligned} \frac{(E_y)_m^{n+\frac{1}{2}} - (E_y)_m^{n-\frac{1}{2}}}{\Delta t} &= -\frac{1}{\epsilon_0}\frac{(H_z)_{m+\frac{1}{2}}^n - (H_z)_{m-\frac{1}{2}}^n}{\Delta x} \\ \frac{(H_z)_{m+\frac{1}{2}}^{n+1} - (H_z)_{m+\frac{1}{2}}^n}{\Delta t} &= -\frac{1}{\mu_0}\frac{(E_y)_{m+1}^{n+\frac{1}{2}} - (E_y)_m^{n+\frac{1}{2}}}{\Delta x} \end{aligned} \tag{2.4}$$

In practical sense, for a simplicity of the calculations, the constants from physical laws are typically omitted from mathematical expressions. The implementation of FDTD usually adapts the natural unit of the speed of light c, which is exactly dimensionless 1, i.e., $c = 1/\sqrt{\epsilon_0 \mu_0} \equiv 1$. By redefining the electric field as $E_y \equiv \sqrt{\epsilon_0/\mu_0} E_y$, Eq. 2.4 can be expressed as:

$$\begin{aligned} (E_y)_m^{n+\frac{1}{2}} &= (E_y)_m^{n-\frac{1}{2}} - \frac{\Delta t}{\Delta x}[(H_z)_{m+\frac{1}{2}}^n - (H_z)_{m-\frac{1}{2}}^n] \\ (H_z)_{m+\frac{1}{2}}^{n+1} &= (H_z)_{m+\frac{1}{2}}^n - \frac{\Delta t}{\Delta x}[(E_y)_{m+1}^{n+\frac{1}{2}} - (E_y)_m^{n+\frac{1}{2}}] \end{aligned} \tag{2.5}$$

Figure 2.4 is the visual illustration of Eq. 2.5, which indicates the numerical dependencies in the 1D FDTD formulations. One can observe that the value of a field at any point is determined by three previous values: two from the neighbors of opposite field at the previous half time step; one from the same position at the previous one time step.

Note that this discretization procedure can be easily extended into 2D and 3D space [2]. However, for example, if 3D problem would require N grid cells in each dimension, the total grid cells are N^3. With a minimum of six fields to compute in double precisions, it can easily take GB of memory with billions of operations. Thus FDTD is relatively a computationally intensive method. However, advances in CPU speed and memory and the emergence of inexpensive parallel systems with parallel computing technology are enabling a full 3D FDTD simulation without any constraints.

Stability criterion. Despite the requirements for spatial grid size in order to maintain the numerical accuracy, the time step must be small enough so that it satisfies the Courant condition [3] in order to achieve a convergence while solving partial differential equations numerically. The detailed mathematical discussion can be found in [4]. The physical fact of the stability criterion is that the speed of numerical propagation should not exceed the physical speed. Thus the lattice speed $\Delta x/\Delta t$ must

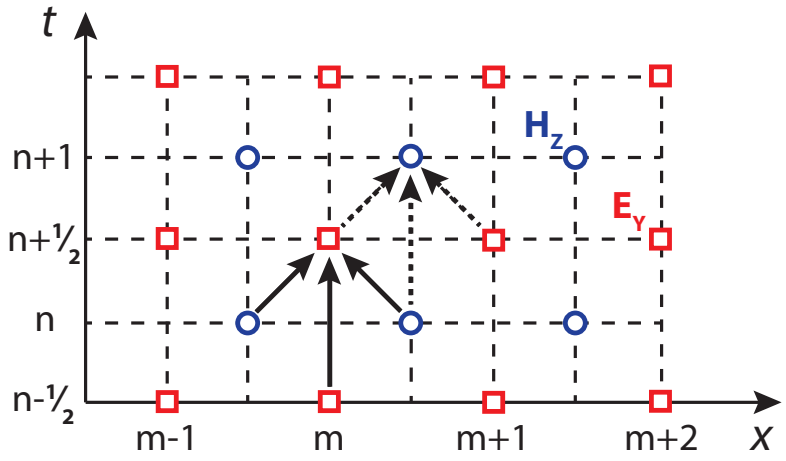

Figure 2.4: Visual illustration of the numerical dependencies in the 1D FDTD method.

be less than the physical velocity v_p in the medium with refractive index of n, where $v_p = c/n$. A summary of stability criteria for various dimensions are presented in Table 2.1.

2.2.3 Boundary Conditions

One of the major challenges of using the FDTD method for solving unbounded electromagnetic problems is to employ a finite computational domain. Thus our simulation domain must be terminated with proper boundary conditions. This termination can be accomplished by introducing an artificial layer to enclose the domain of interest. However, to duplicate the original open-space environment, the artificial boundary layer must absorb the field incident on the layer to eliminate all reflected fields. There are a few approaches to achieve this implementing a mathematical boundary condition (i.e., absorbing boundary condition) or a fictitious absorbing material layer (perfect matching layer).

Absorbing Boundary Condition. An absorbing boundary condition (ABC) is a mathematical technique to approximately estimate the missing field outside the FDTD domain, thus emulating an infinite space. This is normally done by assuming a plane wave incidence. Unfortunately, in many cases, the incident wave at the boundary is usually not a plane wave and furthermore, the angle of incidence is not known a prior. Thus ABC is a general approximation and does not completely prevent reflections back into the FDTD space. Advance treatment is available, such as decomposing an arbitrary wave into many component plane waves. For reader with interests, please refer to [5].

Perfectly Matched Layer. Instead of using a mathematical boundary condition, one can design thin layers of artificial absorbers solely for simulation purpose. A popular absorber model was proposed by Berenger [6] for the FDTD simulation and is known as the perfectly matched layer (PML). A PML is an artificial material that is

Table 2.1: Stability Criterion for FDTD.

Dimensionality	Criterion
1D	$v_p \Delta t \leq \Delta x$
2D	$v_p \Delta t \leq (\frac{1}{\Delta x^2} + \frac{1}{\Delta y^2})^{-\frac{1}{2}}$
3D	$v_p \Delta t \leq (\frac{1}{\Delta x^2} + \frac{1}{\Delta y^2} + \frac{1}{\Delta z^2})^{-\frac{1}{2}}$

theoretically designed to create no reflections regardless of the frequency, polarization and angle of incidence of a plane wave incident upon its interface. The frequency independence is especially important because it enables broadband simulation with a time-domain method. Note since the PML primarily attenuates waves propagating normal to the PML, the truncated PML will provide less attenuation for obliquely incident waves; consequently, a significant non-physical reflection can occur for a wave incident at a near grazing angle. For this reason, the PML has to be placed some distance away from all the sources of the field.

As an example to illustrate the idea of PML, the modified source-free Maxwell′s curl equation for electric field is shown below :

$$\nabla_s \times E = -j\omega\mu H \tag{2.6}$$

where ∇_s is defined by

$$\nabla_s = \hat{x}\frac{1}{s_x}\frac{\partial}{\partial x} + \hat{y}\frac{1}{s_y}\frac{\partial}{\partial y} + \hat{z}\frac{1}{s_z}\frac{\partial}{\partial z} \tag{2.7}$$

and ∇_s can be considered as the standard ∇ operator in Cartesian coordinates whose x, y, and z axes are stretched by a complex numbers of s_x, s_y, and s_z, respectively. Throughout the simulation domain the complex diagonal tensor′s s is the identity tensor, but inside the PML it has the following form [7]:

$$\overleftrightarrow{s} = \begin{bmatrix} \frac{s_y s_z}{s_x} & 0 & 0 \\ 0 & \frac{s_z s_x}{s_y} & 0 \\ 0 & 0 & \frac{s_x s_y}{s_z} \end{bmatrix} \tag{2.8}$$

Note that when a material property changes abruptly and the spatial discretization is not sufficiently dense, undesirable numerical reflections may occur. One approach to avoiding this problem is to vary the material parameters smoothly within the PML [8], thus we have:

$$s_{x,y,z} = 1 - j\Big(\frac{\alpha - L}{L}\Big)\delta_{x,y,z} \tag{2.9}$$

where $\delta_{x,y,z}$ is the loss tangent in dimension x, y and z , α is the distance from the edge, and L is the thickness of the PML, which is terminated at the simulation domain edge with a perfect electrical conductor (PEC) boundary condition. Figure 2.5 has illustrate the effect of the PML for a point source in free space. The calculated spatial profile is shown at time $t = 5t_0$, $t = 7t_0$, and $t = 10t_0$ respectively. As we can see, for the simulation domain with PML, the spherical wave generated by the point source are perfectly absorbed at the simulation domain boundary, while for the case without PML, the reflection from the boundary significantly interfaces with the spherical wave generated from the point source.

2.3 Finite-Difference Frequency-Domain

As we discussed earlier, time-domain methods such as FDTD are extremely useful when a transient or broadband analysis is required. However, when a steady-state solution is the only answer needed at a single frequency, the time-domain method is rather inefficient. Instead, the frequency-domain method, such as the Finite Difference Frequency Domain (FDFD) is highly applicable, since it maintains the finite-difference spatial features, but removes time stepping [9]. The steady-state solution is found at a single frequency through a matrix inversion process. This is often the most desirable solution to many problems, as many engineering problems involves quasi-steady state fields; and, if a single-frequency solution is sought, the FDFD is much faster than the transient broadband analysis afforded by FDTD.

In addition, the FDFD method has the advantage of taking care of the dispersive materials. In FDTD, implementing dispersive materials requires either convolution terms or auxiliary equations, but in FDFD, only one simple set of values of material

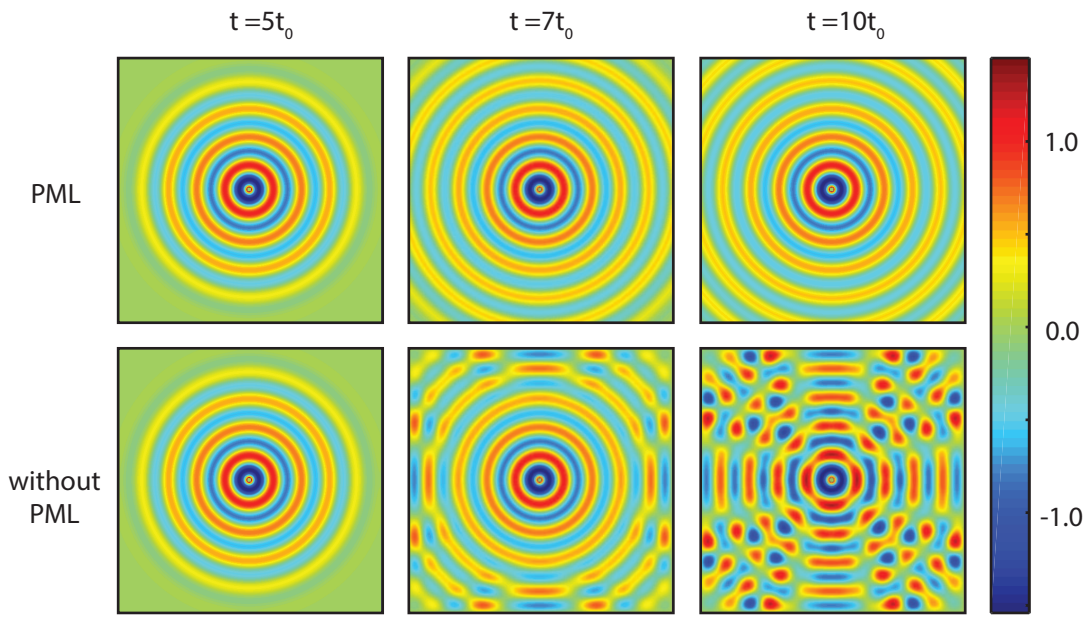

Figure 2.5: Visual illustration of dipole source in free space at time $t = 5t_0$, $t = 7t_0$, and $t = 10t_0$, with and without PML respectively.

properties are needed at the frequency of interest. Note that the FDFD can also be used for broadband simulations, by running multiple simulations with one at each frequency of interest. The spectral response of a problem can be determined with the frequency resolution limited only by the number of simulations. This can be useful for problems involving dispersive media, whose material parameters vary with frequency in a way that cannot be easily modeled in FDTD.

In this section, taking the advantages of the simplicity of 1D example, we briefly illustrates the frequency domain representation of the wave equation and the possible implementations through the Maxwell′s equations.

2.3.1 FDFD from Wave Equations

In practice, the FDFD normally utilizes the frequency domain wave equation for its setup [10]. The wave equation has a more compact form and does not require interleaving or Yee lattice. Meanwhile, only solving one wave equation is necessary; after solving for E, for example, H can be calculated directly follows from the frequency domain Maxwell′s equations.

In the source-free space, the wave equations can be simplified to:

$$\nabla^2 E + k^2 E = 0 \quad \text{and} \quad \nabla^2 H + k^2 H = 0 \tag{2.10}$$

where $k = \omega\sqrt{\epsilon\mu}$ is the wavevector. To illustrate how these equations are solved in FDFD, we will consider the 1D version of the electric field wave equation with a current source term J_z for generality:

$$\frac{\partial^2 E_z}{\partial x^2} + k^2 E_z = j\omega\mu J_z \tag{2.11}$$

We proceed to discretize the above equation using a second-order centered difference:

$$\frac{(E_z)_{m+1} - 2(E_z)_m + (E_z)_{m-1}}{(\Delta x)^2} + k^2 (E_z)_m = j\omega\mu (J_z)_m \tag{2.12}$$

Note that, followed by the notation defined in Eq. 2.3, we only need to discretize in space as there is no time dependence. Thus there is no superscript n, compared with the notation used in FDTD. The wavevector k is a purely complex constant. This difference equation can be rearranged as:

$$(E_z)_{m-1} + a(E_z)_m + (E_z)_{m+1} = b(J_z)_m \tag{2.13}$$

where $a = [k^2(\Delta x)^2 - 2]$ and $b = j\omega\mu(\Delta x)^2$. The entire system can then be represented in a tridiagonal matrix:

$$\underbrace{\begin{pmatrix} a & 1 & 0 & 0 & \cdots \\ 1 & a & 1 & 0 & \cdots \\ 0 & 1 & a & 1 & \cdots \\ \vdots & & & & \cdots \\ \cdots & 0 & 1 & a & 1 \\ \cdots & 0 & 0 & 1 & a \end{pmatrix}}_{M} \underbrace{\begin{pmatrix} (E_z)_0 \\ (E_z)_1 \\ (E_z)_2 \\ \vdots \\ (E_z)_{l-1} \\ (E_z)_l \end{pmatrix}}_{[E_z]} = b \underbrace{\begin{pmatrix} (J_z)_0 \\ (J_z)_1 \\ (J_z)_2 \\ \vdots \\ (J_z)_{l-1} \\ (J_z)_l \end{pmatrix}}_{[J_z]} \tag{2.14}$$

where the total number of spatial cells in our 1D system is $l + 1$. The solution of this equation can be found by simple matrix inversion as

$$[E_z] = [M]^{-1} b [J_z] \tag{2.15}$$

Note that this 1D example of a homogeneous medium can be easily replaced with inhomogeneous and frequency dependent materials, by replacing a, b with a_m and b_m, where it takes consider the material constant such as ϵ, μ and σ for each grid. From this above example, we see that the solution from FDFD involves taking an inverse of the matrix M, which can be easily done in 1D simulation. The discretized FDFD equations in 2D and 3D follows straightforwardly from the 1D example. However, in higher dimensional setup, this matrix M can become very large, thus advanced

linear algebra techniques are required for efficient calculation. In general, the Laplace matrices and the Kronecker products are introduced to assist the FDFD setup in 2D and 3D model. Detailed discussion can be found in [11].

Finally, in the 2D and 3D formulation, directly solving the wave equation of E field may suffer from a problem with the current source. This is due to the assumptions that the divergence of E and H are both equal to zero. Clearly this is not true at the position of the source. For this reason, it is common to solve the wave equation of H field, which can easily include curl J component due to the source, while $\nabla \cdot H = 0$ is still hold to be true.

2.3.2 FDFD from Maxwell′s Equations

FDFD method can also be formulated using Maxwell′s equations . Here, the frequency-domain Maxwell′s equations are as follows:

$$\begin{aligned} \nabla \times E &= -j\omega\mu H - M \\ \nabla \times H &= j\omega\epsilon E + J \end{aligned} \tag{2.16}$$

In the 1D case, we consider an x-directed propagation with E field polarized along y direction, we have:

$$\begin{aligned} \frac{\partial E_y}{\partial x} &= -j\omega\mu H_z - M \\ \frac{\partial H_z}{\partial x} &= j\omega\epsilon E_y + J \end{aligned} \tag{2.17}$$

Discretizing using the leapfrog method, we have the finite difference equations:

$$\begin{aligned} \frac{(E_y)_{m+1} - (E_y)_m}{\Delta x} &= -j\omega\mu (H_z)_{m+\frac{1}{2}} - M \\ \frac{(H_z)_{m+\frac{1}{2}} - (H_z)_{m-\frac{1}{2}}}{\Delta x} &= j\omega\epsilon (E_y)_m + J \end{aligned} \tag{2.18}$$

The matrix system can then be formulated into $[M][F] = [S]$, where the column vector $[F]$ includes each of the E components followed by each of the H components and $[S]$ is the source of the system. This linear system can be rearranged as follows:

$$\begin{aligned} a_h (H_z)_{m+\frac{1}{2}} + (E_y)_{m+1} - (E_y)_m &= -\Delta x M \\ a_e (E_y)_m + (H_z)_{m+\frac{1}{2}} - (H_z)_{m-\frac{1}{2}} &= \Delta x J \end{aligned} \tag{2.19}$$

Note that in this setup based from Maxwell′s equations, the matrix M, which must be inverted, is no longer tridiagonal; this means the inversion process will be more computational intensive. In addition, the vector of field values $[F]$ has doubled in length compared with the wave equation setup (Eq. 2.14), since we are simultaneously solving for E and H. Thus, the doubling of the field vector results in a quadrupling of the matrix M, which increase the computational cost considerably. Therefore, the FDFD method from the wave equation, in general, is more attractive than the FDFD method from Maxwell′s equations.

2.4 Beam Propagation Method

Among the many numerical methods available for modeling optical propagation in integrated and fiber optic photonic devices, the Beam Propagation Method (BPM) is the most commonly used technique for larger photonic system. BPM is an approximation technique for simulating the propagation of light in slowly varying optical waveguides [12]. It solves the well-known parabolic or paraxial approximation of the *Helmholtz* equation. There are several reasons for using the BPM over other numerical methods. First, it is a conceptually straightforward technique and is easily implemented even in three dimensions. Second, it is a very efficient method with an optimal computational complexity, i.e., the computational effort is proportional to the number of grid points used in the simulation. Overall, the BPM is very flexible method and require less intensive computing power compared with other methods such as FDTD.

2.4.1 Paraxial formulation

In this section, we demonstrate the simplest version of BPM, where one assumes a scalar electric field E and paraxial approximations which restrict its applicability

to the fields propagating at small angles with respect to the axis of the waveguide [13]. We define this axis as z axis. To illustrate the method, we start from the monochromatic wave equation. Assuming a scalar field, ϕ, and paraxiality, the wave equation is written in the form of the Helmholtz equation,

$$\frac{\partial^2\phi}{\partial x^2} + \frac{\partial^2\phi}{\partial y^2} + \frac{\partial^2\phi}{\partial z^2} + k^2(x,y,z)\phi = 0 \tag{2.20}$$

where the spatially varying wavenumber is $k(x,y,z) = k_o n(x,y,z)$, and the free space wavenumber is $k_o = 2\pi/\lambda$. The refractive index $n(x,y,z)$ solely defines the geometry of the problem. Considering that the most rapid variation in the field ϕ is the phase variation due to propagation predominantly along the z direction, it is beneficial to factor out this rapid variation by introducing a slowly varying field u,

$$\phi(x,y,z) = u(x,y,z)e^{i\beta z} \tag{2.21}$$

where β is a free parameter called the reference wavenumber and is frequently expressed in terms of a reference refractive index, n_0, via $\beta = k_0 n_0$. Here, n_0 can be the refractive index of the substrate or cladding. Substituting Eq. 2.21 into Eq. 2.20 gives the equation for the envelope of the field:

$$\frac{\partial^2 u}{\partial z^2} + 2i\beta\frac{\partial u}{\partial z} + \frac{\partial^2 u}{\partial y^2} + \frac{\partial^2 u}{\partial x^2} + (k^2 - \beta^2)u = 0. \tag{2.22}$$

By assuming that the variation of u with z is sufficiently slow such that

$$\left|\frac{\partial^2 u}{\partial z^2}\right| \ll \left|2\beta\frac{\partial u}{\partial z}\right| \tag{2.23}$$

the above equation reduces to

$$\frac{\partial u}{\partial z} = \frac{i}{2\beta}\Big[\frac{\partial^2 u}{\partial x^2} + \frac{\partial^2 u}{\partial y^2} + (k^2 - \beta^2)u\Big] \tag{2.24}$$

which is known as the Fresnel or paraxial equation. This approximation eliminates the second-order derivative term in z, which reduces the second-order boundary value problem to a first-order initial value problem, so that it can be solved by simple

integration along the propagation direction z. In addition, the efficiency is enhanced by the fact that the longitudinal grid can be much coarser than the wavelength for many problems.

2.4.2 Finite-Difference BPM

Here we present the detailed implementation of BPM based on finite-difference method [14, 15]. The above differential equation can be numerically integrated in the forward z direction using the Crank-Nicholson scheme, which is a finite-difference approach and is the most widely used. In this numerical scheme, the field in the transverse x-y plane is denoted as discrete points on a grid, and at discrete points along the longitudinal propagation direction z. Given the field at one z plane, the field at the next z plane can be determined. The stepping process is repeated to account for the propagation throughout the structure. Assuming a 2D BPM case, if we let u_i^m denote the field at the transverse grid point i and longitudinal plane m and assume the the grid points and planes are equally spaced by Δx and Δz apart. Thus in the Crank-Nicholson scheme, Eq. 2.24 is represented at the midplane between the known plane m and the unknown plane $m+1$ as follows:

$$\frac{u_i^{m+1} - u_i^m}{\Delta z} = \frac{i}{2\beta}\Big[\frac{\delta^2}{\Delta x^2} + (n^2 k_0^2 - \beta^2)\Big]\frac{u_i^{m+1} + u_i^m}{2} \tag{2.25}$$

where δ^2 is the second-order difference operator, $\delta^2 u_i = [u_{(i+1)} + u_{(i-1)} - 2u_i]$, and n is the averaged refractive index between the two planes. The above equation can be rearranged into the form of a standard tridiagonal matrix equation for the unknown field u in the plane $(n+1)$ in terms of known quantities, resulting in

$$a u_{i-1}^{n+1} + b u_i^{n+1} + c u_{i+1}^{n+1} = d \tag{2.26}$$

where the expressions for the coefficients a, b, c, and d above are readily derived and can be found in [16].

Boundary conditions. Since the field can only be represented on a finite computational domain, the above equation requires an appropriated boundary condition

which complete the system of equations. A commonly used boundary condition is the so-called transparent boundary condition (TBC). The basic approach is to assume that near the boundary the field behaves as an outgoing plane wave, with characteristics that are dynamically determined via some heuristic algorithm. The TBC is generally very effective in allowing radiation to freely escape the computational domain and details on implementations are given in [17].

2.4.3 BPM Expansions

Certainly there are a few limitations on the traditional BPM that is based on the paraxial approximations. For example, the fields must propagate primarily along the z axis, i.e., fields are paraxial and limited to a small angular spread in wavenumber. This places a restriction on geometries with large and abrupt perturbations along the z axis. Also, the gradient of the refractive index must be small. In addition, the elimination of the second-order derivative term eliminates the possibility of a backward propagating wave solution; thus devices relying on reflections cannot be modeled. In this section, we briefly introduce a few techniques that is to eliminate or significantly relax these limitations.

Wide-angle BPM. The fundamental physical limitation of the above BPM approach results from the parabolic approximation to the Helmholtz equation, which implies a paraxiality condition on the primary direction of propagation. This restriction as well as the related restrictions on index-contrast can be relaxed through the use of extensions that have been referred to as wide-angle BPM. The essential idea behind this approach is to reduce the paraxial limitations by incorporating the effect of the second-order derivative term that was neglected in the basic BPM. Thus the above mentioned limitations can be reduced using more accurate approximations to the Helmholtz equation. The most popular formulation is based on Padé approximants [18]. In general, larger angles, higher index contrast, and more complex mode

interference can be analyzed in both guided wave and free space problems as the Padé order increases. Detailed discussion for using this technique can be found in [19].

Bi-directional BPM. While wide-angle BPM allows propagation in a wider numerical aperture, it is still not able to include the backward traveling wave. Therefore, various bi-directional BPM techniques have been considered to address this issue, with most focusing on the coupling that occurs through reflection of a wave incident on an interface along z direction [20, 21]. For example, the guided wave propagation can be divided into regions that are uniformed along z and the interfaces between these regions. At any point along the structure, it is considered that both forward and backward waves can exist. The essential idea is to employ a transfer matrix M' which describes the entire structure that is composed of propagation and interface matrices. The propagation matrices describe the uniform regions using normal BPM. The interface matrices are given by generalized Fresnel formulas involving differential operators employing the Padé approximants used in wide-angle BPM.

Full-vector BPM. The basic BPM approach discussed above results from the assumption of scalar waves, which prevents the polarization effects from being considered. This limitation can be overcome though a Full-vector BPM technique, which is to recognize the electric field as a vector and solving from the vector wave equation rather than the scalar Helmholtz equation. This approach can be found with more details in [22, 23].

2.5 Finite Element Methods

Finite element method (FEM) was originally developed for mechanical and structural analysis in the 1950s. It became popular in solving the vector electromagnetic problems after an important breakthrough occurred in the 1980s with the development of edge-based vector element [24, 25]. There is a major difference between the

finite-difference methods (FDM) and the FEM. From the discussions earlier in this chapter, we note that, in principles, FDM finds an *approximation to the differential operators*, and then use these difference equations to solve for the fields at each grid; while the FEM makes an *approximation to the solution* of the differential equation over the domain of the problem, and then tailors that approximation to minimize its difference with the exact solution.

The FEM is a numerical procedure to convert partial differential equations into a set of linear algebraic equations to obtain approximate solutions to boundary-value problems. In particular, it divides the simulation space into small areas or volumes, which can be arbitrarily shaped and oriented; for this reason, the FEM is well suited to problems with complex geometry. The solution to Maxwell′s equations over each subdomain is then approximated with some functional form, usually a low-order polynomial. The solutions in each subdomain are then made to be continuous across their boundaries, and the solution must be made to fit with the global boundary conditions. The primary reasons for using FEM rather than FDM for electromagnetic problems are its geometric flexibility and the ability to work in higher orders of accuracy. Geometric flexibility arises because the grid in FEM can use arbitrary polygons or polyhedral (in 2D or 3D, respectively), and these can be designed to match the shapes of objects in the simulation space.

In this section, we illustrate the basic principle of the FEM by briefly introducing the methods for solving the boundary-value problems in mathematical modeling. Then we present the formulation procedure of the FEM to solve the electromagnetic problems in frequency domain.

2.5.1 Boundary-Value Problems

Boundary-value problems has long been a major topic in mathematical modeling. A typical boundary-value problem can be defined by a governing differential equation

in a domain Ω, with boundary conditions specified on the boundary that encloses the domain: $\mathcal{L}\psi = f$, where $\mathcal{L}$ is a differential operator, f is the source function, and ψ is the unknown quantity. In electromagnetics, the form of the governing differential equation ranges from a simple Poisson equation to complicated vector wave equations.

To solving the boundary-value problems, various approximate methods have been developed, and among them the Ritz and Galerkin′s methods have been used most widely [26]. The **Ritz method** is a direct method to find an approximate solution for boundary value problems. It is a variational method which starts from the variational representation, which is referred to as functional, of the boundary-value problem. The minimum of the functional corresponds to the governing differential equation under the given boundary conditions. The approximate solution is then obtained by minimizing the functional with respect to its variables. On the other hand, **Galerkin′s method** belongs to the family of weighted residual methods, which start directly from the partial differential equation of the boundary-value problem and seek the solution by weighting the residual of the differential equation. In this method, it converts a continuous operator problem into a discrete problem, then characterize the discrete space with a finite set of basis functions, i.e., the weighting function, used for the expansion of the approximate solution. A brief reviews of the Ritz and Galerkin′s methods and a detailed illustration of their solution procedures to a simple boundary-value problem can be found in [27].

2.5.2 Implementation of FEM

In general, it is a very challenging step in the Ritz and Galerkin's methods to find a trial function defined over the entire solution domain, which is capable of representing the true solution of the problem. This is particularly true for two- and three-dimensional problems. To make it simpler, we can divide the entire domain into small subdomains and employ the trial functions defined over each subdomain.

These trial functions are usually in a much simpler form since the subdomains are small. Therefore, the principle of the finite element method is to replace an entire continuous domain by a number of subdomains, in which the unknown function is represented by simple interpolation functions with unknown coefficients. A system of equations is then obtained by applying the Ritz variational or Galerkin′s procedure and the solution of the boundary-value problem is achieved by solving the system of equations. The basic steps for a finite element method can be summarized as follows:

- *Domain discretization.* The first and perhaps the most important step in the finite element method is to discretize the domain over which the solution is desired. An effective discretization with proper numbering for each elements can significantly affect the computing time, memory usage, as well as the accuracy of the numerical results [5]. Note that the linear line segments, triangles, and tetrahedral are the most frequently used subdomain elements for one- two- and three-dimensional modelling, due to their simplicity and suitability for domains with arbitrary shape and volume. We demonstrate two examples in Fig. 2.6 showing the finite element discretization of a two- and a three-dimensional domain.

- *Select interpolation functions.* The approximation of the unknown solution is assumed to take a specific functional form over each small element. In general, the interpolation is usually selected to be the linear (first-order polynomial) or parabolic (second-order) functions. These functions are then matched to the adjacent cells to ensure continuity across the cell boundaries

- *Formulate a system of equations.* In this step, each elemental equation can be formulated using either the Ritz variational or Galerkin′s method. The system of equations can then be set up by summing the elemental equations over the entire domain. The boundary conditions are then imposed to obtain

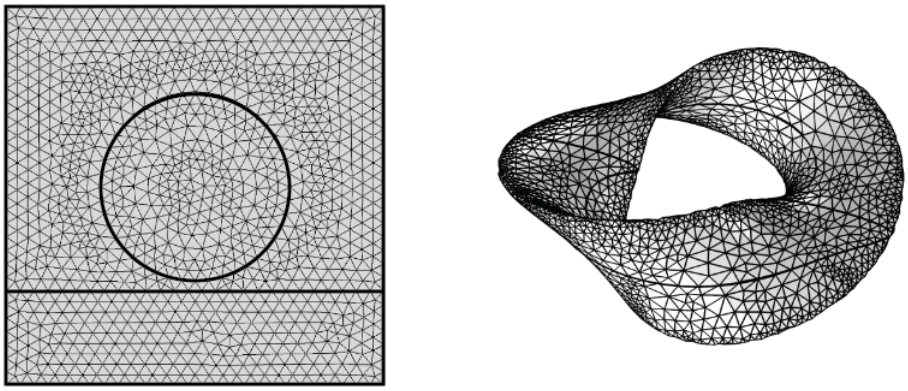

Figure 2.6: Visual illustration of the finite element mesh grid for 2D (left) and 3D (right) object.

the final form of the system of equations. This system includes information about boundaries and sources, also have the added constraint of continuity across element boundaries.

- *Solve the system of equations.* The resultant system, in general, has one of the following two forms:

$$[M][\phi] = [S] \tag{2.27}$$

or

$$[A][\phi] = \lambda[B][\phi] \tag{2.28}$$

In electromagnetics, Eq. 2.27 is corresponding to the wave equations with the known vector $[S]$ as the source. Equation 2.28 represents the eigenvalue systems that associated with source-free problems. In this case, the source vector $[S]$ vanishes and the matrix $[K]$ can be written as $[A] - \lambda[B]$, where λ denotes the unknown eigenvalues. Similar to FDFD, solving these systems becomes purely a linear algebra problem, and the truncation of the infinitely large solution domain into a finite computation domain is accomplished by setting up an artificial mesh layer with either absorption boundary conditions (ABC) or perfect matching layers (PML).

2.6 Summary

In this chapter, we briefly descrbed the basic principle and formulation of a few major computational methods for numerical analysis of electromagnetic fields for photonics applications. These include the finite-difference time-domain method, finite-difference frequency-domain method, beam propagation method and the finite element method. We started with the construction of the finite differencing formulas and demonstrated their applications in solving one-dimensional Maxwell′s equations. Taking the advantage of the simplicity of one-dimensinal problems, we discussed the

working principles, stability criterion and boundary conditions in the time-domain simulation. The finite-difference method then extended to frequency domain, where the linear system of equations can be formulated. After that, we illustrated the basic principle and steps of finite element method with possible applications to electromagnetic problems. These four methods are chosen because they represent the fundamental and the popular approaches for numerical analysis of photonics engineering design. The reader is also encouraged to consult more advanced books and references listed in the end of this chapter, for a more comprehensive understanding about these methods with a variety of advanced treatment and applications.

2.7 References

[1] K. Yee, "Numerical solution of initial boundary value problems involving maxwell's equations in isotropic media," *IEEE Trans. Antennas Propag.*, vol. 14, no. 3, pp. 302–307, 1966.

[2] M. S. Wartak, *Computational photonics: an introduction with MATLAB*. Cambridge University Press, 2013.

[3] W. H. Press, *FORTRAN Numerical Recipes: Numerical recipes in FORTRAN 90*. Cambridge University Press, 1996.

[4] A. Taflove and S. C. Hagness, *Computational electrodynamics*. Artech House, 2005.

[5] J.-M. Jin, *Theory and computation of electromagnetic fields*. John Wiley & Sons, 2011.

[6] J.-P. Berenger, "A perfectly matched layer for the absorption of electromagnetic waves," *J. Comput. Phys.*, vol. 114, no. 2, pp. 185–200, 1994.

[7] S. D. Gedney, "An anisotropic perfectly matched layer-absorbing medium for the truncation of fdtd lattices," *IEEE Trans. Antennas Propag.*, vol. 44, no. 12, pp. 1630–1639, 1996.

[8] W. Chew and J. Jin, "Perfectly matched layers in the discretized space: An analysis and optimization," *Electromagnetics*, vol. 16, no. 4, pp. 325–340, 1996.

[9] K. S. Kunz and R. J. Luebbers, *The finite difference time domain method for electromagnetics*. CRC Press, 1993.

[10] J. D. Joannopoulos, S. G. Johnson, J. N. Winn, and R. D. Meade, *Photonic crystals: molding the flow of light*. Princeton University Press, 2011.

[11] U. S. Inan and R. A. Marshall, *Numerical electromagnetics: the FDTD method*. Cambridge University Press, 2011.

[12] S. Obayya, *Computational photonics*. John Wiley & Sons, 2011.

[13] B. E. Saleh, M. C. Teich, and B. E. Saleh, *Fundamentals of photonics*, vol. 22. Wiley New York, 1991.

[14] R. Scarmozzino, A. Gopinath, R. Pregla, and S. Helfert, "Numerical techniques for modeling guided-wave photonic devices," *IEEE J. Quantum Electron.*, vol. 6, no. 1, pp. 150–162, 2000.

[15] R. Scarmozzino and R. Osgood, "Comparison of finite-difference and fourier-transform solutions of the parabolic wave equation with emphasis on integrated-optics applications," *J. Opt. Soc. Am. A*, vol. 8, no. 5, pp. 724–731, 1991.

[16] Y. Chung and N. Dagli, "An assessment of finite difference beam propagation method," *IEEE J. Quantum Electron.*, vol. 26, no. 8, pp. 1335–1339, 1990.

[17] G. R. Hadley, "Transparent boundary condition for the beam propagation method," *IEEE J. Quantum Electron.*, vol. 28, no. 1, pp. 363–370, 1992.

[18] G. R. Hadley, "Wide-angle beam propagation using padé approximant operators," *Opt. Lett.*, vol. 17, no. 20, pp. 1426–1428, 1992.

[19] G. R. Hadley, "Multistep method for wide-angle beam propagation," *Opt. Lett.*, vol. 17, no. 24, pp. 1743–1745, 1992.

[20] P. Kaczmarski and P. Lagasse, "Bidirectional beam propagation method," *Electron. Lett.*, vol. 24, no. 11, pp. 675–676, 1988.

[21] H. Rao, R. Scarmozzino, and R. M. Osgood, "A bidirectional beam propagation method for multiple dielectric interfaces," *IEEE Photon. Technol. Lett.*, vol. 11, no. 7, pp. 830–832, 1999.

[22] W. Huang and C. Xu, "Simulation of three-dimensional optical waveguides by a full-vector beam propagation method," *IEEE J. Quantum Electron.*, vol. 29, no. 10, pp. 2639–2649, 1993.

[23] C. Xu, W. Huang, J. Chrostowski, and S. Chaudhuri, "A full-vectorial beam propagation method for anisotropic waveguides," *J. Lightwave Technol.*, vol. 12, no. 11, pp. 1926–1931, 1994.

[24] J.-C. Nédélec, "Mixed finite elements in r3," *Numer. Math.*, vol. 35, no. 3, pp. 315–341, 1980.

[25] M. Barton and Z. Cendes, "New vector finite elements for three-dimensional magnetic field computation," *J. Appl. Phys.*, vol. 61, no. 8, pp. 3919–3921, 1987.

[26] O. Axelsson and V. A. Barker, *Finite element solution of boundary value problems: theory and computation*. SIAM, 2001.

[27] J.-M. Jin, *The finite element method in electromagnetics*. John Wiley & Sons, 2015.

Chapter 3

Engineering Metal-Nanoantennae/Dye Complexes for Maximum Fluorescence Enhancement

Abstract

We theoretically investigate the fluorescence enhancement of a representative set of dye-molecules excited by three nanoantennae geometries, using a fully vectorial three-dimensional finite-difference time-domain (3D FDTD) method. Through these 3D FDTD calculations, in conjunction with analytic guidance using temporal coupled-mode (TCM) theory, we develop a design procedure for antenna assemblies that allow achieving fluorescence enhancements of 200-900× over the emission intensity of the dye molecule in free space. The enhancement from these commercially available fluorochrome conjugates, namely, $CF^{TM}568$, $CF^{TM}660R$ and $CF^{TM}790$ are fully investigated using spherical-dimer, elliptical-dimer, and bowtie nanoantennae, where there is an optimal antenna structure for high fluorescence enhancement for each specific dye-molecule pair due to the different plasmonic response and field coupling with variation in shape at each wavelength. These results demonstrate a method for rationally designing arbitrary metallic nanoparticle/emitter assemblies prior to their synthesis and assembly to achieve optimum fluorescence enhancement.

3.1 Introduction

It is well known that the absorption cross section and radiative efficiency of a molecule can be enhanced by a nearby plasmonic nanostructure; this enhancement is important, for example, for applications in biosensing and photovoltaics [1, 2]. Furthermore, while the enhancement of the local optical field due to the metal structure can be calculated accurately numerically, much less numerical research has been carried out on the *combined effects* of excitation and quenching. Fluorescence enhancement depends on the metallic composition, size, shape, orientation of the nanoantennae, the dielectric properties of the surrounding medium, the number of nanoantennae, and the polarization state and frequency of the incident beam. Each of these parameters modifies the combined effects of excitation by the incident field and ohmic loss in the nanoantennae [3, 4]. Recently, Dal Negro and coworkers have theoretically investigated the fluorescence enhancements and deep-ultraviolet near-field interactions for single metal nanoparticles of various shapes and sizes, using a surface integral equation method [5]. However, there has been no systematic investigation of the emission properties of dye molecules coupled to nanoantennae of different shapes, sizes and their interactions in the visible spectrum region.

Analysis of the fluorescence properties of an emitter such as a dye molecule can be carried out by generalized Mie theory (GMT) [6]. However, Mie theory cannot directly predict the scattering of non-spherical particles or of an arbitrary ensemble of nanoparticles. Thus for the case of light scattering by non-spherical nanoparticles, only approximate GMT algorithms have been established. In addition, an important earlier analytic study, which considered a single spherical antenna [7–9], used a Green's function approach to analyze the molecule's linear excitation rate. This method provided a useful analytic formulation; however, such an approach lacks the generality of rigorous numerical computation.

Concomitantly, synthesis methods have been developed by many groups, which

enable fabrication of specific nanoparticle structures for fluorescence with sub-nanometer precisions using DNA self-assembly. For example, Gang and coworkers have developed methods of fabricating arrays by DNA self-assembly [10–12]. These arrays consist of structures formed with metal nanoparticles and dye molecules. In addition, Zhang and coworkers also have implemented several viable synthetic methodologies for the fabrication of a range of nanoscale formulations [13, 14]. These synthesis methods require a companion approach for computing the optical/fluorescence properties of the structures.

In this chapter, we use a method based on full vectorial three-dimensional finite-difference time-domain (3D FDTD) computation to calculate accurate fluorescence enhancements for arbitrary-shaped metal nanoparticle antennae. In addition, we show that temporal coupled-mode (TCM) theory [15] can be used for analytical guidance in the optimization of the antennae design. We have determined antennae configurations that optimize the fluorescence enhancement of each of a selected set of dye molecules, which are matched to three different antennae geometries. Our results provide guidance for the rational design of optimized metallic nanoparticle complexes for maximum fluorescence enhancement. Finally, we note that this approach provides a design method for applications of optically active nanostructures in near-field imaging [16, 17], biosensing [18, 19], light harvesting [20, 21] and nonlinear optical properties of metal nanostructures [22, 23].

3.2 Dye-molecule/antenna complex

First, for our emitter-dye complexes, the emission spectrum of each dye is dependent on both the spectral response of each dye and the response and efficiency of its nearby nanoantenna. Second, each dye/antenna combination exhibits strong fluorescence enhancement only over a limited spectral region, where in this chapter,

only antennae having a fixed specific volume of metal are considered and compared. This behavior is sketched in Fig. 3.1(a) for the cases of a spherical- and an ellipsoidal-dimer antenna. The spectral response can be broadened or shifted by changes in the geometry of the antenna. For example, a change in the spacing between the antenna nanoparticles shifts the antenna response—but only by a relatively small amount; see the dotted line in Fig. 3.1(a). On the other hand, it is possible to access other spectral regions using an antenna with a different geometrical shape such as the ellipsoid shown in Fig. 3.1(a), since the antenna has a distinct, shape-dependent localized-plasmon resonance frequency. Finally, note that enlarging the radius of a spherical dimer also shifts the antenna response, while at the same time increasing the magnitude of field enhancement due to its larger antenna polarizability (Fig. 3.1(b)). However, larger antennae also experience larger ohmic loss. This large ohmic loss makes the larger spherical dimer/dye cluster to be a less efficient emitter than the smaller ellipsoid dimer/dye cluster. Therefore, the scope of this chapter focuses on investigating the influence of the nanoparticle geometry, rather than the dependence on volumetric scaling.

Our goal is to provide a general approach to designing nanoantennae for efficient molecule light-emitting clusters. Thus, we consider the radiative and quenching processes of an excited emitting dye molecule in the near field of a metal nanoantenna, illuminated by a monochromatic optical source, as shown in Fig. 3.2(a). The approximate energy level of dye molecule is shown in Fig. 3.2(b). In the presence of incident light with intensity I_0, the molecule undergoes optical excitation followed by either nonradiative quenching or fluorescence, with an appropriate Stokes shift. If a dye molecule is located within the near field of the metal antenna, resonant localized plasmons within the metal can enhance these optical processes. In effect, the metal antenna causes a much stronger local field to form at the position of the dye

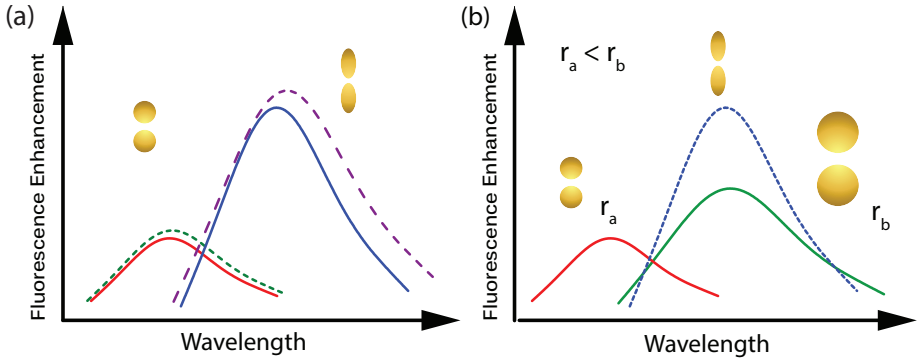

Figure 3.1: (a) A conceptual sketch showing how the choice of nanodimer type (a spherical and ellipsoidal dimer with a fixed volume are shown here) selectively enhances a certain fluorescence-emission wavelength region. Only a very limited tuning of the dimer's spectral response is achieved by changes in the interdimer-nanoparticle spacing. For example, when the dimer spacing is adjusted by 1nm, the resonance will shift from solid curve to dash line. (b) Spectral shifting and variation in fluorescence enhancement can also be achieved with a change in dimer radius (solid lines). The larger enhancement due to shape effect is shown for comparison (dotted lines).

molecule due to excitation of localized surface plasmons (LSP), which corresponds to the external field distribution, causing, in turn, stronger optical excitation of the dye molecules. This excited molecule gives enhanced fluorescence as it decays radiatively with rate $\gamma_{rad} = 1/\tau_{rad}$, as shown in Fig. 3.2(c). Note that ohmic loss within the metal antenna inserts an additional non-radiative channel with the non-radiative decay rate of $\gamma_{nrad} = 1/\tau_{nrad}$ that is not present in an isolated dye molecule.

Considering these processes, we can express the fluorescence rate γ_{em} of a single molecule as the product of an excitation rate γ_{exc} and the quantum yield q, where q is defined as the ratio of radiative transition rate (from excited to ground state) to the total decay rate: thus nonradiative quenching lowers q. It is sufficient to treat the excitation and emission processes independently because there is no coherence between the two processes [7]. The fluorescence enhancement can then be expressed as

$$\frac{\gamma_{em}}{\gamma_{em}^0} = \frac{\gamma_{exc}}{\gamma_{exc}^0} \cdot \frac{q}{q^0} \tag{3.1}$$

where the superscript '0' indicates the corresponding free-space quantity. Since we are considering only linear excitation processes, the excitation rate of the molecule is directly proportional to the number of incident photons, i.e., the incident intensity of the field:

$$\frac{\gamma_{exc}}{\gamma_{exc}^0} = \frac{|\mathbf{E}(\mathbf{r})|^2}{|\mathbf{E_0}(\mathbf{r})|^2} \tag{3.2}$$

The values of $\mathbf{E}(\mathbf{r})$ and $\mathbf{E_0}(\mathbf{r})$, which are the electric-field strengths for a specific optical frequency ω at the location, $\mathbf{r}$, of the molecule with and without the presence of an antenna, are obtained from our 3D FDTD calculations. The fluorescence enhancement is calculated by approximating the emitting molecule as a classical dipole; this approach has been described earlier by Gersten and Nitzan [24] and Novotny [7, 8]. The wavelength of the dipole is set to the emission wavelength of the dye, i.e., the Stokes shift is empirically accounted for. To obtain the quantum yield, q, of the isolated molecule, ohmic loss must be obtained using the dielectric function of the

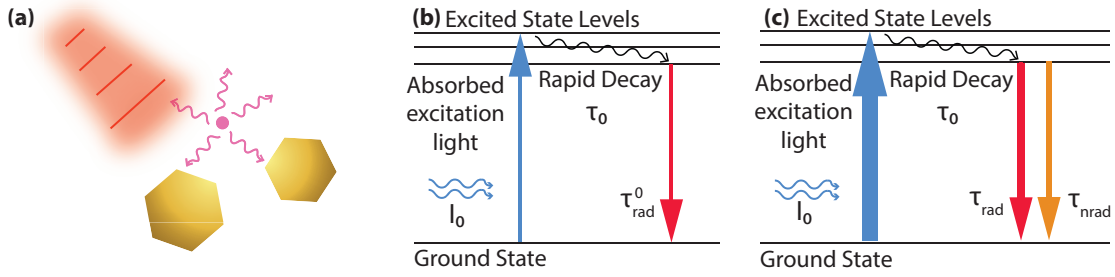

Figure 3.2: (a) A schematic illustration of an antenna-dye system under laser illumination. (b) Energy level for dye molecules in free space. (c) Energy level for dye molecules near metallic nanoantennae.

nanoantenna metal. This process includes a nonradiative rate γ_{nrad}, which then gives the quantum yield [25],

$$q = \frac{\gamma_{rad}/\gamma^0_{rad}}{\gamma_{rad}/\gamma^0_{rad} + \gamma_{nrad}/\gamma^0_{rad} + (1-q^0)/q^0} \tag{3.3}$$

where $\gamma_{rad}/\gamma^0_{rad}$ and $\gamma_{nrad}/\gamma^0_{rad}$ are the normalized radiative and non-radiative decay rates. Placing the emitter within the near-field of the nanoantenna increases its local optical density of states [26]. Then based on Fermi's Golden rule, the radiative decay rate will change compared to its value in free space. The analysis—discussed in Ref. [7, 9]—shows that the normalized energy-transfer rate can be written as $\gamma_{rad}/\gamma^0_{rad} = P_{rad}/P_0$ and $\gamma_{nrad}/\gamma^0_{rad} = P_{nrad}/P_0$, with P_{rad} being the power radiated by the classical dipole in the presence of a metal nanoparticle, P_{nrad} being the power absorbed by the metal particle due to ohmic loss, and P_0 being the power radiated by a classical dipole in free space. The quantum yield is then obtained by measuring the power emitted from the dipole-nanoantenna system.

3.3 Theoretical approach

To model the metal antennae optical response accurately, a parametrized Drude-Lorentz model [27, 28] was used. The analysis below considers Au antennae because of their prevalence in many fluorescence applications [7, 10]. We chose dyes that emit at red or near-infrared wavelengths because Au has a low absorption coefficient in this wavelength range. In this work, size effects on the metal dielectric constant were neglected and all dye-molecules were assumed to have unity internal quantum efficiency. In addition, because they are commonly used in cellular and biophotonics applications, we chose commercially available fluorochrome conjugates for these molecules, namely, $CF^{TM}568$, $CF^{TM}660R$ and $CF^{TM}790$ [29], which have useful spectral distributions, namely excitation maxima at 562nm, 663nm, 784nm, and peak emission wavelengths at 583nm, 682nm, and 806nm, respectively.

3.3.1 Analytical Method

In order to gain analytical insight into the optical properties of our nano-system, we first treat the metal nanoparticles as coupled resonators and employ the TCM theory discussed by Haus [15] to analyze the energy transfer between the incident light and metal nanospheres. While the use of TCM theory is approximate, it does enable a qualitative analysis of our systems. It, thus, allows us to determine the factors controlling antennae performance and provides guidance for understanding under which conditions the metal antennae increase radiative efficiency.

The framework of TCM theory can be best illustrated by considering the fields of a metal antenna cluster in the presence of an exciting beam with power of $|s_+|^2$. For illustrative purposes, we consider a metal antenna consisting of two spheres with a fixed spacing, i.e., a dimer, which is illuminated by a beam propagating perpendicular to,and polarized paralleled to,the dimer axis. TCM theory then generates the following rate equations to describe the relationship between the isolated sphere LSP-mode amplitudes, (a_1 and a_2, with corresponding energies $|a_1|^2$ and $|a_2|^2$ and LSP resonant frequencies ω_1 and ω_2),

$$\frac{da_1}{dt} = i\omega_1 a_1 - \frac{\gamma_{nrad} + \gamma_{rad}}{2} a_1 + \kappa_{in} s_+ + \frac{\gamma_{12}}{2} a_2 \tag{3.4}$$

$$\frac{da_2}{dt} = i\omega_2 a_2 - \frac{\gamma_{nrad} + \gamma_{rad}}{2} a_2 + \kappa_{in} s_+ + \frac{\gamma_{21}}{2} a_1 \tag{3.5}$$

where γ_{rad} is the radiative decay rate of a sphere with radius of r_0 at frequency ω which is known as

$$\gamma_{rad} = \gamma_{rad}^{4\pi} = \left(\frac{2\pi r_0}{\lambda}\right)^3 \frac{\omega}{1 + 2\epsilon_D} \tag{3.6}$$

and λ and ϵ_D are the wavelength of incident beam and the dielectric constant of the medium, respectively. The nonradiative decay rate $\gamma_{nrad} = \gamma$, with γ being the metal ohmic loss in the Lorentz-Drude approximation. The in-coupling coefficient, κ_{in}, is the degree of coupling between the incident light and the LSP, and γ_{12} and γ_{21} are the coupling coefficients between an LSP of one sphere with another.

Based on the dipole-dipole approximation [30, 31], the in-coupling coefficient κ_{in} can be evaluated as $\kappa_{in} = (\gamma_{rad}^{\Omega})^{1/2}$, with Ω being the far-field solid angle, where $\gamma_{rad}^{\Omega} = \gamma_{rad} \int_0^{\Omega} f(\theta, \phi) d\Omega$ and $f(\theta, \phi) = 3(1 - \sin^2\theta \cos^2\phi)/8\pi$. Due to the symmetry of our dimer system, the coupling coefficients $\gamma_{12} = \gamma_{21} = \gamma_c$ and the amplitudes of the LSP modes $a_1 = a_2 = a$. We can evaluate the γ_c using an overlap integral as follows,

$$\gamma_c = \frac{\frac{\omega}{2}\epsilon_o \int_{mode} [\epsilon(\mathbf{r}) - \epsilon_d] E_1^*(\mathbf{r}) \cdot E_2(\mathbf{r}) dV}{|a|^2} \tag{3.7}$$

where $E_1(\mathbf{r})$ is the electric field at location $\mathbf{r}$ when both LSP_1 and LSP_2 are present, $E_2(\mathbf{r})$ is the electric field at location $\mathbf{r}$ when only LSP_2 is present and the LSP mode energy $|a|^2 = \frac{1}{2}\epsilon_o \epsilon_D E_{max}^2 V_{eff}$, where V_{eff} is the effective mode volume [30]. Therefore, the steady-state solution of Eqs. 3.4 and 3.5 yields

$$a = \frac{2\kappa_{in}}{(\gamma_{rad} + \gamma_{nrad} - \gamma_c) - 2j(\omega - \omega_o)} s_+, \tag{3.8}$$

where ω_0 is the LSP resonance frequency. This equation shows the proportionality between s_+ and a, and hence between the incident power $|E_{inc}|^2$ and the isolated LSP $|E_{max}|^2$ of the sphere. The radiative γ_{rad} and non-radiative loss rates γ_{nrad} are mostly dependent on the particle size, while the coupling rate γ_c is mostly dependent on the inter-particle spacing. We can then vary the enhancement via a change in ω or in nanoparticle geometry.

As mentioned before, while useful for qualitative insight, TCM does not provide quantitative accuracy. This is readily illustrated by detailed comparison between the results of TCM theory and FDTD simulation (Fig. 3.3). For this comparison, we have selected a dimer structure with two 40nm-radius spherical Au particles under illumination by 663nm light. The surface-to-surface spacing is adjusted from 4nm to 20nm. The dashed line shows the enhancement estimated by TCM, which is in good agreement with the FDTD results (solid curve) at larger spacings (>10nm). At this larger spacing, results obtained with TCM for an isolated metal-sphere-nanoparticle overlap those obtained using Eq. 3.7, agree well with the exact numerical solution.

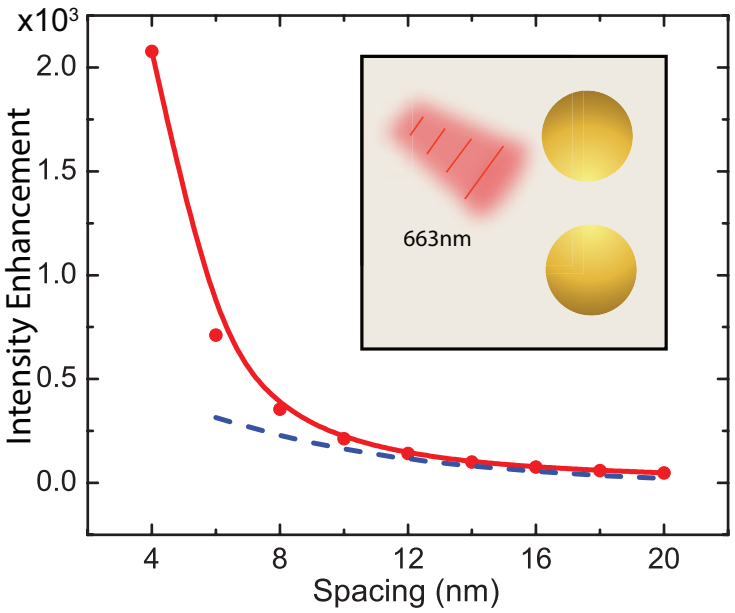

Figure 3.3: The intensity enhancement measured at the center of the gap using TCM is presented as the dashed curve (blue) for a dimer structure with two 40nm-radius spherical Au particles under the illumination of 663nm light; the solid curve (red) is the result from FDTD simulations; note that the curves continue to diverge at smaller inter-particle spacings of the dimer.

However, we can see that with decreasing inter-particle distance TCM fails to accurately predict the field enhancement by treating the dimer as a single-dipole.

3.3.2 Simulation

The advantages of FDTD simulation are its accuracy and simplicity of implementation. Our simulations are implemented on the computer clusters (gen04) at Brookhaven National Laboratory's Center for Functional Nanomaterials. The problem was solved across hundreds of cores, enabling not only division of a large numerical problem into smaller calculations, but also the concurrent investigation of multiple structures. For our simulation model, a nanoantenna/dye molecule was illuminated using a *cw* plane-wave source, with an excitation wavelength located at the peak absorption frequency of the dye molecules. The dipole radiates at the Stokes-shifted emission frequency of the dye molecules. A perfectly matched layer (PML) was used as the radiation boundary condition for the computational domain and the simulation had a mesh size of 0.5nm; 2% convergence was required for each calculation.

3.4 Results

3.4.1 Spherical Dimer

Calculations of the fluorescence enhancement and quenching of a single spherical metallic nanoantenna have been previously extensively investigated [2, 7, 25] yet it is useful to review briefly the fundamentals of this standard model system for an optical antennae photoresponse. For example, based on a quasi-static approximation [32], where the center of nanoparticle is located at the origin, the electric field near-field region due to a single spherical metallic nanoparticle is given as follows:

$$\mathbf{E}(r,\theta) = E_0(\cos\theta\mathbf{e_r} - \sin\theta\mathbf{e}_\theta) + \frac{\alpha(\omega)}{4\pi\epsilon_0}\frac{E_0}{r^3}(2\cos\theta\mathbf{e_r} + \sin\theta\mathbf{e}_\theta) \tag{3.9}$$

where $\mathbf{e_r}$ and $\mathbf{e}_\theta$ are the unit vectors in radial and polar directions, respectively; $\alpha(\omega)$ denotes the polarizability of the metal particle and r is the distance from the center of particle. The general expression for polarizability of the metal sphere [33] is

$$\alpha(\omega) = 4\pi\epsilon_o r_0^3 \frac{\epsilon_M(\omega) - \epsilon_D(\omega)}{\epsilon_M(\omega) + 2\epsilon_D(\omega)} \tag{3.10}$$

where ϵ_M and ϵ_D are the relative permittivity for metal and surrounding dielectric materials. We retain only the $l = 1$ spherical harmonics and consider only a particle radius r_0, such that $r_0 \ll \lambda$ (i.e. the dipole limit). Note that the plasmon polariton frequency is resonant when $Re\{\epsilon_M(\omega)\} + 2\epsilon_D(\omega) \approx 0$, which for a Au particles is at $\lambda \sim 500$nm. However, the strong ohmic loss in the vicinity of this wavelength reduces the overall fluorescence enhancement.

Now consider the simplest multiparticle ensemble, namely a dimer of two spherical nanoparticles. Our TCM calculations show that coupling between the two Au nanoparticles changes their optical properties, including a strong field enhancement and a down-shifting of the plasmon resonant frequency of the assembly, compared to the response of a single metal nanosphere. For a single Au spherical particle, the strongest enhancement occurs at 520nm [9], but for the Au dimer structure, the peak enhancement is, say, red shifted to 570nm (for a spherical-dimer with radius of 40nm), due to the lower plasmon resonant frequency. With this geometry, the enhanced intensity decreases as the spacing increases, which is demonstrated by the dashed line shown in Fig. 3.4(c). Note that this red-shifting has been previously introduced and reported in Refs. [34, 35] and this prior work on this model system was used to provide a validation of our model. Our TCM calculations show that the size of the Au nanospheres and the distance between their centers directly controls the magnitude of the red shift of the resonant wavelengths, a result also shown in prior work [15].

Finally, we add a cautionary note. Recently Nordlander [36] and Pendry [37] have studied quantum phenomena that occur when the surfaces of two Au particles are within sub-nanometer distances of each other. However, this near-contact case is not

the focus of our research here. Instead, we examine cases, in which the Au particles are separated by a surface-to-surface spacing, which is larger than 4nm. Therefore, near-contact effects, which become increasingly significant as separations decrease from 1 nm, such as quantum tunneling, are ignored in our calculations.

Numerical computation of enhancement and spectral shifts. Consider now our FDTD computations. The intensity enhancement of the excitation field obtained when illuminating with a *cw* source at the maximum absorption frequency of a dye molecule and in the presence of a dimer antenna is shown in Fig. 3.4(a); in this figure the dye molecule is located at the center of the spacing between the two spheres of the dimer. In addition, the incident field is, as shown, polarized parallel to the dimer axis. The numerical results of the antenna intensity enhancement of the emission field at the location of dye molecule with respect to the spacing between sphere particles are demonstrated in Fig. 3.4(c). Recall that in this chapter, in order to compare the dye/antenna assemblies uniformly, we fixed the volume of each Au particle in the dimer to be equal to that in a spherical antenna with a radius of 40nm, in which case, the spherical antenna has a plasmon resonant frequency that is peaked near the maximum excitation wavelength of $CF^{TM}568$. The fluorescence quenching, due to the ohmic losses of the dye/nanoantennae assemblies, has also been investigated. By treating the excited dye molecule as a dipole source (see Fig. 3.4b), we find that the dipole radiative decay rate is related to its surrounding environment and the non-radiative decay rate is proportional to the power absorbed by the Au particles; this dependence enables us to calculate the quantum yield for different dye molecules and dimer antennae of different dimensions. Figure 3.4(c) shows the overall quantum yield, q, for our three different dye molecules. As the spacing is reduced, the in-coupling coefficient from the radiating dye molecule to the Au particles increases. In particular, more of the optical energy emitted from each dye molecule is then dissipated through ohmic losses in the Au-particle antenna, thus causing a decreased

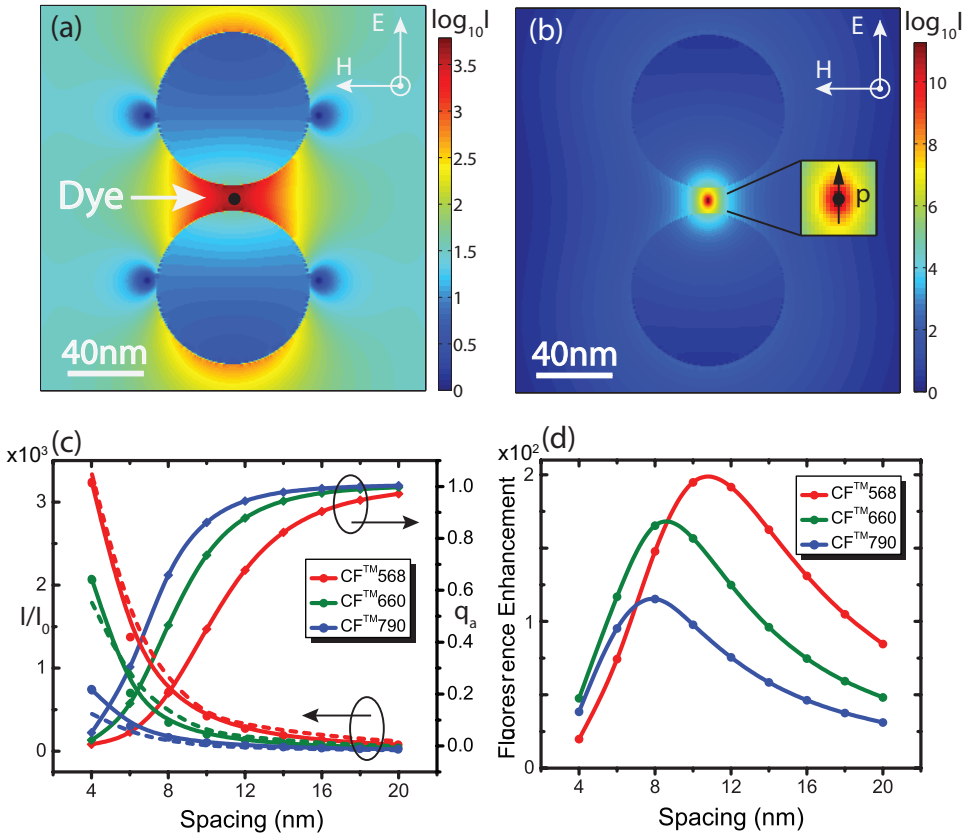

Figure 3.4: (a) Plot of the excitation electric field intensity distribution for a dye/dimer complex under illumination by a *cw* source at the maximum absorption frequency of dye molecules, i.e., 562nm. (b) The emission electric field intensity distribution for an excited $CF^{TM}568$ at its maximum emission frequency, i.e., 583nm. (c) A comparison of calculations of excitation rate $\gamma_{exc}/\gamma^o_{exc}$ using TCM theory (dashed lines) with calculated curves using FDTD (solid lines) for three dye molecoles. Also, the FDTD calculated quantum yield, q_a, as a function of dimer separation. (d) The calculated emission rate $\gamma_{em}/\gamma^o_{em}$ as a function of dimer separation for different dye molecules.

quantum yield. As shown in Eq. 3.1, the total fluorescence enhancement reflects the combined effects of excitation and quenching. In summary, for the aforementioned three dye molecules, we can achieve a 100-200 fluorescence enhancement by using spacings of 8-11.5nm. A plot of the performance of each dye/antenna type is given in Fig. 3.4(d).

Finally, as discussed in the previous section, standard TCM underestimates the antenna-intensity enhancement, especially when the interparticle spacing in the dimer is very small (<10nm). This underestimate is due to the fact that the isolated-sphere solution is used to calculate the overlap integral for intersphere coupling. In effect, this approach assumes that the polarizability α of each particle behaves as it would for an isolated particle, which in turn effects the value of γ_{rad}. We note, however, at such close spacing, we can treat the dimer pair as a single-dipole with an increased polarizability α_{pair} due to interactions between the original spheres. This approach has been described in [6] to model the enhancement behavior at close spacings. When this approach is used in the TCM framework, the results, as shown in Fig. 3.4(c) (dashed line), are in good agreement with our FDTD calculations.

3.4.2 Ellipsoid Dimer

In the previous section, it was shown that a spherical-dimer nanoantenna is well matched for enhancing the fluorescence efficiency of a $CF^{TM}568$ dye. To enhance fluorescence for a longer wavelength dye, such as $CF^{TM}660R$, the spherical shape was changed into an ellipsoid; the major axis of the ellipsoid nanoantenna was adjusted to match the plasmon resonance of the structure with the longer-wavelength emission peak of dye molecules, i.e., 663nm. This approach is based on insight from our TCM solution, which suggests that an ellipsoidal structure will yield a larger polarizability and stronger coupling coefficient at longer wavelength, thus allowing us to increase the intensity $|a|^2/|s_+|^2$. Hence, in this section, we use ellipsoid dimers and,

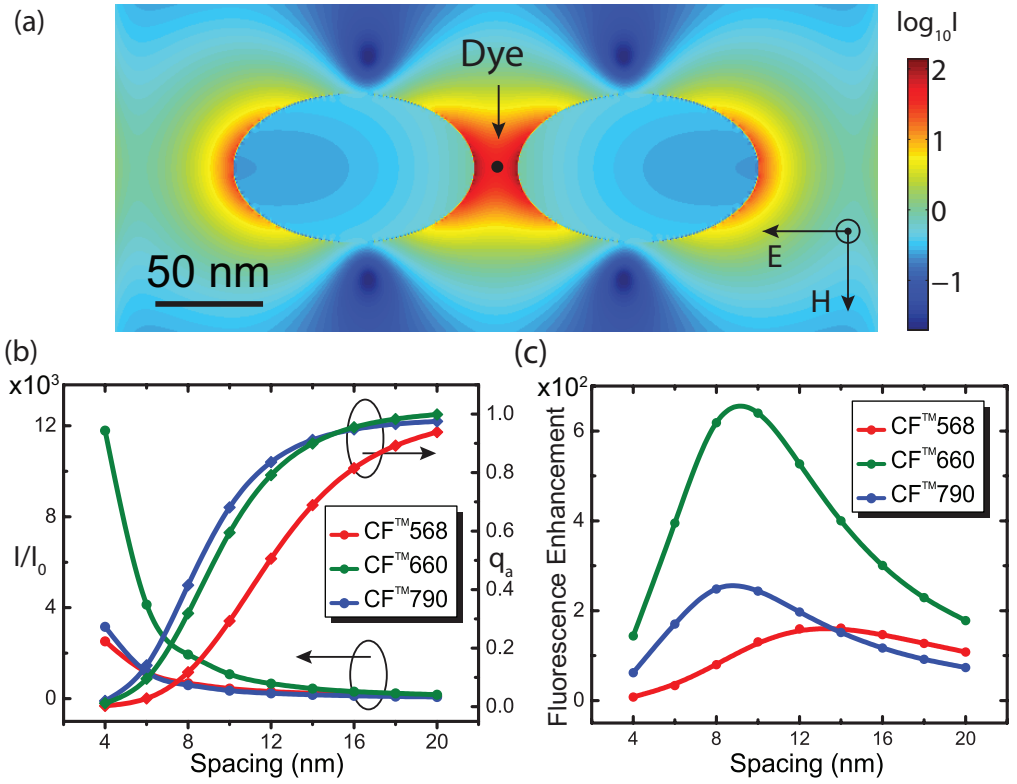

Figure 3.5: (a) The intensity distribution under illumination from a *cw* source, having the absorption wavelength of a specific dye molecule. (b) Calculated excitation rate, $\gamma_{exc}/\gamma^o_{exc}$, and quantum yield, q_a, as a function of dimer separation. (c) Calculated emission rate, $\gamma_{em}/\gamma^o_{em}$, as a function of dimer separation.

for simplification, focus on spheroids, which have two axes of equal length; therefore, only one geometrical factor is independent. From our results on spherical dimers, we recall that the dimer structure has 200× the fluorescence enhancement for $CF^{TM}568$ compared with its value for the molecule with no antenna, while the enhancement for $CF^{TM}660R$ is only 150× and only 100× for $CF^{TM}790$. The lower values for the last two dyes is due to the fact that the excitation wavelengths for the last two dyes are off-resonance for their emission wavelengths, as was shown in a notional way in Fig. 3.1. Thus we can achieve better fluorescence enhancement for dye molecules, simply by altering the shape of the nanoantennae to change its LSP mode.

Figure 3.5(a) shows the intensity distribution of a spheroid dimer under illumination by a *cw* source at the wavelength of maximum absorption for three dye molecules. In addition, for this figure, the major axis is aligned along the polarized E-field of incident light. The polarizability, α, of an isolated spheroid in a field parallel to its major axis is then

$$\alpha = 4\pi abc \frac{\epsilon_M - \epsilon_D}{3\epsilon_D + 3L(\epsilon_M - \epsilon_D)} \tag{3.11}$$

where a is its major axis and $b = c$ are its minor axes; ϵ_M and ϵ_D are the dielectric constants of the metal and the surrounding medium. An analytical expression for the geometrical factor L as a function of the eccentricity $e = \sqrt{1 - b^2/a^2}$ can then be found from [38]:

$$L = \frac{1 - e^2}{e^2} \left(-1 + \frac{1}{2e} \ln \frac{1 + e}{1 - e} \right) \tag{3.12}$$

Based on Eqs. 3.11, 3.12 and setting $a > b = c$, the choice of a longer major axis a will yield a smaller L, which will lead to stronger polarizability α. Based on the quasi-static approximation, the near-field enhancement of such a spheroid, in general, will be much larger than that of a sphere of comparable volume. In fact a larger enhancement is obtained in our calculation, as shown in Fig. 3.5(b). This result can also be seen from application of the TCM solution. In particular, since the spheroid's radiative mode is more directional than that of a sphere, the coupling

coefficient κ for the spheroidal dimer is also larger. Based on Eq. 3.8, the magnitude of a/s_+ will increase when κ is increased. In our simulations, our spheroid antenna was designed to be $a = 110.7nm$ and $b = c = 34nm$, since these dimensions yield a resonant frequency of 665nm. As shown in Fig. 3.5(c), this antenna structure has a 650× fluorescence enhancement for $CF^{TM}660R$ when the surface-to-surface spacing is 8nm. This result is more than 4× than for a spherical-dimer antenna. For $CF^{TM}790$, the spheroid still has a 250× fluorescence enhancement - that is about 3× times higher than that obtained when using a sphere. It is worth noting that a recent publication has reported an advanced fabrication capability that can synthesize a cylinder nanorod with round tip [39]. However, for our equivolume design rule, the cylinder dimer normally resonates in the range near 1500nm that is out of the range of commercial dye-molecule fluorescence. The fluorescence enhancement is thus very weak at our three selected dye wavelengths using a cylinder dimer and thus its use will not be discussed further here.

3.4.3 Bowtie

In order to efficiently fluoresce at the longest wavelength considered in this chapter, it was necessary to consider and examine a third dimer structure—the nanobowtie (triangle dimer). Using the same approach, the fluorescence enhancement of a bowtie nanoantenna was investigated, again with the same fixed volume of Au as was used for the spherical dimer discussed above. The choice of a bowtie to increase fluorescence enhancement at longer wavelengths was also motivated by the TCM theory. In particular, its strong near-field coupling and its large planar area cause it to have a stronger resonance at a longer wavelength than for the two antennae discussed above. Note also that its use has also been enabled by a recent development in advanced fabrication procedures [40, 41]. The bowtie has several features, which are qualitatively distinct from those of our other two nanodimers. One of these is its sharp

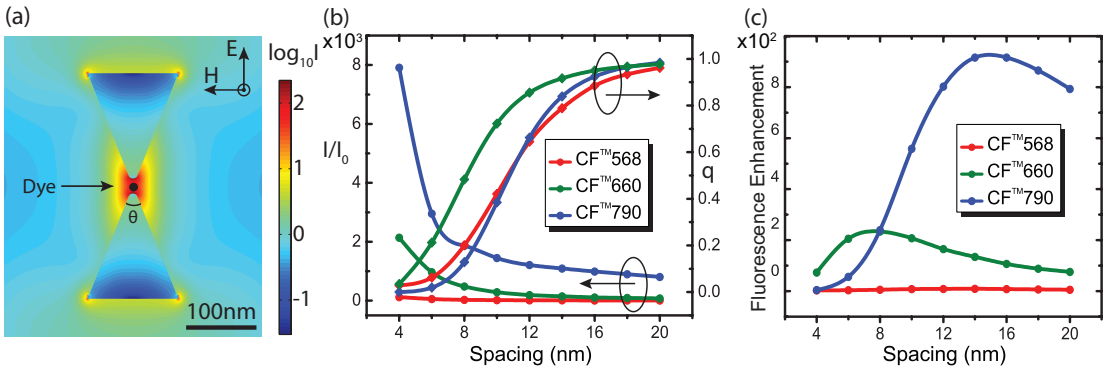

Figure 3.6: (a) The intensity distribution, I, due to the illumination of a *cw* source at the maximum absorption wavelength of the three dye molecules. (b) Calculated excitation rate, $\gamma_{exc}/\gamma^o_{exc}$, and quantum yield, q, as a function of dimer separation. (c) Calculated emission rate $\gamma_{em}/\gamma^o_{em}$ and as a function of dimer separation for different particle sizes.

point, which leads to a high directionality radiation. The second difference is that, for a fixed nanoparticle volume, the bowtie has a higher in-coupling coefficient κ_{in} and is resonant at longer wavelengths than for ellipsoids and spherical dimers. Based on Eq. 3.8; this high directionality in-coupling coefficient, κ, will further increase the field enhancement.

The intensity enhancement resulting from normal-incidence light impinging on a bowtie structure is shown in Fig. 3.6(a). Using our optimization procedure to scan through bowtie configurations with thicknesses from 20 to 40nm and angle θ from 30˚to 120˚, we find a local optimal enhancement structure of 30nm-thickness with a width of 120nm and a height of 149nm. As anticipated, the bowtie has a much stronger resonance at 800nm wavelength than at 560nm as indicated in Fig. 3.6(b). Although the quantum yield of the bowtie structure is comparable to that of the spherical dimers, the field enhancement of the bowtie dimer is stronger. From Fig. 3.6(c), we see that the optimal spacing between the bowtie tips for a $CF^{TM}790$ molecule is 14nm, which gives a 900× fluorescence enhancement compared with 150× fluorescence enhancement with a spherical dimer structure and 300× fluorescence enhancement with an ellipsoidal dimer. The enhancement for a $CF^{TM}660R$ dye using a bowtie dimer structure is comparable to that achieved with a spherical-dimer antenna, however as expected, the enhancement for a $CF^{TM}568$ dye is not significant. In summary, the bowtie structure is well matched to the near-IR fluorescent molecule.

3.5 Conclusion

In order to summarize our theoretical investigation of our three different choices of nanoantennae, we present our optimal fluorescence enhancement data for each configuration for the dye-molecules $CF^{TM}568$, $CF^{TM}660R$ and $CF^{TM}790$ in Table 3.1. As the table shows, there is an optimal antenna structure for high fluorescence enhance-

	Max. Fluorescence Enhancement		
	$CF^{TM}568$	$CF^{TM}660R$	$CF^{TM}790$
Sphere	200	170	115
Ellipsoid	160	650	250
Bowtie	10	235	920

Table 3.1: Summary of the maximum fluorescence enhancement for each dye molecule.

ment for each specific dye-molecule pair; this enhancement is due to the different plasmonic response and field coupling with variation in shape at each wavelength. Our results show that, based on TCM analysis, use of 3D FDTD computation of enhancement and metallic loss can provide accurate fluorescence enhancement calculations for arbitrary-shaped metal nanoparticle antennae. These results enable rational design of metallic nanoparticle complexes for maximum fluorescence enhancement. Thus with the help of our theoretical tools, it is possible to design assembles before synthesis and fabrication procedures, so as to achieve high performance. As computing hardware architecture advances, this method will soon be able to be implemented on a single desktop server with massively parallel processors and extensive memory.

3.6 References

[1] J. A. Schuller, E. S. Barnard, W. Cai, Y. C. Jun, J. S. White, and M. L. Brongersma, "Plasmonics for extreme light concentration and manipulation," *Nat. Mater.*, vol. 9, no. 3, pp. 193–204, 2010.

[2] P. Bharadwaj, B. Deutsch, and L. Novotny, "Optical antennas," *Adv. Opt. Photon.*, vol. 1, no. 3, pp. 438–483, 2009.

[3] X. Jiao and S. Blair, "Optical antenna design for fluorescence enhancement in the ultraviolet," *Opt. Express*, vol. 20, no. 28, pp. 29909–29922, 2012.

[4] B. B. Yousif and A. S. Samra, "Optical responses of plasmonic gold nanoantennas through numerical simulation," *J. Nanopart. Res.*, vol. 15, no. 1, pp. 1–15, 2013.

[5] C. Forestiere, A. Handin, and L. Dal Negro, "Enhancement of molecular fluorescence in the uv spectral range using aluminum nanoantennas," *Plasmonics*, pp. 1–11, 2014.

[6] M. Quinten, *Optical properties of nanoparticle systems: Mie and beyond*. Wiley, 2010.

[7] P. Anger, P. Bharadwaj, and L. Novotny, "Enhancement and quenching of single-molecule fluorescence," *Phys. Rev. Lett.*, vol. 96, no. 11, p. 113002, 2006.

[8] S. Kühn, U. Håkanson, L. Rogobete, and V. Sandoghdar, "Enhancement of single-molecule fluorescence using a gold nanoparticle as an optical nanoantenna," *Phys. Rev. Lett.*, vol. 97, no. 1, p. 017402, 2006.

[9] L. Novotny and B. Hecht, *Principles of nano-optics*. Cambridge University Press, 2006.

[10] D. Nykypanchuk, M. M. Maye, D. van der Lelie, and O. Gang, "Dna-guided crystallization of colloidal nanoparticles," *Nature (London)*, vol. 451, no. 7178, pp. 549–552, 2008.

[11] M. M. Maye, M. T. Kumara, D. Nykypanchuk, W. B. Sherman, and O. Gang, "Switching binary states of nanoparticle superlattices and dimer clusters by dna strands," *Nat. Nanotechnol.*, vol. 5, no. 2, pp. 116–120, 2009.

[12] H. Xiong, M. Y. Sfeir, and O. Gang, "Assembly, structure and optical response of three-dimensional dynamically tunable multicomponent superlattices," *Nano Lett.*, vol. 10, no. 11, pp. 4456–4462, 2010.

[13] S. Zhang, J. Zhou, Y.-S. Park, J. Rho, R. Singh, S. Nam, A. K. Azad, H.-T. Chen, X. Yin, A. J. Taylor, *et al.*, "Photoinduced handedness switching in terahertz chiral metamolecules," *Nat. Commun.*, vol. 3, p. 942, 2012.

[14] L. Huang, X. Chen, B. Bai, Q. Tan, G. Jin, T. Zentgraf, and S. Zhang, "Helicity dependent directional surface plasmon polariton excitation using a metasurface with interfacial phase discontinuity," *arXiv preprint arXiv:1304.1285*, 2013.

[15] H. A. Haus, *Waves and fields in optoelectronics*. Prentice-Hall Englewood Cliffs, NJ, 1984.

[16] R. L. Olmon, P. M. Krenz, A. C. Jones, G. D. Boreman, and M. B. Raschke, "Near-field imaging of optical antenna modes in the mid-infrared," *Opt. Express*, vol. 16, no. 25, pp. 20295–20305, 2008.

[17] A. C. Jones, R. L. Olmon, S. E. Skrabalak, B. J. Wiley, Y. N. Xia, and M. B. Raschke, "Mid-ir plasmonics: near-field imaging of coherent plasmon modes of silver nanowires," *Nano Lett.*, vol. 9, no. 7, pp. 2553–2558, 2009.

[18] J. R. Lakowicz, "Plasmonics in biology and plasmon-controlled fluorescence," *Plasmonics*, vol. 1, no. 1, pp. 5–33, 2006.

[19] X. Huang, P. K. Jain, I. H. El-Sayed, and M. A. El-Sayed, "Plasmonic photothermal therapy (pptt) using gold nanoparticles," *Laser Med. Sci.*, vol. 23, no. 3, pp. 217–228, 2008.

[20] L. Novotny and N. van Hulst, "Antennas for light," *Nat. Photon.*, vol. 5, no. 2, pp. 83–90, 2011.

[21] C. Min and G. Veronis, "Absorption switches in metal-dielectric-metal plasmonic waveguides," *Opt. Express*, vol. 17, no. 13, pp. 10757–10766, 2009.

[22] V. Valev, N. Smisdom, A. Silhanek, B. De Clercq, W. Gillijns, M. Ameloot, V. Moshchalkov, and T. Verbiest, "Plasmonic ratchet wheels: switching circular dichroism by arranging chiral nanostructures," *Nano Lett.*, vol. 9, no. 11, pp. 3945–3948, 2009.

[23] M. J. Huttunen, G. Bautista, M. Decker, S. Linden, M. Wegener, and M. Kauranen, "Nonlinear chiral imaging of subwavelength-sized twisted-cross gold nanodimers," *Opt. Mater. Express*, vol. 1, no. 1, pp. 46–56, 2011.

[24] J. Gersten and A. Nitzan, "Spectroscopic properties of molecules interacting with small dielectric particles," *J. Chem. Phys.*, vol. 75, no. 3, pp. 1139–1152, 1981.

[25] P. Bharadwaj, L. Novotny, *et al.*, "Spectral dependence of single molecule fluorescence enhancement," *Opt. Express*, vol. 15, no. 21, pp. 14266–14274, 2007.

[26] E. N. Economou, *Green's functions in quantum physics*, vol. 3. Springer, 1984.

[27] A. D. Rakic, A. B. Djurišic, J. M. Elazar, and M. L. Majewski, "Optical properties of metallic films for vertical-cavity optoelectronic devices," *Appl. Opt.*, vol. 37, pp. 5271–5283, Aug 1998.

[28] G. Veronis and S. Fan, "Overview of simulation techniques for plasmonic devices," *Surface plasmon nanophotonics*, pp. 169–182, 2007.

[29] C. Dyes, "Biotium inc.," *http://www.biotium.com/*, 2013.

[30] J. B. Khurgin, G. Sun, and R. Soref, "Practical limits of absorption enhancement near metal nanoparticles," *Appl. Phys. Lett.*, vol. 94, no. 7, pp. 071103–071103, 2009.

[31] J. B. Khurgin, G. Sun, and R. Soref, "Electroluminescence efficiency enhancement using metal nanoparticles," *Appl. Phys. Lett.*, vol. 93, no. 2, pp. 021120–021120, 2008.

[32] J. D. Jackson and R. F. Fox, "Classical electrodynamics," *Am. J. Phys.*, vol. 67, p. 841, 1999.

[33] J. Dadap, J. Shan, K. Eisenthal, and T. Heinz, "Second-harmonic rayleigh scattering from a sphere of centrosymmetric material," *Phys. Rev. Lett.*, vol. 83, no. 20, pp. 4045–4048, 1999.

[34] S. Oldenburg, R. Averitt, S. Westcott, and N. Halas, "Nanoengineering of optical resonances," *Chem. Phys. Lett.*, vol. 288, no. 2–4, pp. 243 – 247, 1998.

[35] B. Willingham, D. Brandl, and P. Nordlander, "Plasmon hybridization in nanorod dimers," *Appl. Phys. B*, vol. 93, no. 1, pp. 209–216, 2008.

[36] N. J. Halas, S. Lal, W.-S. Chang, S. Link, and P. Nordlander, "Plasmons in strongly coupled metallic nanostructures," *Chem. Rev.*, vol. 111, no. 6, pp. 3913–3961, 2011.

[37] D. Y. Lei, A. Aubry, Y. Luo, S. A. Maier, and J. B. Pendry, "Plasmonic interaction between overlapping nanowires," *ACS Nano.*, vol. 5, no. 1, pp. 597–607, 2010.

[38] C. F. Bohren and D. R. Huffman, *Absorption and scattering of light by small particles*. Wiley, 2008.

[39] P. Zijlstra, J. W. Chon, and M. Gu, "Five-dimensional optical recording mediated by surface plasmons in gold nanorods," *Nature (London)*, vol. 459, no. 7245, pp. 410–413, 2009.

[40] M. Rang, A. C. Jones, F. Zhou, Z.-Y. Li, B. J. Wiley, Y. Xia, and M. B. Raschke, "Optical near-field mapping of plasmonic nanoprisms," *Nano Lett.*, vol. 8, no. 10, pp. 3357–3363, 2008.

[41] A. Kinkhabwala, Z. Yu, S. Fan, Y. Avlasevich, K. Müllen, and W. Moerner, "Large single-molecule fluorescence enhancements produced by a bowtie nanoantenna," *Nat. Photon.*, vol. 3, no. 11, pp. 654–657, 2009.

Chapter 4

Plasmonic Enhancement of a Silicon-Vacancy Center in a Nanodiamond Crystal

Abstract

This work reports a rigorous and comprehensive three-dimensional electromagnetic computation to investigate and design photoluminescence enhancement from a single silicon-vacancy (SiV) center in a nanodiamond crystal embedded in various metallic nanoantennae, each having a different geometry. The study demonstrates how each antenna design enhances the photoluminescence of SiV centers in diamond. In particular, our report discusses how the 2D or 3D curvature of the nanoantenna and the control of the local environment of the SiV center can lead to significant field enhancement of its optical field. Our calculated optimal photoluminescence for each design enhances the emission intensity by 15-300× that of a single SiV center without antenna. The enhancement mechanisms are investigated using four representative structures that can be fabricated under feasible and realistic growth conditions, i.e., spherical-, nanorod-, nanodisk-dimer, and bowtie nanoantennae. These results demonstrate a method for rationally designing arbitrary metallic nanoantenna/emitter assemblies to achieve optimal SiV center photoluminescence.

4.1 Introduction

Diamond has emerged as an important materials platform and a distinct photonics approach to quantum information processing [1]. This approach is based on the fact that pre-selected nanodiamond crystals containing single defect centers are good candidates for single-photon sources due to their stable photoluminescence (PL), spin-sensitive optical transitions, and long electron-spin-coherence lifetimes [2, 3]. These attributes have also led to the investigation of single defect centers within nanodiamond crystals for applications other than quantum information processing, which include biomedical sensing and biological imaging [4]. However, the optical and radiative properties of these defect centers are certainly far from ideal. For example, due to the high refractive index of nanodiamond crystals, the coupling to the electromagnetic field is weak compared to other systems such as dye molecules or quantum dots in typically lower index hosts [5]. As a result, only a small fraction of the available radiation can be collected and thus the PL efficiency of the process is low. Thus the spontaneous emission rate of defect centers requires a systematic study of the enhancement for the environments of these specific applications and their different integrated forms. This enhancement can be realized by employing the Purcell effect, i.e., by modifying the spontaneous emission rate of the emitters (in our case, the defect centers in diamond) via interaction with the optical density of states of the environment. Several groups have reported studies based on Purcell enhancement by coupling defect centers to plasmonic or dielectric resonators, including plasmonic structures [6, 7], dielectric microdisks [8], and photonic crystal cavities [2, 9].

In this work, we report a *systematic* investigation if the radiative enhancement of a single silicon-vacancy (SiV) center inside a high-refractive-index nanodiamond crystal with four possible metallic nanoantennae geometries. The work in our paper makes use of advanced computational methods using a cluster computer to access fully three dimensional finite difference time domain (3D-FDTD) calculations. The

work is distinctive in that it provides a systematic set of calculations with four different nanoantennae based on 3D calculation for the important case of nanodiamond emitters. The work thus allows comparison of the enhancement in photoluminescence for these four different antenna designs. In the following section, we provide a design procedure for use with nanoantennae assemblies before synthesis or fabrication, as well as a general understanding of antenna-emitter interactions that is useful for experimental efforts to achieve the optimal enhancement of photoluminescence.

4.2 Theoretical considerations

The goal of our study is to provide a general approach to designing nanoantennae for efficient quantum emitters, such as single-photon sources. Our work focuses on a nanodiamond crystal containing a SiV center in the near-field of a Au nanoantennae. A SiV center is chosen for this study due to its narrow zero-phonon-line width and its low phonon coupling. In addition, its near-infrared emission at 738nm is in a spectral region such that the background fluorescence of the surrounding diamond material is weak and the metallic ohmic loss is small [10]. Note, however, that the general design principles reported here apply for other defect centers in nanodiamond.

Here, a open-source 3D-FDTD numerical computation program, MEEP, is used [11] to analyze an emitter having an arbitrary nanoantenna geometry with high accuracy and simple implementation. The algorithm consists of first discretizing Maxwell equations on a 3D grid and then, starting from a given set of initial conditions, marching a set of iterative relations forward in time. With a suitably refined computational grid, the corresponding numerical solution gives an accurate representation of the dynamics of the electromagnetic field. The extensive 3D computational requirements were satisfied using a parallel implementation of the MEEP package running on Linux clusters at the Center for Functional Nanomaterials, Brookhaven National

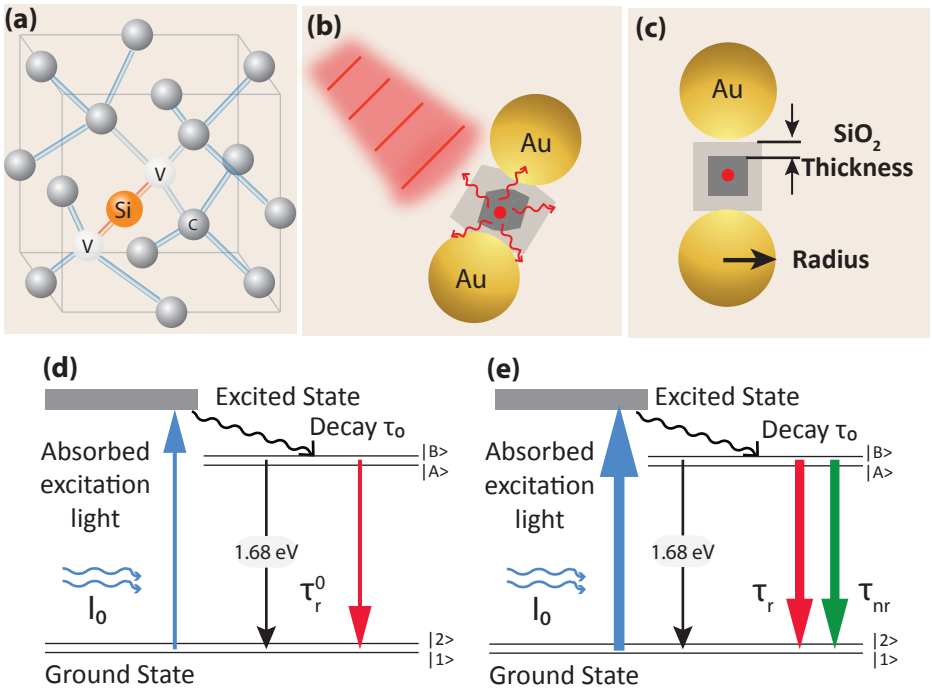

Figure 4.1: (a) Atomic structure for SiV center inside nanodiamond crystal. (b) The nanodiamond in the near field of a dimer metal nanoantennae, illuminated by a monochromatic optical source. (c) Cross section view: nanodiamond crystal (dark gray), SiV center (red), and SiO_2 (light gray) that has a thickness, d, and each of the spherical particles in the Au dimer has a radius r. (d)-(e) Excitation and relaxation processes of the SiV center under 532nm excitation in (d) free space and (e) near the metallic nanoantennae.

Laboratory. The MEEP package was controlled externally with our multi-parameter optimization algorithm, which implements the automatic procedures for design optimization. In our simulations, a perfectly matched layer was used as the boundary condition for the computational domain and the simulation had a mesh size of 1 nm to achieve convergent results.

The atomic structure of an example of such a SiV center is shown in Fig. 4.1(a), where its approximate energy level has a 1.68 eV band gap [12]. The diamond-antennae system is then illuminated by a monochromatic optical source, as illustrated in Fig. 4.1(b). A cross-section view of a sample antenna assembly is shown in Fig. 4.1(c), where the nanodiamond crystal (dark gray) is coated with an SiO_2 thin film (light gray) of thickness d and each Au-dimer sphere has a radius r. The incident light intensity, I_0, can then excite the SiV center inside the nanodiamond crystal, where its *location* is denoted by a red dot shown in Fig. 4.1(c). If the defect center is located within the near field of the metal antenna, localized surface plasmons (LSP) within the metal object can enhance any relevant optical process [13–15]. In effect, the metal antenna causes a much stronger local field to form at the position of the SiV center due to excitation of localized surface plasmons, resulting in stronger optical excitation of the SiV center.

The excited SiV center in free space yields photoluminescence with a radiative lifetime of τ_{r}^0, while the excited SiV center near a metallic nanoantennae gives enhanced PL and a radiative lifetime of τ_{r} as indicated in Fig. 4.1(d). Note also that ohmic loss within the metal nanoantennae gives an additional non-radiative channel with a non-radiative decay rate of τ_{nr} that is not present in an isolated defect center, which is shown in Fig. 4.1(e). Considering these processes, we can express the PL emission rate γ_{em} of a single SiV center as the product of an excitation rate γ_{exc} and the associated quantum yield q, i.e.,

$$\gamma_{\mathrm{em}} = \gamma_{\mathrm{exc}} \cdot q, \tag{4.1}$$

where q is defined as the ratio of radiative transition rate (from excited to ground state) to the total decay rate. Thus nonradiative quenching lowers q. It is sufficient to treat the excitation and emission processes independently since there is no coherence between the two processes [16].

For our initial analysis, our computation considers the weak excitation regime. This restriction allows us to avoid treating phenomena such as thermal runaway or light-induced phase changes in the nanoantennae [17]. In effect, only linear excitation processes are thus considered, hence the excitation rate of the SiV center in the diamond is directly proportional to the number of incident photons, i.e., the incident intensity of the field, which is proportional to $|E|^2$. The normalized excitation rate γ_{exc} then be expressed as

$$\gamma_{\text{exc}} = \frac{|\mathbf{E}(\mathbf{r})|^2}{|\mathbf{E_0}(\mathbf{r})|^2} \tag{4.2}$$

where $\mathbf{E}(\mathbf{r})$ and $\mathbf{E_0}(\mathbf{r})$ are the electric-fields for a specific optical frequency ω at location $\mathbf{r}$ of the SiV center with and without the presence of the antennae, respectively. In addition, we chose 532 nm as the excitation wavelength because this is an easily accessible wavelength experimentally (via frequency doubling of a YAG laser output) and it is widely used by experimentalists for studying the optical properties of SiV centers [18, 19]. Alternatively, tunable sources such as an optical parametric oscillator or an optical parametric amplifier may be used for resonance enhancement.

To obtain the quantum yield q of the system, the SiV center is modeled as a point dipole emitter inside a nanodiamond crystal [6]. Furthermore, the wavelength of the dipole emission is set to be the emission wavelength of the SiV center. Since the placement of nanoantennae increases its local optical density of states ρ, the radiative decay rate γ_r will change, compared to its value in free space, in accord with Fermi's Golden Rule,

$$\Gamma_{i\to f} = \frac{2\pi}{\hbar} |\langle f| H |i\rangle|^2 \rho \tag{4.3}$$

where $\hbar$ is the reduced Planck's constant and H is the time-dependent Hamiltonian,

given by $H = -\mathbf{E} \cdot \mathbf{p}$, due to the photon field $\mathbf{E}$ and dipole moment $\mathbf{p}$, and $|i\rangle$, $\langle f|$ denote the initial and final states, respectively.

Figure 4.2(a) shows an example of our simulation model, for which the nanoantenna and its nanodiamond host were illuminated with a *cw* plane-wave source. The excitation rate was calculated using the electric-field intensity at the location of the SiV center. The excited SiV center radiates at its zero-phonon line frequency. The computation thus considers the defect and its related transition as an atomic system immersed in a dielectric continuum [20, 21]. The analysis, as also discussed in [16], shows that the radiative and nonradiative rates, γ_{r} and γ_{nr}, are proportional to the power radiated by the classical dipole in the presence of metal nanoantennae, P_{r}, and the power absorbed by the metal nanoantennae due to ohmic loss, P_{nr}. The quantum yield can then be calculated using the expression $q = P_{\mathrm{r}}/(P_{\mathrm{r}} + P_{\mathrm{nr}})$ by measuring the net power flowing through a suitably chosen closed surface with integration over this surface and then averaged over time. As indicated in Fig. 4.2(b), the time-averaged power flow by the SiV center in the presence of metal nanoantennae is noted as $P_{\mathrm{i}} = P_{\mathrm{r}} + P_{\mathrm{nr}}$ and the power absorbed by the metal nanoantennae due to ohmic loss is $P_{\mathrm{nr}} = P_{\mathrm{i}} - P_{\mathrm{r}}$. The quantum yield, q, can also be expressed as $q = P_{\mathrm{r}}/P_{\mathrm{i}}$.

The nanodiamond crystal is modeled as a cubic structure based on the experimentally measured TEM image, where the cube has a side dimension of 10 nm and has a refractive index of 5.86 [22]. In addition, prior theoretical treatment shows that the shape and size of nanodiamond crystal as well as its environment affect the optical properties of its defect centers and, in fact, nominally identical nanocrystals can have a high variance of intrinsic quantum efficiencies [23]. As a result, in our simulations, we neglect these effects for simplicity and assume that a nanodiamond is preselected to contain a single SiV center with well-defined orientation [24]. The orientation of its dipole moment is assumed to be parallel to the symmetry axis of the nanoantenna [25].

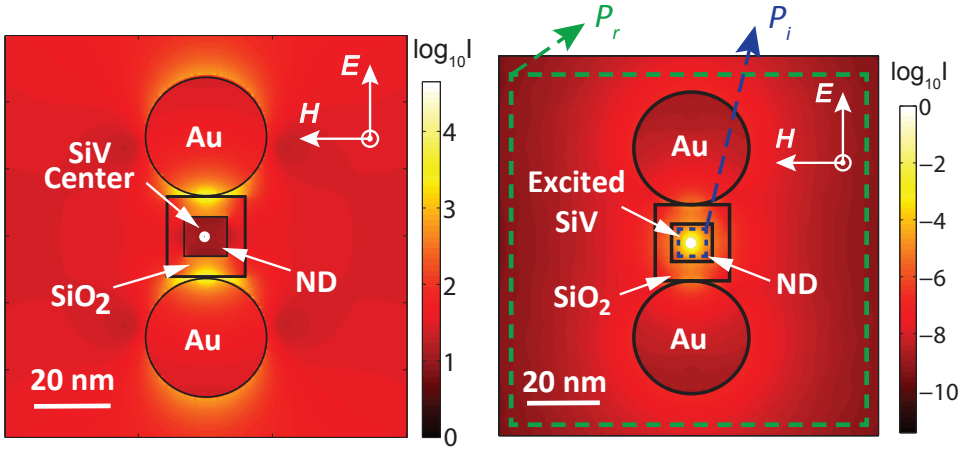

Figure 4.2: (a) The excitation intensity profile of the diamond-antennae system under the illumination of a *cw* source at 532 nm. (b) The emission intensity profile for an excited SiV center at its emission frequency. The excited SiV center inside the nanodiamond crystal is modeled as a classical dipole. The quantum yield is then obtained by measuring the power emitted from the dipole (P_{i}) arising from the region denoted by the blue dashed-line box inside the nanodiamond host and power emitted from the dipole-nanoantennae system (P_{r}), denoted by the green dashed box.

4.3 Numerical results and discussion

In the following sections, we investigate the design and efficacy of nanodiamond PL enhancement using different nanoantenna geometries. These geometries can be generally classified into two categories. In the first category, the nanoantenna has a 3D curvature, e.g., nanospheres or nanorods. This type of nanoantennae can, in general, be fabricated through a "bottom-up"assembly procedure or under colloidal chemical growth conditions [26]. The nanodiamond crystal with a thin layer of SiO_2 coating can be positioned near the nanoantennae through surface chemistry methods [27–29]. The second category of nanoantennae is fabricated from a thin film and thus has flat top and botom surfaces. Such plasmonic nanostructures can be fabricated precisely, including electing to have a periodic arrangement, through "top-down"techniques such as electron beam lithography [30] or focused-ion-beam milling [31]. Note that due to the small size of the nanoantenna's hotspot, achieving the degree of enhancement is very sensitive to the diamond alignment. However, improved positioning techniques now being realized in advanced alignment methods [32] would facilitate a satisfactory alignment for the nanodiamond to achieve near optimal enhancement.

Our approach here is to calculate the optical performance and properties of these two classes of basic antenna with 2D and 3D curved surfaces. Note that for all antennae geometries, a dimer configuration is selected and its major axis is aligned parallel to the incident field polarization. This results in strong coupling of the field to the antenna, creating a strong LSP mode in the two dimer components [33, 34].

4.3.1 Nanoantennae with 3D curvature

We now consider the spherical dimer nanoantenna with a nanodiamond crystal. This particular antenna also serves as a prototype to illustrate our computational method as well as the antenna's sensitivity to various geometric properties. A cal-

culation of the intensity enhancement from such a diamond/antennae system, under typical conditions and with a typical geometry is shown in Fig. 4.3(a). The nanodiamond is assumed to be bonded to the nanoantennae through a thin layer of SiO_2 and the incident field is polarized parallel to the dimer axis. In many cases, these nanoantennae are supported by very low index materials [35] and thus we have assumed an effective index of 1.0 for the supporting medium. This condition also applies to the nanorod configuration discussed below.

The optical response of this structure can now be investigated with our computational method. The excitation of the localized surface plasmon and the quenching due to ohmic losses in the antennae were separately investigated. The numerical results for the PL enhancement of the SiV center and its dependence on the radius of the Au spheres and the thickness of SiO_2 coating are plotted in Fig. 4.3(b), from which we can find the optimized parameters corresponding to the maximum PL enhancement. For our wavelength, the peak response of the spherical dimer corresponds to a 65 nm radius in the presence of a 2nm-thick-SiO_2 coating on the nanodiamond crystal. This peak PL enhancement is more than 300×. A contour plot of the PL enhancement is also shown under the three-dimensional shaded surface in Fig. 4.3(b).

Note that in our numerical investigation, for 532 nm excitation, the overall PL enhancement drops when the sphere radius is larger than 65 nm. However, it is known that the field enhancement should be higher in the subwavelength regime when the radius of spherical nanoparticle increases, due to its stronger polarizability. Here, the PL enhancement drops due to the mismatch between the excitation wavelength and the size of the antennae, as well as due to the increased ohmic loss. Our calculations also show, as suggested in prior work, that the size of the gold nanospheres and the thickness of the SiO_2, which are used here to precisely adjust the distance between nanosphere centers, directly controls the magnitude of the PL enhancement [36].

Our second antenna type is a nanowire, or cylindrical-nanorod, dimer. This an-

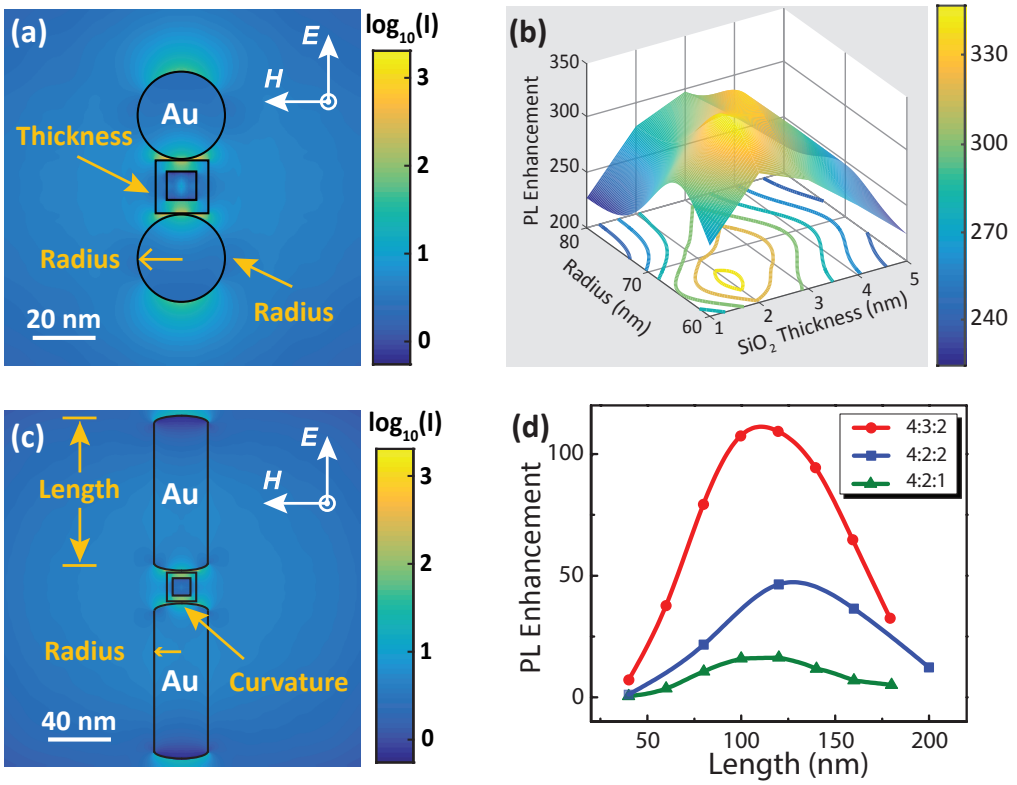

Figure 4.3: (a) Plot of the excitation field intensity distribution of the cross section of a nanodiamond/spherical dimer complex under illumination by a *cw* source ($\lambda = 532\,\text{nm}$). (b) Plot of PL enhancement as a function of the radius of the spherical nanoparticle and the thickness of the SiO_2 layer coating. A contour plot also shows the PL enhancement of the SiV center. (c) Plot of the intensity distribution of the cross section of a diamond/nanorod dimer complex under illumination by a *cw* source ($\lambda = 532\,\text{nm}$). The nanorod is a cylinder with a spherical cap. (d) The PL enhancements, calculated as a function of length of the nanorods, with aspect ratios (length:radius:curvature) of 4:3:2, 4:2:2 and 4:2:1.

tenna can be viewed as a result of a one dimensional variation in length of a nanospherical dimer along one axis. This antenna geometry, which can be fabricated using wet-chemical methods, has been frequently investigated because of its applications to nano or quantum wires [16, 37]. In order to compare the results of this antenna with that of the nanosphere antenna, our nanorod dimer is terminated with spherical caps on each end. Each cylindrical nanorod has a length, L, a body radius, r, and a curvature radius, ρ, of the spherical cap at the end of the rod. Again, it is assumed that the nano-rod axis is aligned along the polarized E-field of the incident light. Figure 4.3(c) shows the intensity distribution from a typical structure of a nanorod with a length of 100 nm. This structure has also been thoroughly explored with our optimization algorithm in order to obtain the peak PL enhancement for nanorod dimer lengths in the 40 nm to 200 nm range for selected aspect ratios ($L : 2r : \rho$), namely, 4:3:2, 4:2:2 and 4:2:1, and assuming a SiO_2 layer of 2 nm thickness. The calculated PL enhancements are shown in Fig. 4.3(d), where see that the resonance peak position is related to the cylinder-length-to-radius ratio ($L : r$). It was also found that the magnitude of the enhancement depends sensitively on the curvature radius ρ of the rod end, since the curvature radius can significantly modify its polarizability. Our results also show that nanorod dimers can lead to photoluminescence enhancements of more than 100×. In addition, it was found that the optimal length of each nanorod is approximately 120 nm, in which case the entire length of the nanorod dimer is about 250 nm, which acts as a halfwave antenna. Note that the radius of the cylindrical nanorod also has an important role for the field enhancement, since we find that a larger radius leads to a higher enhancement. However, the PL enhancement of the nanorod dimer, in general, is lower than that of the spherical dimer due to the smaller dipole polarizability of nanorod.

4.3.2 Nanoantennae with 2D curvature

The third and fourth structural motif that we examined are both fabricated via thin film methods and thus possess flat top and bottom faces [38, 39]. Despite their near two dimensional geometry, these antenna structures have finite thickness and must be analyzed with 3D FDTD methods for accurate simulation. These structures can be fabricated using advanced patterning technologies and can readily be patterned to form an array [40, 41]. Antenna arrays containing nanodiamonds have been of interest as single-photon sources [42, 43], which are particularly important for quantum information processing. Consider now, as an example, the nanodisk dimer antenna, which constitutes our third antenna structure. This structure is essentially a flattened version of the nanosphere antenna discussed earlier. Our FDTD method can be immediately applied to calculate the intensity distribution of this structure; an example is shown in Fig. 4.4(a), which is the cross section of cylindrical nanodisks with 20 nm radius and 20 nm disk height on top of a SiO_2 substrate. Using the same computational approach as above, we investigated the PL enhancement of this nanodisk dimer for different combinations of parameters including dimer separation, disk radius, and disk height. We find that the height of the disk had a negligible impact on the resulting PL enhancement in the range of 20 nm to 40 nm. This effect is due to the thin (i.e., $\ll \lambda$) film nature of the structure, as well as the nearly uniform enhancement of the field in the gap. Thus the disk height was fixed at 30 nm to investigate the antenna performance for different parameters. Figure 4.4(b) shows that a maximum enhancement is reached in PL when the disk radius is at 50 nm. The gap size between the nanodisk and nanodiamond surfaces can also modify the magnitude of enhancement. Thus by varying this radius, we found that more than a 25-fold enhancement of the PL signals could be realized.

Finally, a bowtie shaped nanoantennae was investigated as our fourth antenna structure [44, 45]. This antennae was chosen due to its known ultra-confined LSP

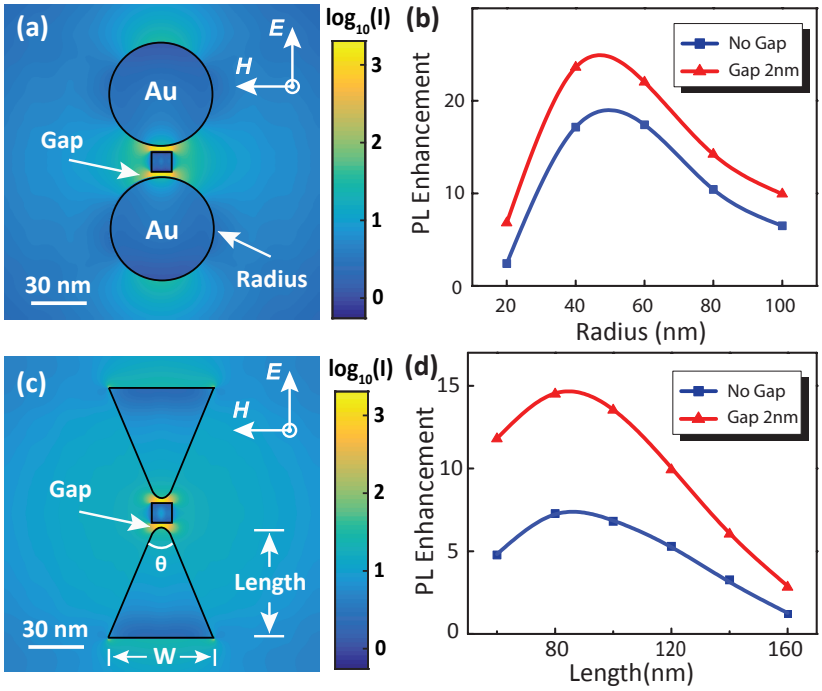

Figure 4.4: (a) Plot of the intensity distribution of a cross section of a diamond/nanodisk dimer complex under illumination by a *cw* source ($\lambda = 532\,\text{nm}$). (b) Plot of the PL enhancement as a function of radius of the nanodisks, with a fixed disk height of 30 nm. (c) Plot of the intensity distribution of the cross section of a diamond/nanobowtie complex under illumination by the same *cw* source. The nanobowtie is modeled as a triangular disk, which is terminated such that the pointed tip has a finite radius. (d) Plot of the PL enhancement as a function of length of the bowtie antenna between 60-160 nm, with the disk thickness to be constant at 30 nm, $\theta = 60^\circ$ and the base W to be 60nm.

mode and highly directional coupling. The quality and geometry of these antennae have also benefited from recent developments in advanced lithographic processing. With regard to our simulations, a typical intensity enhancement resulting from normal-incidence light impinging on a bowtie structure is shown in Fig. 4.4(c), where each triangular component has a 60 nm base and an 80 nm height. Note that the sharp tip end is assumed to be rounded with a radius of 5 nm and electric field intensity is strongly enhanced at this relatively sharp end. In addition, our optimization procedure was used for a range of bowtie geometries. This procedure allows examining length from 60 nm to 160 nm and angles θ from 30° to 60° in order to find a locally optimized structure. As in the case of the circular disk, the thickness of the bowtie structure was found to have negligible impact on the PL enhancement. Figure 4.4(d) shows the enhancement profile for a structure of 30 nm thickness. Due to its sharpness and the ultra-confined near-field enhancement, we can achieve approximately 15× enhancement of the PL signals. These results are consistent with a previous study, where a bowtie structure was reported to have its stronger response in the near infrared instead of the visible spectrum [36, 45].

Finally, we note that, in addition to the above investigation, we have examined the effect of other materials-based changes in the antennae/nanocrystal structure. For example, one important issue involves the addition of a thin-layer coating of a relatively low-dielectric materials such as SiO_2 on the nanodiamond crystal surface. Figure 4.5 (a) and (b) shows the PL enhancement from a SiV center via both spherical and nanodisk dimers. The figure thus involves a nanoantennae structures on either a 3D curvature or a flat-3D surface (2D curvature). In both cases, our calculations showed that having a thin-layer SiO_2 coating outside nanodiamond crystal leads to a more than 3-fold improvement. This increase is due to the fact that the thin-layer SiO_2 coating reduces the highly index-mismatched boundary at the nanodiamond surfaces thereby increasing the electromagnetic coupling with the nanodiamond crystal.

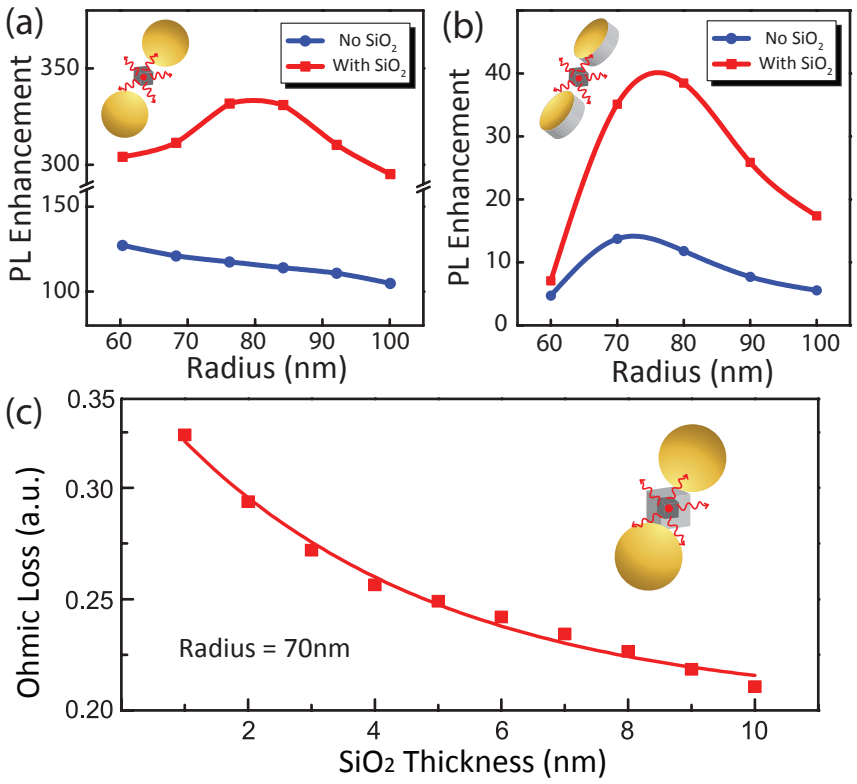

Figure 4.5: Plot of the PL enhancement as a function of the radius of the spherical (a) and nanodisk (b) dimers both with and without SiO_2 between antennae and diamond surfaces. (c) The normalized ohmic loss for the spherical dimer as the function of SiO_2 dielectric coating thickness.

Table 4.1: Comparison of optimal signal stength from four general nanoantennae structures

	Photoluminescence Enhancement			
3D	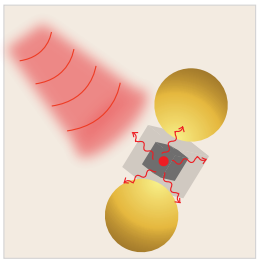	~300	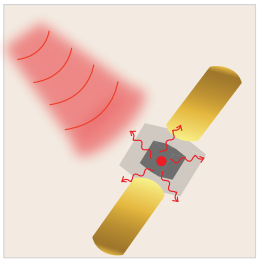	~50
Flat - 3D	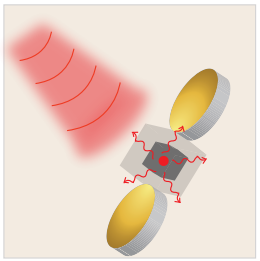	~25	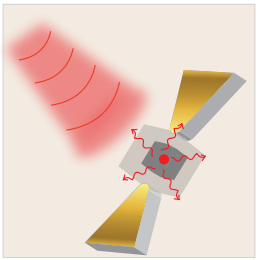	~15

Before we conclude, we briefly discuss the role of the ohmic loss. It is not readily apparent how the strength of ohmic loss varies from one shape to another or even as a function of size of the antenna for a given shape. It depends primarily on the radiation coupling to the nanoantenna structure, as well as the overlap between the antenna structure and it plasmonic mode. However, a simple case in which the trend for the ohmic loss variation becomes obvious is its dependence on separation between the two antenna elements. Figure 4.5 (c), for example, shows the ohmic loss (normalized to the total input power) as a function of the SiO_2 thickness for the spherical dimer antenna. The ohmic loss decreases as the SiO_2 thickness, and concomitantly the separation of the spheres, increases.

4.4 Conclusion

Our work here demonstrates that it is possible to systematically design and optimize a nanoantenna/ nanodiamond structure with SiV center photoluminescence greatly enhanced over that from a free standing nanodiamond object with no antennae. A summary of our theoretical investigation of two general classes (3D and flat-3D) of nanoantennae is presented in Table 4.1. Specifically this figure presents the optimal PL enhancement from a SiV center in a nanodiamond crystal for each configuration in the table. The PL enhancement of each optimized nanoantennae configuration arises from the complex interplay of plasmonic resonance and ohmic loss, whose effects are modulated by the nanoantennae geometry and the local dielectric environment. The table below illustrates, for each optimal antennae configuration, that PL enhancement factors range from about 15 to larger than 300 fold. From a more general perspective, our results also show that the use of 3D FDTD computation of optical enhancement and metallic loss can provide accurate PL enhancement calculations for arbitrary-shaped metal nanoparticle antennae. These results enable rational

design of metallic nanoparticle complexes and provide guidance in determining optimized parameters that depend directly on the materials employed for maximum PL enhancement. Thus with the help of our theoretical tools, it is possible to design assemblies before synthesis and fabrication, so as to achieve high performance. Such a design procedure is useful both for general understanding of emitter-metal structure interaction and experimental efforts in plasmonic nanomaterials applications.

4.5 References

[1] I. Aharonovich and E. Neu, "Diamond nanophotonics," *Adv. Optical Mater.*, vol. 2, no. 10, pp. 911–928, 2014.

[2] J. Wolters, A. W. Schell, G. Kewes, N. Nusse, M. Schoengen, H. Doscher, T. Hannappel, B. Lochel, M. Barth, and O. Benson, "Enhancement of the zero phonon line emission from a single nitrogen vacancy center in a nanodiamond via coupling to a photonic crystal cavity," *Appl. Phys. Lett.*, vol. 97, no. 14, pp. 141108–141108, 2010.

[3] C. Bradac, T. Gaebel, N. Naidoo, M. Sellars, J. Twamley, L. Brown, A. Barnard, T. Plakhotnik, A. Zvyagin, and J. Rabeau, "Observation and control of blinking nitrogen-vacancy centres in discrete nanodiamonds," *Nat. Nanotechnol.*, vol. 5, no. 5, pp. 345–349, 2010.

[4] Y.-R. Chang, H.-Y. Lee, K. Chen, C.-C. Chang, D.-S. Tsai, C.-C. Fu, T.-S. Lim, Y.-K. Tzeng, C.-Y. Fang, C.-C. Han, *et al.*, "Mass production and dynamic imaging of fluorescent nanodiamonds," *Nat. Nanotechnol.*, vol. 3, no. 5, pp. 284–288, 2008.

[5] K. Hennessy, A. Badolato, M. Winger, D. Gerace, M. Atatüre, S. Gulde, S. Fält, E. L. Hu, and A. Imamoğlu, "Quantum nature of a strongly coupled single

quantum dot–cavity system," *Nature (London)*, vol. 445, no. 7130, pp. 896–899, 2007.

[6] S. Schietinger, M. Barth, T. Aichele, and O. Benson, "Plasmon-enhanced single photon emission from a nanoassembled metal- diamond hybrid structure at room temperature," *Nano Lett.*, vol. 9, no. 4, pp. 1694–1698, 2009.

[7] J. T. Choy, B. J. Hausmann, T. M. Babinec, I. Bulu, M. Khan, P. Maletinsky, A. Yacoby, and M. Lončar, "Enhanced single-photon emission from a diamond-silver aperture," *Nat. Photon.*, vol. 5, no. 12, pp. 738–743, 2011.

[8] P. E. Barclay, K.-M. C. Fu, C. Santori, and R. G. Beausoleil, "Chip-based microcavities coupled to nitrogen-vacancy centers in single crystal diamond," *Appl. Phys. Lett.*, vol. 95, no. 19, p. 191115, 2009.

[9] D. Englund, B. Shields, K. Rivoire, F. Hatami, J. Vuckovic, H. Park, and M. D. Lukin, "Deterministic coupling of a single nitrogen vacancy center to a photonic crystal cavity," *Nano Lett.*, vol. 10, no. 10, pp. 3922–3926, 2010.

[10] T. Müller, C. Hepp, B. Pingault, E. Neu, S. Gsell, M. Schreck, H. Sternschulte, D. Steinmüller-Nethl, C. Becher, and M. Atatüre, "Optical signatures of silicon-vacancy spins in diamond," *Nat. Commun.*, vol. 5, 2014.

[11] A. F. Oskooi, D. Roundy, M. Ibanescu, P. Bermel, J. D. Joannopoulos, and S. G. Johnson, "Meep: A flexible free-software package for electromagnetic simulations by the fdtd method," *Comput. Phys. Commun.*, vol. 181, no. 3, pp. 687–702, 2010.

[12] I. I. Vlasov, A. S. Barnard, V. G. Ralchenko, O. I. Lebedev, M. V. Kanzyuba, A. V. Saveliev, V. I. Konov, and E. Goovaerts, "Nanodiamond photoemitters based on strong narrow-band luminescence from silicon-vacancy defects," *Adv. Mater.*, vol. 21, no. 7, pp. 808–812, 2009.

[13] C. Liow, F. Meng, X. Chen, and S. Li, "Dependence of plasmonic properties on electron densities for various coupled au nanostructures," *J. Phys. Chem. C*, vol. 118, no. 47, pp. 27531–27538, 2014.

[14] C. Ciracì, A. Rose, C. Argyropoulos, and D. R. Smith, "Numerical studies of the modification of photodynamic processes by film-coupled plasmonic nanoparticles," *J. Opt. Soc. Am. B*, vol. 31, no. 11, pp. 2601–2607, 2014.

[15] A. Li, S. Isaacs, I. Abdulhalim, and S. Li, "Ultrahigh enhancement of electromagnetic fields by exciting localized with extended surface plasmons," *arXiv preprint arXiv:1507.00311*, 2015.

[16] P. Anger, P. Bharadwaj, and L. Novotny, "Enhancement and quenching of single-molecule fluorescence," *Phys. Rev. Lett.*, vol. 96, no. 11, p. 113002, 2006.

[17] J. Wolters, G. Kewes, A. W. Schell, N. Nüsse, M. Schoengen, B. Löchel, T. Hanke, R. Bratschitsch, A. Leitenstorfer, T. Aichele, *et al.*, "Coupling of single nitrogen-vacancy defect centers in diamond nanocrystals to optical antennas and photonic crystal cavities," *Phys. Status Solidi B*, vol. 249, no. 5, pp. 918–924, 2012.

[18] L. J. Rogers, K. D. Jahnke, T. Teraji, L. Marseglia, C. Müller, B. Naydenov, H. Schauffert, C. Kranz, J. Isoya, L. P. McGuinness, *et al.*, "Multiple intrinsically identical single photon emitters in the solid-state," *Nat. Commun.*, vol. 5, 2014.

[19] K. D. Jahnke, A. Sipahigil, J. M. Binder, M. W. Doherty, M. Metsch, L. J. Rogers, N. B. Manson, M. D. Lukin, and F. Jelezko, "Electron–phonon processes of the silicon-vacancy centre in diamond," *New J. Phys.*, vol. 17, no. 4, p. 043011, 2015.

[20] L. Blanco and F. G. de Abajo, "Spontaneous light emission in complex nanostructures," *Phys. Rev. B*, vol. 69, no. 20, p. 205414, 2004.

[21] T. H. Taminiau, F. Stefani, and N. F. van Hulst, "Single emitters coupled to plasmonic nano-antennas: angular emission and collection efficiency," *New J. Phys.*, vol. 10, no. 10, p. 105005, 2008.

[22] A. Wolcott, T. Schiros, M. E. Trusheim, E. H. Chen, D. Nordlund, R. E. Diaz, O. Gaathon, D. Englund, and J. S. Owen, "Surface structure of aerobically oxidized diamond nanocrystals," *J. Phys. Chem. C*, vol. 118, no. 46, pp. 26695–26702, 2014.

[23] A. Mohtashami and A. F. Koenderink, "Suitability of nanodiamond nitrogen–vacancy centers for spontaneous emission control experiments," *New J. Phys.*, vol. 15, no. 4, p. 043017, 2013.

[24] P. R. Dolan, X. Li, J. Storteboom, and M. Gu, "Complete determination of the orientation of nv centers with radially polarized beams," *Opt. Express*, vol. 22, no. 4, pp. 4379–4387, 2014.

[25] R. Epstein, F. Mendoza, Y. Kato, and D. Awschalom, "Anisotropic interactions of a single spin and dark-spin spectroscopy in diamond," *Nature Phys.*, vol. 1, no. 2, pp. 94–98, 2005.

[26] J. Zhang, Y. Li, X. Zhang, and B. Yang, "Colloidal self-assembly meets nanofabrication: From two-dimensional colloidal crystals to nanostructure arrays," *Adv. Mater.*, vol. 22, no. 38, pp. 4249–4269, 2010.

[27] R. Jin, Y. Cao, C. A. Mirkin, K. Kelly, G. C. Schatz, and J. Zheng, "Photoinduced conversion of silver nanospheres to nanoprisms," *Science*, vol. 294, no. 5548, pp. 1901–1903, 2001.

[28] A. G. Curto, G. Volpe, T. H. Taminiau, M. P. Kreuzer, R. Quidant, and N. F. van Hulst, "Unidirectional emission of a quantum dot coupled to a nanoantenna," *Science*, vol. 329, no. 5994, pp. 930–933, 2010.

[29] X. Meng, R. R. Grote, A. Wolcott, J. S. Owen, and R. M. Osgood, "Photoluminescence enhancement from a single nitrogen vacancy center in a nanodiamond crystal via a metal nanoantenna," in *Laser Science*, pp. LTh3H–1, Optical Society of America, 2013.

[30] D. Scarabelli, M. Trusheim, O. Gaathon, D. Englund, and S. J. Wind, "Nanoscale engineering of closely-spaced electronic spins in diamond," *Nano Lett.*, vol. 16, no. 8, pp. 4982–4990, 2016.

[31] D. Dregely, K. Lindfors, J. Dorfmüller, M. Hentschel, M. Becker, J. Wrachtrup, M. Lippitz, R. Vogelgesang, and H. Giessen, "Plasmonic antennas, positioning, and coupling of individual quantum systems," *Phys. Status Solidi B*, vol. 249, no. 4, pp. 666–677, 2012.

[32] A. W. Schell, G. Kewes, T. Schröder, J. Wolters, T. Aichele, and O. Benson, "A scanning probe-based pick-and-place procedure for assembly of integrated quantum optical hybrid devices," *Rev. Sci. Instrum.*, vol. 82, no. 7, p. 073709, 2011.

[33] E. Hao and G. C. Schatz, "Electromagnetic fields around silver nanoparticles and dimers," *J. Chem. Phys.*, vol. 120, no. 1, pp. 357–366, 2004.

[34] P. Nordlander, C. Oubre, E. Prodan, K. Li, and M. Stockman, "Plasmon hybridization in nanoparticle dimers," *Nano Lett.*, vol. 4, no. 5, pp. 899–903, 2004.

[35] J.-Q. Xi, M. F. Schubert, J. K. Kim, E. F. Schubert, M. Chen, S.-Y. Lin, W. Liu, and J. A. Smart, "Optical thin-film materials with low refractive index for broadband elimination of fresnel reflection," *Nat. Photon.*, vol. 1, no. 3, pp. 176–179, 2007.

[36] X. Meng, R. R. Grote, J. I. Dadap, N. C. Panoiu, and R. M. Osgood, "Engineering metal-nanoantennae/dye complexes for maximum fluorescence enhancement," *Opt. Express*, vol. 22, no. 18, pp. 22018–22030, 2014.

[37] T. K. Sau and C. J. Murphy, "Seeded high yield synthesis of short au nanorods in aqueous solution," *Langmuir*, vol. 20, no. 15, pp. 6414–6420, 2004.

[38] S. Kim, H. Jung, Y. Kim, J. Jang, and J. W. Hahn, "Resolution limit in plasmonic lithography for practical applications beyond 2x-nm half pitch," *Adv. Mater.*, vol. 24, no. 44, 2012.

[39] V. Giannini, A. I. Fernández-Domínguez, Y. Sonnefraud, T. Roschuk, R. Fernández-García, and S. A. Maier, "Controlling light localization and light–matter interactions with nanoplasmonics," *Small*, vol. 6, no. 22, pp. 2498–2507, 2010.

[40] P. Z. El-Khoury, E. Khon, Y. Gong, A. G. Joly, P. Abellan, J. E. Evans, N. D. Browning, D. Hu, M. Zamkov, and W. P. Hess, "Electric field enhancement in a self-assembled 2d array of silver nanospheres," *J. Chem. Phys.*, vol. 141, no. 21, p. 214308, 2014.

[41] Y. Gong, A. G. Joly, L. Kong, P. Z. El-Khoury, and W. P. Hess, "High-brightness plasmon-enhanced nanostructured gold photoemitter," *Phys. Rev. Appl.*, vol. 2, no. 6, p. 064012, 2014.

[42] G. X. Du, T. Mori, M. Suzuki, S. Saito, H. Fukuda, and M. Takahashi, "Evidence of localized surface plasmon enhanced magneto-optical effect in nanodisk array," *Appl. Phys. Lett.*, vol. 96, no. 8, p. 081915, 2010.

[43] B. Zhang, Y. Zhao, Q. Hao, B. Kiraly, I.-C. Khoo, S. Chen, and T. J. Huang, "Polarization-independent dual-band infrared perfect absorber based on

a metal-dielectric-metal elliptical nanodisk array," *Opt. Express*, vol. 19, no. 16, pp. 15221–15228, 2011.

[44] M. Rang, A. C. Jones, F. Zhou, Z.-Y. Li, B. J. Wiley, Y. Xia, and M. B. Raschke, "Optical near-field mapping of plasmonic nanoprisms," *Nano Lett.*, vol. 8, no. 10, pp. 3357–3363, 2008.

[45] A. Kinkhabwala, Z. Yu, S. Fan, Y. Avlasevich, K. Müllen, and W. Moerner, "Large single-molecule fluorescence enhancements produced by a bowtie nanoantenna," *Nat. Photon.*, vol. 3, no. 11, pp. 654–657, 2009.

Chapter 5

Two-Color Field Enhancement at an STM Junction for Spatiotemporally-Resolved Photoemission

Abstract

We report measurements and numerical simulations of ultrafast laser-excited carrier flow across a scanning tunneling microscope (STM) junction. The spatiotemporally-resolved current from a nanoscopic tungsten tip across a ∼1-nm vacuum gap to a silver surface is driven by a two-color excitation scheme that uses an optical delay-modulation technique to extract the two-color signal from background contributions. The role of optical field enhancements at the junction in driving the current is investigated using density functional theory (DFT) and full 3D finite-difference time-domain (FDTD) computations. We find that simulated field-enhanced two-photon photoemission (2PPE) currents are in excellent agreement with the observed exponential decay of the two-color photoexcited current with increasing tip-surface separation, as well as the optical-delay dependence of the current. The results suggest an approach to 2PPE with simultaneous subpicosecond temporal and nanometer spatial resolution.

5.1 Introduction

Strong near-field enhancements at metallic tip nanostructures are of central importance to emerging nanoscopic spectroscopies that use phenomena such as tip-enhanced Raman scattering [1, 2], near-field optical detection [3, 4], strong-field photoemission [5–7], nonlinear photoemission [8] and hot-electron transfer [9], to probe the structure and dynamics of surfaces and surface-adsorbed molecules at the nanoscale. Analysis of the photon-driven processes that may occur in the tip-surface junctions in these nanoprobes requires accurate determination of the field enhancements in the vicinity of the junction. Such determinations are challenging because the relevant length and time scales are in the subnanometer and subpicosecond regimes [10, 11].

We report the observation of electron currents driven across the tunnel junction of a cryogenic ultrahigh vacuum scanning tunneling microscope (STM), in conjunction with advanced computational simulations to elucidate the photoexcitation mechanism. In the experiment, the photocurrents are driven by ultrafast-laser two-color shaken-pulse pair excitation (hereafter referred to as 2C-SPPX [12]) of a metallic tip held $\sim$ 1 to 3 nm above a metallic substrate. We observe 2C-SPPX signals with subpicosecond time resolution that depend exponentially on the tip-sample separation and are sensitive to the position of the tip relative to Ag nanoparticles on otherwise flat Ag(111) terraces. Computationally, application of a three-dimensional finite difference time domain (3D-FDTD) method reveals that the photocurrents are well-described by 2PPE from the tip driven by a tip-substrate plasmon resonance [13, 14]. Based on the experiments and computations, we estimate tip-geometry-dependent resolutions less than a nanometer along the surface normal direction and smaller than the radius of curvature of the probe tip in the surface plane. The temporal resolution is limited by the $\sim$100-fs pulse widths of the exciting laser pulses.

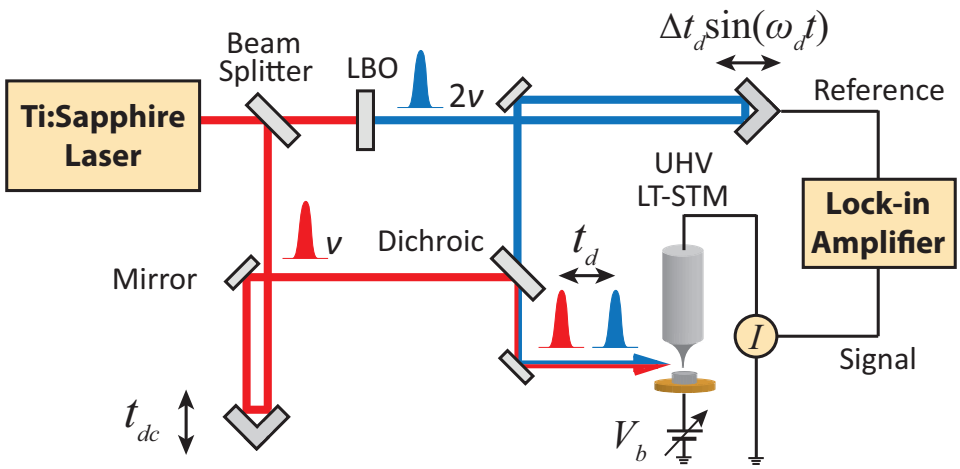

Figure 5.1: Schematic of the two-color ultrafast-laser-excited STM setup. The NIR output of a Ti:Sapphire oscillator (ν) is split by a beam sampler at the entrance to a modified Mach-Zehnder interferometer. The UV second harmonic (2ν) is generated in an LBO crystal. The two colors are combined on a dichroic mirror with time delay t_d and focused onto the tip-surface junction. The current (I) across the junction is monitored simultaneously by the STM control electronics and a lock-in amplifier.

5.2 Experimental Setup

Our two-color ultrafast-laser-assisted STM setup (Fig. 5.1) has been described in detail elsewhere [12] and is reviewed in brief here. The STM tunnel junction consists of an electrochemically-etched W tip and a Ag(111) surface held at 77 K. Two p-polarized beams excite the junction: the fundamental near-infrared (NIR) output of an ultrafast, 80-MHz repetition rate Ti:Sapphire oscillator ($\hbar\omega_1$=1.63 eV) and its ultraviolet (UV) second harmonic ($\hbar\omega_2$=3.26 eV). The photon energies are well below the photoemission threshold for both W (Φ=$\sim$4.6 eV) and Ag(111) (Φ=4.74 eV), thus space-charge effects due single-photon photoemission do not play a role. Two 2PPE pathways are possible: absorption of either two UV photons, or of one UV and one NIR photon, is sufficient to excite electrons above the vacuum level. Higher-order process are possible, but these two-photon process predominate [12]. As described in our prior work [12], this two-color scheme eliminates optical interference, delivering a constant thermal load to the junction even for pulse delays within the cross-correlation envelope. This eliminates the $\sim$1ps "blind spot" caused by strong thermal expansion and contraction driven by interference in one-color schemes where interference modulates the thermal load [12, 15].

To time-resolve the photoemission it is necessary to (i) isolate the two-color 2PPE signal from the one-color signal and the conventional, bias-driven STM tunneling current, and (ii) measure the two-color signal as a function of delay between the NIR and UV pulses. This is achieved by the 2C-SPPX method [12]. The two colors traverse separate arms of an interferometer. The NIR arm defines a central delay time, t_{dc}, about which the NIR-UV delay, $t_d(t)$, can be dithered with a sinusoidal modulation at frequency $f_d = \omega_d/2\pi$ such that $t_d(t) = t_{dc} + \Delta t_d \sin(\omega_d t)$, where t is the laboratory-frame time and Δt_d is the dither amplitude. The dither results in a sinusoidal modulation of any photoinduced contribution that depends on the delay between the two pulses; delay-independent contributions are unmodulated. Thus the

delay-dependent signal can be isolated using phase-sensitive detection of the sample-tip current by lock-in amplification.

5.3 FDTD Simulations

For the 3D-FDTD field enhancement computations, the tip was modeled as an 800-nm-long truncated cone terminated by a hemispherical apex. Based on SEM images of the probe used in the experiments, the radius of the hemisphere, R, was set to 55 nm and the base of the cone was set equal to 200 nm. The probe, aligned along the z-axis, was suspended perpendicularly above the Ag surface, designated as the x-y plane, with a variable distance, d, between its apex and the surface. To match the experimental conditions, the laser pulses were collinearly incident with Gaussian temporal profiles of 100 and 167 fs full-width at half maximum (FWHM), respectively, at an angle of $\theta = 78^\circ$ with respect to the z-axis.

A full 3D-FDTD numerical computation was employed with a finite difference resolution of 1 nm over the large region of the tip away from the junction, but a much finer resolution—down to 0.1 nm—in the gap between the tip and substrate. A non-uniform grid setup avoided abrupt and sharp terminations of the model's structure. The extensive computational requirements of a full 3D-FDTD simulation (Synopsys RSoft) were satisfied using a parallel implementation on a Linux cluster at the Center for Functional Nanomaterials at Brookhaven National Laboratory.

A typical plasmonic mode for two-color excitation with the tip apex located 2 nm above the Ag is shown in Fig. 5.2a, where we plot the 3D-FDTD-computed field intensity in the x-z plane averaged over one oscillation of optical excitation. The electric field is enhanced significantly around the tip end, and the maximum enhancement at the apex approaches four orders of magnitude. The field intensity is plotted in terms of the calculated enhancement factor $|\vec{E}(\omega_1) + \vec{E}(\omega_2)|^2/(|\vec{E}_i(\omega_1)|^2 + |\vec{E}_i(\omega_2)|^2)$,

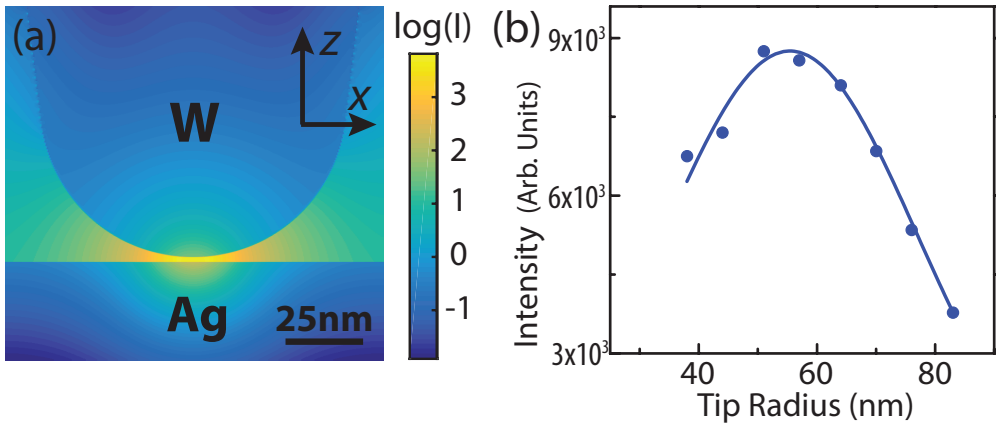

Figure 5.2: (a) The normalized, time averaged electric field intensity spatial distribution in response to two-color excitation for a 55-nm radius tungsten tip, and (b) the plasmonic mode intensity at the midpoint between the tip apex and the substrate as a function of tip radius. The tip apex-substrate spacing is 2 nm in both (a) and (b).

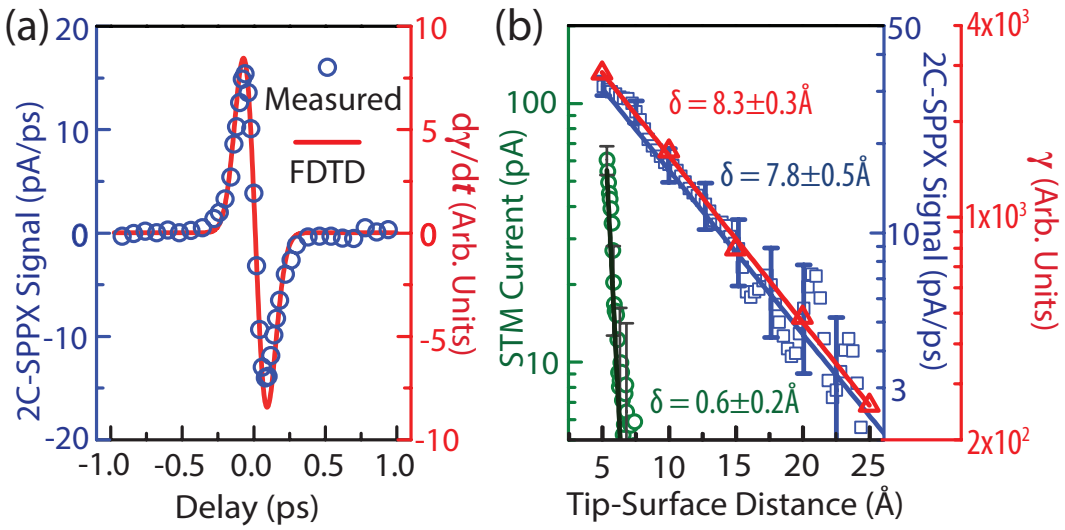

Figure 5.3: (a) Time resolved 2C-SPPX photoemission signal (open circles). Solid line: delay-time derivative of the 3D-FDTD-simulated 2C-SPPX signal ($\mathrm{d}\gamma/\mathrm{d}t$, $\gamma \sim |\vec{E}(\omega_1)|^2|\vec{E}(\omega_2)|^2$). (b) Measured STM current and 2C-SPPX signal vs. tip-surface distance (open circles and squares, respectively) and the amplitude of the delay-time derivative of the simulated 2C-2PPX signal vs. tip-sample distance (open triangles). The corresponding solid lines are single-exponential-decay fits to the data.

where $\vec{E}(\omega_j)$ and $\vec{E}_i(\omega_j)$ are the calculated and incident electric field amplitudes, respectively, at frequency ω_j. We find that the field enhancement is critically sensitive to the geometry of the W probe, as expected [14]. Specifically, our calculations reveal a tip-substrate hybridized mode due to interaction of the nonresonant W tip with the plasmonic Ag substrate that significantly impacts the magnitude of the field-enhancement. This result is illustrated in Fig. 5.2(b), where the field enhancement is shown to depend strongly on the tip radius. We identify a resonance centered at $\sim$55 nm, which shifts slightly with tip-substrate separation. This result indicates that maximizing the field at the tip would require precise control of the tip geometry [16].

5.4 Results and Analysis

Three key aspects of the experimental 2C-SPPX measurements are illustrated in Figs. 5.3 and 5.4: (i) a subpicosecond response, (ii) an exponential decay with tip-surface distance on a subnanometer length scale, and (iii) a sensitivity to the tip position relative to nanometer-scale surface features. In the following, each of these aspects of the experimental results is described. We then consider the computations and their implications regarding the mechanism of the observed effects.

Figure 5.3a shows the subpicosecond time-resolved 2C-SPPX signal as a function of the NIR-UV delay. These measurements were made with the tip engaged in tunneling (tip-sample separation of $\sim$0.5 nm) at a +0.6 V sample bias (current setpoint = 51 pA; feedback bandwidth = 0.5 Hz; data averaged over 100 delay sweeps). The derivative lineshape is well-fit by the first derivative of a $\sim$200-fs FWHM Gaussian, as found previously [12], and consistent with the cross correlation of the two Gaussian-shaped photoexcitation pulses. The timescale is consistent with a prompt two-photon photoemission process, and the amplitude of the Gaussian is positive, indicating that the direction of the current flow is from the tip to the sample.

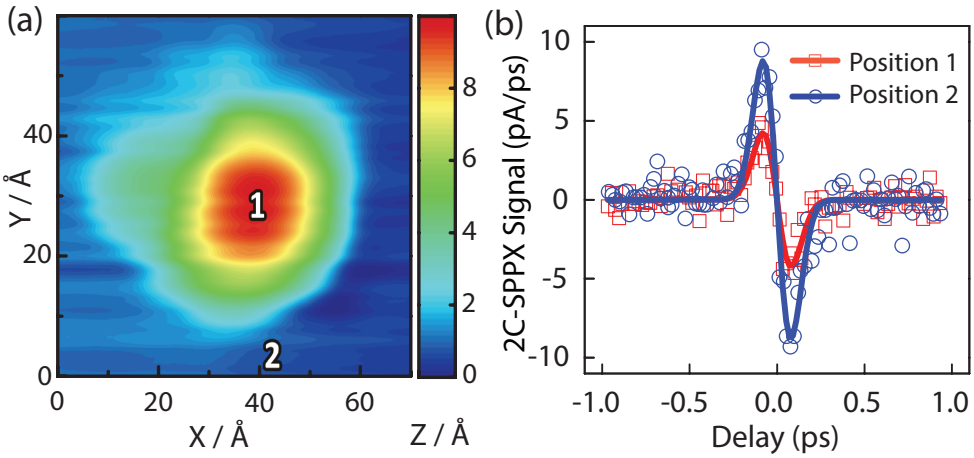

Figure 5.4: (a) Constant-current STM image of a sliver nanoparticle atop a Ag(111) surface. The color bar shows the vertical height of the sample surface (x-y plane). (b) Demonstration of position dependence of the 2C-SPPX signal amplitude: atop (position 1) and adjacent to (position 2) the nanoparticle, with the tip height determined by the same constant current conditions (bias = +0.6V, current = 50 pA). The solid lines are Gaussian-first-derivative fits to the data.

Figure 5.3b shows 2C-SPPX measurements made with the NIR-UV delay fixed at -70 fs (i.e., at the maximum of the 2C-SPPX signal in Fig. 5.3a) while retracting the tip from the tunneling setpoint (+0.6 V, 50 pA) with the feedback control disabled. The data are well fit by a single exponential decay: $I = I_0 \exp(-z/\delta)$, where z is the tip-sample distance, $z = 0$ corresponds to the distance at which the set point current ($I_0 = 50$ pA) is achieved, and the decay length, $\delta = 7.8 \pm 0.5$Å. Also shown for reference in Fig. 5.3b is the measured the z-dependence of the conventional tunneling current (i.e., the unilluminated junction). This, as expected, is also an exponential decay with a decay length of $\delta = 0.6 \pm 0.2$Å—typical for an STM junction [17]. The large disparity between the two decay lengths indicates that photoexcited tunneling can be ruled out as a possible mechanism for the 2C-SPPX current.

Figure 5.4 shows the sensitivity of the 2C-SPPX signal to the tip position near a nanometer-scale surface feature. In particular, measurements were made atop and adjacent to a 3-nm diameter, 1-nm high hemispherical nanoparticle on the otherwise flat Ag(111) surface. The topography of this feature is shown in Fig. 5.4a. Figure 5.4b indicates a factor of $\sim$2 decrease in 2C-SPPX signal atop the particle as compared to adjacent to the particle. As discussed below, this attenuation is only partially explained by the exponential z dependence, suggesting that lateral resolution on nanometer length scales is also achieved.

To understand the mechanism responsible for these key experimental observations, we first weigh the relative significance of contributions from two regimes for electron transport across the gap: (i) where classical electrodynamics is a good description of the optical response in the junction and (ii) where quantum tunneling modifies the optical response. To delineate these regimes, we performed DFT calculations using the ABINIT code [18], to obtain the self-consistent electron potential profile, V_{eff}, across the vacuum gap, with particular attention to the height of V_{eff} above the Fermi level (E_{F}), i.e., the potential barrier height. We used the local density approxima-

tion because it more accurately reproduces the experimental work function values for Ag and W than does the generalized gradient approximation. The W(111)/Ag(111) junction interface was represented by $(\sqrt{3} \times \sqrt{3})R30^\circ$ W(111) (bcc, bulk lattice parameter = 3.165 Å) supercell matched to a $(\sqrt{7} \times \sqrt{7})R19^\circ$ Ag(111) (fcc, bulk lattice parameter = 4.085 Å) supercell. The hexagonal supercell's lateral lattice parameter was 7.71 Å, corresponding to a slight linear compression of the W (0.56%) and expansion of the Ag (0.88%). The cell consisted of 7 slabs of W and 4 slabs of Ag separated by a vacuum layer of variable thickness. The Brillouin zone was sampled with a $(6 \times 6 \times 6)$ Monkhorst-Pack k-point mesh. The structure was optimized prior to the V_{eff} calculation.

The calculations show (Fig. 5.5, left) that for vacuum-gap widths below ∼4 Å the barrier height decreases rapidly with decreasing gap width from a value nearly equal to the work function toward zero when the W and Ag contact. In contrast, for gap widths above ∼4 Å (Fig. 5.5, middle and right), the tip-substrate junction is characterized by a substantial potential barrier with a constant height equal to the height of the vacuum level above E_F.

These results have qualitative significance regarding the suitability of the application of classical electrodynamics. Specifically, for vacuum-gap widths in the regime where the potential barrier height is small, quantum tunneling probabilities are high and electrons can flow freely back and forth across the junction. This represents a significant modification of the junction optical response that drastically reduces electromagnetic field enhancements relative to classical predictions [19]. Our DFT results suggest that for the Ag-W system, quantum tunneling cannot be ignored below ∼4 Å.

On the other hand, for gap widths ≥4 Å, the barrier is sufficiently high and the electron tunneling probability is greatly reduced. In this regime the tip-surface plasmonic coupling is well described by classical electrodynamics. The experimentally-observed exponential decay of the conventional tunneling current (Fig. 5.3b) confirms

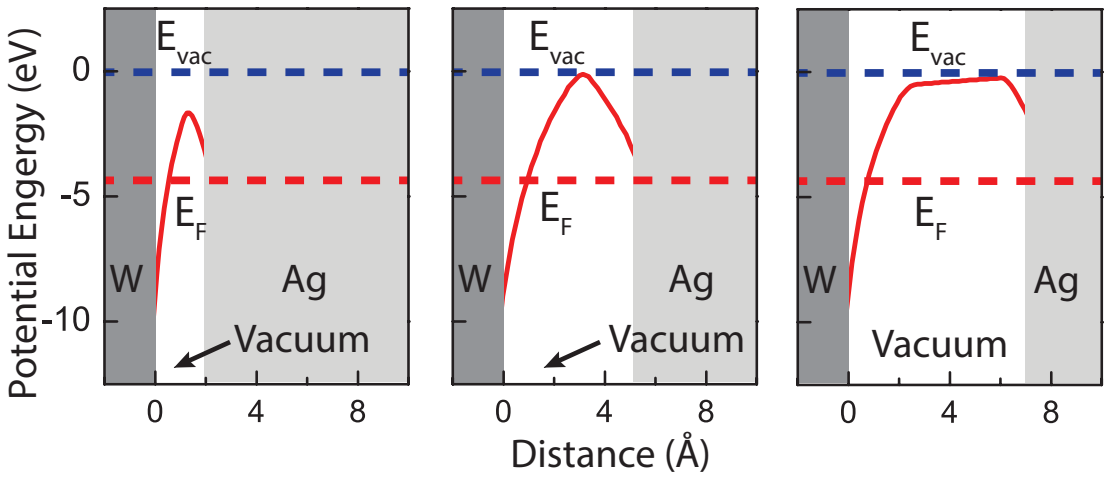

Figure 5.5: Self-consistent effective potential energy V_{eff} along the tip axis, for $d = 2.0\,\text{Å}$ (left), $4.0\,\text{Å}$ (middle) and $7.0\,\text{Å}$ (right), where d is the vacuum distance between the W tip and Ag substrate. The red dashed lines mark the Fermi level. The blue dashed lines mark the vacuum energy.

that the measurements were made in the regime where the barrier height is constant with increasing gap width [20]. Furthermore, the relatively long decay length for the 2C-SPPX signal (Fig. 5.3b) indicates that a photoassisted quantum tunneling mechanism is not operative. Thus the 3D-FDTD calculations using classical electromagnetic theory in the regime where our measurements were made, namely tip-sample gaps greater than $\sim$4 Å, is appropriate. The calculations yield the tip-sample photoinduced current, assuming that 2PPE dominates the observed signal. The good agreement of the simulations shown below with experimental data supports this assumption and our assignment of the operative mechanism as 2PPE.

From Fermi's Golden Rule, the carrier transition rate for two-photon two-color photoexcitation from the ground state to the final state (vacuum), which is proportional to the two-color 2PPE yield, can be shown to be proportional to the product of the field intensities: $\Gamma_{i\to f} \propto \gamma$, where $\gamma = |\vec{E}(\omega_1)|^2|/|\vec{E}_i(\omega_1)|^2 \times |\vec{E}(\omega_2)|^2/|\vec{E}_i(\omega_2)|^2$ [21]. Thus, we calculated the relative photoemission yield from the tip as a function of the tip-sample gap width at a fixed NIR-UV pulse delay of -70 fs (i.e., near the peak in the observed 2C-SPPX signal, Fig. 5.3a). The computational result is shown in Fig. 5.3b. In the regime where experimental measurements were possible, the computed field intensity product, γ, exhibits an exponential decay with a decay length of $\delta = 8.3 \pm 0.3$Å, in excellent agreement with that of the measured 2C-SPPX photoinduced current, $\delta = 7.8 \pm 0.5$Å. This agreement supports the conclusion that the field enhancement at the tip apex in proximity to the surface is responsible for the observed 2C-SPPX signal. We have also used the 3D-FDTD computation of the field enhancement in the junction to simulate the pulse-delay dependence of the photoelectron yield. The calculated time derivative of γ depends on the pulse-delay in a manner nearly identical to that of the 2C-SPPX signal (Fig. 5.3a). This observation indicates that the photoinduced process, involving a virtual intermediate state, is immediate. Thus the simulation result is consistent with our conclusion that the

field enhancement at the tip apex in proximity to the surface drives the 2PPE that is responsible for the observed 2C-SPPX signal.

Finally, we address the issue of lateral resolution. The sensitivity of the 2C-SPPX signal to position with respect to a ∼2 nm feature in Fig. 5.4a suggests that a resolution of ∼2 nm may be achieved. Note that, in the absence of the nanoparticle, raising the tip ∼1 nm from the surface results in a ∼3.4-fold attenuation of the 2C-SPPX signal, based on both the decay lengths extracted from the experiments and computations. However, raising the tip ∼1 nm above surface with the nanoparticle below the tip apex was observed to result in only a ∼2.1-fold attenuation (Fig. 5.4b). This discrepancy suggests that the tip is sensitive to the presence of the particle, with a lateral resolution on the order of 1-2 nm. However, further experimental and computational investigations are needed to quantify the limits on lateral resolution.

5.5 Summary

In summary, we have demonstrated two-color two-photon photoemission from a nanoscopic probe tip to a solid surface with time resolution limited by the ∼100 fs widths of the exciting laser pulses. The photoemission is strongly sensitive to the height of the tip above the surface, decaying exponentially with a subnanometer decay length. 3D-FDTD computations of the optical field enhancement in the junction support our assignment of photoemission as the mechanism responsible for the observed signal. In addition, measurements in the neighborhood of a ∼3 nm metal particle suggest that resolution of features on nanometer scale is possible. Such detailed investigations of plasmonic field enhancements and current flow in a tip-surface tunneling junction are critical to the development of emerging fs-Å joint-resolution and single-molecule spectroscopy methods [22]. With improved control over tip size and shape, the field-enhancement-based time-resolved excitations at the STM tip

apex and at metal nanoparticle surfaces may enable the mapping of electron dynamics at the nanoscale via photoemission. Also, excitation with longer wavelengths to drive higher-order optical nonlinearities could improve spatial resolution [8]. Our work reported here is an important step toward developing 2PPE to achieve simultaneous subnanometer and subpicosecond spatiotemporal resolution of surface electron dynamics.

5.6 References

[1] T. Ichimura, N. Hayazawa, M. Hashimoto, Y. Inouye, and S. Kawata, "Tip-enhanced coherent anti-stokes raman scattering for vibrational nanoimaging," *Phys. Rev. Lett.*, vol. 92, no. 22, p. 220801, 2004.

[2] J. Stadler, T. Schmid, and R. Zenobi, "Nanoscale chemical imaging using top-illumination tip-enhanced raman spectroscopy," *Nano Lett.*, vol. 10, no. 11, pp. 4514–4520, 2010.

[3] E. J. Sánchez, L. Novotny, and X. S. Xie, "Near-field fluorescence microscopy based on two-photon excitation with metal tips," *Phys. Rev. Lett.*, vol. 82, no. 20, p. 4014, 1999.

[4] Z. Fei, A. Rodin, G. Andreev, W. Bao, A. McLeod, M. Wagner, L. Zhang, Z. Zhao, M. Thiemens, G. Dominguez, *et al.*, "Gate-tuning of graphene plasmons revealed by infrared nano-imaging," *Nature (London)*, vol. 487, no. 7405, pp. 82–85, 2012.

[5] R. Bormann, M. Gulde, A. Weismann, S. Yalunin, and C. Ropers, "Tip-enhanced strong-field photoemission," *Phys. Rev. Lett.*, vol. 105, no. 14, p. 147601, 2010.

[6] M. Schenk, M. Krüger, and P. Hommelhoff, "Strong-field above-threshold photoemission from sharp metal tips," *Phys. Rev. Lett.*, vol. 105, no. 25, p. 257601, 2010.

[7] M. Krüger, M. Schenk, and P. Hommelhoff, "Attosecond control of electrons emitted from a nanoscale metal tip," *Nature (London)*, vol. 475, no. 7354, pp. 78–81, 2011.

[8] C. Ropers, D. Solli, C. Schulz, C. Lienau, and T. Elsaesser, "Localized multiphoton emission of femtosecond electron pulses from metal nanotips," *Phys. Rev. Lett.*, vol. 98, no. 4, p. 043907, 2007.

[9] S. Wu and W. Ho, "Two-photon-induced hot-electron transfer to a single molecule in a scanning tunneling microscope," *Phys. Rev. B*, vol. 82, no. 8, p. 085444, 2010.

[10] S. Dey, D. Mirell, A. R. Perez, J. Lee, and V. A. Apkarian, "Nonlinear femtosecond laser induced scanning tunneling microscopy," *J. Chem. Phys.*, vol. 138, no. 15, p. 154202, 2013.

[11] T. L. Cocker, V. Jelic, M. Gupta, S. J. Molesky, J. A. Burgess, G. De Los Reyes, L. V. Titova, Y. Y. Tsui, M. R. Freeman, and F. A. Hegmann, "An ultrafast terahertz scanning tunnelling microscope," *Nat. Photon.*, vol. 7, no. 8, pp. 620–625, 2013.

[12] A. Dolocan, D. Acharya, P. Zahl, P. Sutter, and N. Camillone III, "Two-color ultrafast photoexcited scanning tunneling microscopy," *J. Phys. Chem. C*, vol. 115, no. 20, pp. 10033–10043, 2011.

[13] R. M. Roth, N. C. Panoiu, M. M. Adams, R. M. Osgood, C. C. Neacsu, and M. B. Raschke, "Resonant-plasmon field enhancement from asymmetrically illuminated conical metallic-probe tips," *Opt. Express*, vol. 14, no. 7, pp. 2921–2931, 2006.

[14] N. Behr and M. B. Raschke, "Optical antenna properties of scanning probe tips: plasmonic light scattering, tip-sample coupling, and near-field enhancement," *J. Phys. Chem. C*, vol. 112, no. 10, pp. 3766–3773, 2008.

[15] V. Gerstner, A. Knoll, W. Pfeiffer, A. Thon, and G. Gerber, "Femtosecond laser assisted scanning tunneling microscopy," *J. Appl. Phys.*, vol. 88, no. 8, pp. 4851–4859, 2000.

[16] X. Meng, R. R. Grote, J. I. Dadap, N. C. Panoiu, and R. M. Osgood, "Engineering metal-nanoantennae/dye complexes for maximum fluorescence enhancement," *Opt. Express*, vol. 22, no. 18, pp. 22018–22030, 2014.

[17] Y. Kuk and P. Silverman, "Scanning tunneling microscope instrumentation," *Rev. Sci. Instrum.*, vol. 60, no. 2, pp. 165–180, 1989.

[18] X. Gonze, "A brief introduction to the ABINIT software package," *Z. Kristallogr.*, vol. 220, no. 5/6, pp. 558–562, 2005.

[19] J. Zuloaga, E. Prodan, and P. Nordlander, "Quantum description of the plasmon resonances of a nanoparticle dimer," *Nano Lett.*, vol. 9, no. 2, pp. 887–891, 2009.

[20] Y. Kuk and P. Silverman, "Scanning tunneling spectroscopy of metal surfaces," *J. Vac. Sci. Technol., A*, vol. 8, no. 1, pp. 289–292, 1990.

[21] H. Ueba and B. Gumhalter, "Theory of two-photon photoemission spectroscopy of surfaces," *Proc. Surf. Sci.*, vol. 82, no. 4, pp. 193–223, 2007.

[22] R. Zhang, Y. Zhang, Z. Dong, S. Jiang, C. Zhang, L. Chen, L. Zhang, Y. Liao, J. Aizpurua, Y. e. Luo, *et al.*, "Chemical mapping of a single molecule by plasmon-enhanced raman scattering," *Nature (London)*, vol. 498, no. 7452, pp. 82–86, 2013.

Chapter 6

Rigorous Theoretical Analysis of a Surface-Plasmon Nanolaser with Monolayer MoS_2 Gain Medium

Abstract

Lasers based on monolayer transition-metal dichalcogenide semiconductor crystals have the potential for low threshold operation and small device footprint; however, nanophotonic engineering is required to maximize interaction between optical fields and the three-atom-thick gain medium. Here, we develop a theoretical model to design a direct-bandgap, optically-pumped nanophotonic integrated laser. Our device utilizes a gap-surface-plasmon optical mode to achieve subwavelength optical confinement and consists of a high-index GaP nanowire atop a monolayer MoS_2 film on a Ag substrate. The optical field and materials medium are analyzed using a three dimensional finite-difference time-domain (3D-FDTD) method and a first-principles calculation based on density functional theory (DFT), respectively. The nanolaser is designed to have a threshold of $\sim$0.6 µW under quasi-continuous wave operation on an excitonic transition at room temperature.

6.1 Introduction

The realization of an ultracompact subwavelength on-chip laser continues to be an unmet challenge for microdevice applications. However, this goal has recently been advanced with devices based on the plasmonic properties of metals, which confine optical excitation to subwavelength dimensions *via* surface plasmon polaritons (SPPs) at metal-dielectric interfaces [1–4]. When coupled to a suitable optical gain medium, SPP lasers can achieve tight plasmonic (optical) confinement and feedback, which reduces the optical mode volume far below the scale of a vacuum wavelength. The ability to confine optical energy to such small volumes offers an ideal platform for coupling to the unique material properties of gain media with reduced dimensionality.

For these lasers, monolayers of transition-metal dichalcogenide (TMDC) semiconductors present a number of desirable electronic and optical properties for use as a gain medium, including relatively large direct bandgaps, robust excitons, and strong photoluminescence (PL). For example, a single layer of molybdenum disulfide (MoS_2) has a direct gap of 1.82 eV and a luminescence quantum efficiency of more than a factor 10^4 greater than the bulk crystal [5]. More importantly, it is stable at room temperature due to its large binding energy. The combination of these electrical, optical and chemical properties, not seen in monolayers of other materials, makes TMDCs promising candidates for novel optoelectronic devices, such as light-emitting devices operating in the visible range [6–9].

In this chapter, we report the design of an optically-pumped, plasmonically-excited TMDC laser using a rigorous theoretical analysis. The analysis is based on a fully three-dimensional finite element method (FEM) mode solver, finite-difference time-domain (3D-FDTD) computation for the time varying optical fields, and a first-principles calculation using density functional theory (DFT) for examining excitonic optical transition in the material medium [10].

6.2 Theoretical Model

The nanolaser topology analyzed here is illustrated in Fig. 6.1(a), with cross-section given in Fig. 6.1(b). The device uses a monolayer of MoS_2 for the active medium and a deep-subwavelength cavity. This cavity, which is approximately 1 µm long, provides resonances within the surface plasmon spectral bandwidth. This structure uses the 2D nature of the monolayer of the MoS_2, along with its overlaying and underlaying dielectric and plasmonic layers to obtain a low-threshold behavior. This hybrid geometry also includes a high-refractive-index nanowire (GaP, $n = 3.2$) placed on top of a low-refractive-index (SiO_2, $n = 1.45$) near the atomically smooth metal (Ag) film surface [2], where the metal surface serves as a plasmonic waveguide with a surface plasmon polaritons (SPPs) mode. A silver film is used since it offers the best properties among the available plasmonic films at visible and near-infrared wavelength range due to its minimal plasmonic damping. The laser design incorporates a slot in the SiO_2 layer so as to form region of suspended MoS_2 and hence reduced carrier lost; this reduced carrier recombination is known to lead, for example, to stronger photoluminescence [5]. We have chosen GaP for the lateral confining "over"wire because of its higher refractive index. This structure also offers low optical absorption and a higher group index, which further reduces the optical loss [11]. SPP scattering due to surface roughness [12] and grain boundaries [13] is ignored in our analysis, as we assume the silver film is an expitaxially grown, atomically smooth single-crystalline layer. The finite length of the nanowire defines the cavity that laterally confines cavity modes in the gap between the nanowire and the plasmonic waveguide, with cavity feedback arising from modal reflection at the end-facets. The MoS_2 has a finite thickness of 0.7 nm with a measured refractive index given in Ref. [14], and is supported between two SiO_2 spacer layers as illustrated in Fig. 6.1. The nanolaser has a length of 0.996 µm, which is carefully chosen by FDTD analysis as discussed in detail in a later section. Other monolayer TMDC materials have even higher quantum yield,

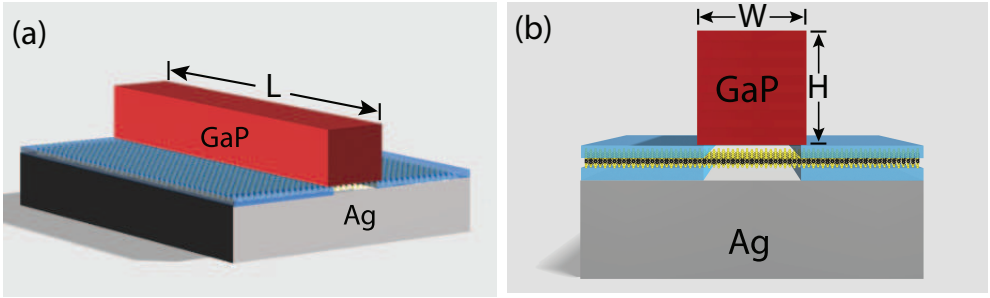

Figure 6.1: (a) A perspective view of the structure of the proposed nanolaser using a monolayer semiconductor film as the active medium. The high-refractive-index GaP nanowire with length L ∼1 µm is placed on a low-refractive-index dielectric near a metal surface. (b) A cross-sectional view of the device structure, showing the width (W) and height (H) of ∼0.2 µm for the nanowire and that the monolayer semiconductor film is embedded in a nm-thick low-permittivity, e.g. SiO_2, spacer layers.

such as WS_2 and WSe_2 [10], however, we use in our theoretical analysis a monolayer of MoS_2 since it is particularly well studied and thus, has a well characterized set of material parameters obtained via experimental measurements.

We can obtain a basic theoretical understanding of the time-resolved laser characteristics, using the following rate equation approach [15]:

$$\frac{dN}{dt} = R - \frac{N}{\tau_r} - \frac{N}{\tau_{nr}} - v_g g(N - N_{tr})P \tag{6.1}$$

$$\frac{dP}{dt} = \Gamma v_g g(N - N_{tr})P + \Gamma\beta\frac{N}{\tau_r} - \frac{P}{\tau_c} \tag{6.2}$$

where N and P are the carrier and photon densities within the nanocavity, R is the pumping rate, v_g is the group velocity, g is the differential gain coefficient and N_{tr} is the transparency carrier density. The cavity photon lifetime, the radiative, and the nonradiative recombination lifetimes are τ_c, τ_r and τ_{nr}, respectively. The spontaneous emission factor, β, is defined as the fraction of the spontaneous emission radiated into the cavity mode. The confinement factor, Γ, accounts for the matching between the active region and the optical mode. In the following analysis, FEM is used to find the modal group velocity and modal overlap with the gain medium, DFT is used to find the differential gain coefficient, and FDTD is used to find the cavity losses and spontaneous emission factor. With the totality of these parameters calculated through numerical methods, we can obtain a first-principle calculation of the lasing threshold for the proposed structure.

6.3 Hybrid Gap Mode

Our analysis begins using coupled-mode theory [16]. In this case, the cavity mode can be described as a superposition of the nanowire waveguide mode and the SPP mode, i.e. a hybrid mode,

$$\Psi = a\Psi_{wg} + b\Psi_{spp} \tag{6.3}$$

where a and b are the amplitudes of the constituent nanowire waveguide $\Psi_{wg} = \{1\ 0\}^T$ and SPP $\Psi_{spp} = \{0\ 1\}^T$ basis modes, respectively. The modes of the coupled system are characterized by the system of equations discussed in [17]

$$\begin{pmatrix} n_{wg} & \kappa_{12} \\ \kappa_{21} & n_{spp} \end{pmatrix} \begin{pmatrix} a \\ b \end{pmatrix} = n_{eff} \begin{pmatrix} a \\ b \end{pmatrix} \tag{6.4}$$

where κ_{12}, κ_{21} are the coupling strengths between specific nanowire waveguide and SPP modes and n_{wg}, n_{spp} are the refractive index of nanowire waveguide and the effective index of plasmonic waveguide, respectively. In addition, n_{eff} is the effective index of the resultant hybrid mode and its analytical solution agrees well with those calculated numerically.

A cross-section of the device, with an overlay of a plot of the hybrid mode, calculated by FEM, is shown in Fig. 6.2(a). The strong plasmonic confinement enables ultratight vertical localization of the hybrid optical mode in the gap, i.e., the cavity containing the suspended TMDC monolayer. Further as is seen in Fig. 6.2, the hybrid mode is also tightly confined in the transverse direction by the GaP nanowire; thus both effects result in excellent spatial overlap between the mode and the monolayer gain medium, enabling ultralow-threshold CW lasing operation in a diffraction-free footprint. The nanowire geometry was designed to maximize the field in the monolayer of MoS_2, so as also to maximize the absorption efficiency of monolayer MoS_2. The SiO_2 layers serve as low-permittivity spacers to suspend MoS_2, which leads to a strong normal electric field component in the gap due to the continuity of the displacement field across this interface. In addition, such a low-index dielectric-metal interface also leads to low propagation loss. The overlayer nanowire "guides"the hybrid gap mode, where its reflectivity depends only on the mismatch between the effective index of the structure and free space.

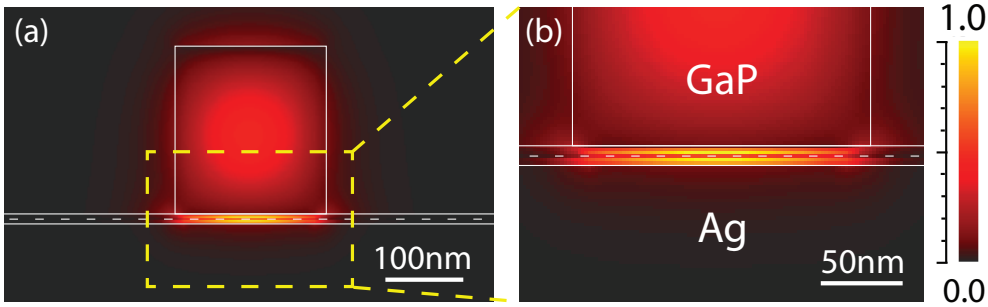

Figure 6.2: (a) A cross-sectional profile of the hybrid waveguide mode showing a high degree of confinement in the TMDC monolayer in the gap between the GaP nanowire and the Ag surface. (b) An enlarged-area of a portion of the panel (a) showing the gap mode and the MoS_2 monolayer (indicated by a dashed line).

6.4 Ab-initio Analysis

Due to the 2D nature of the MoS_2 (semiconductor) monolayer, the band structure of a suspended monolayer behaves as a quantum well, with an effective out-of-plane potential, which can be calculated using the density-functional-theory ABINIT code under the generalized gradient approximation [18]. In this calculation, a periodic slab geometry with a 12 Å vacuum spacer layer is used. In addition, the in-plane lattice constant and the interplane distance between the Mo and S atomic planes are structurally optimized. The calculation employs a $10 \times 10 \times 1$ k-point mesh with a wave function cut-off energy of 50 *Hartree* and an energy difference tolerance of 10^{-10}. Due to this quantum-well structure, monolayer TMDCs should offer some of the well known advantages of more conventional quantum well lasers, namely, the large differential gain associated with their 2D density of states. Moreover, compared to conventional group III-V quantum well lasers, the large refractive index of monolayer TMDCs can significantly increase the optical confinement in the laser active region of the laser. The optical gain can be further enhanced by the strong Colulomb interactions, due to the vertical confinement and the reduced dielectric screening [19].

These points are shown in a more detailed manner by the bandstructure of MoS_2. Figure 6.3(a) shows the calculated effective potential profile of monolayer MoS_2 along the out-of-plane direction (c axis). This potential profile indicates that in monolayer MoS_2, the pure in-plane nature of the electrons due to quantum confinement can be described by a single quantum-well model, which has a significant but finite barrier (8 eV) to electron transport in the out of plane direction. This barrier fully confines the gain of an optical wave within the quantum-well crystal medium. Figure 6.3(b) shows the uppermost valence band and the excitonic band along $\bar{\Gamma}$-$\bar{K}$-$\bar{M}$-$\bar{\Gamma}$ high-symmetry line. The figure shows a direct band gap of 1.82 eV at $\bar{K}$, which is very close to the experimental result given in [5]. Note the band degeneracy due to spin-orbit

is not considered here because the linearly polarized excitation wave will excite both spin-up and spin-down electrons. By fitting the valence band maximum (VBM) and excitonic band minimum (EBM) in the vicinity of $\bar{K}$ to a parabola, the hole effective mass can be extracted at the VBM ($m_v = 0.61m_e$) and the electron effective mass at the EBM ($m_c = 0.51m_e$), respectively. The carrier effective masses in our calculation are in good agreement with the values determined by G_0W_0 calculations [20]. It is worth noting that the relatively large effective masses of charge carriers in MoS_2 results in high densities of states in both the valence and conduction bands. This fact, coupled with the fairly large bandgap of MoS_2, requires carrier concentrations of $\sim 1 \times 10^{19}\,\mathrm{cm}^{-3}$ to push the quasi-Fermi levels into the corresponding bands so as to achieve population inversion. A recent experiment [21] has confirmed the presence of such high carrier concentrations.

The quantum-well behavior of the effective potential profile together with the carrier effective mass allow calculation of the gain, where its analytic form at excitation frequency ω_0 is [22]

$$\gamma(\omega_0) = \frac{m_r \lambda_0^2}{4\pi\hbar L_z n^2 \tau}[f_c(\hbar\omega_0) - f_v(\hbar\omega_0)] \tag{6.5}$$

where L_z is the thickness, τ is the recombination lifetime, n is the refractive index of monolayer active medium and where continuous wave operation is assumed. The gain coefficient also depends on the excitation wavelength λ_0, the reduced mass m_r, as well as the quasi-Fermi functions f_c and f_v that are evaluated at room temperature. Attainment of a low optical threshold is an important practical aspect of plasmonically enhanced lasers, such as the one studied here, since it governs the minimum power consumption, or threshold, necessary for useful device operation. In this chapter, the lasing threshold is defined by equating stimulated emission to spontaneous emission. Thus using a steady-state solution to the coupled rate equations (Eq. 6.1 and Eq. 6.2), a relationship between pumping rate R and photon densities P is obtained.

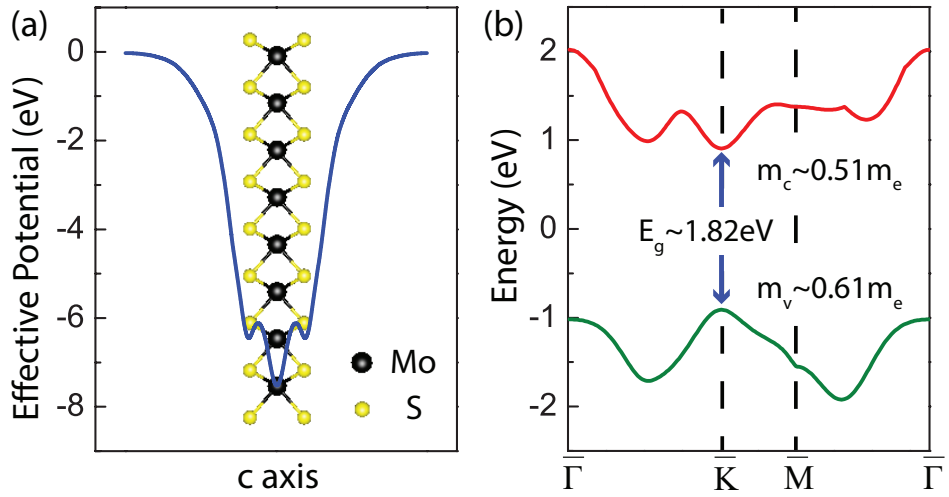

Figure 6.3: (a) The effective potential profile of the suspended monolayer MoS_2 that behaves like a quantum-well with a finite barrier of 8 eV. (b) The electron band structure of suspended monolayer MoS_2 with a bandgap of 1.82 eV. The electron effective mass has also been calculated by fitting the band in the vicinity of K point.

6.5 Device Design

Designing the cavity requires consideration of several different physical phenomena. For example, Fig. 6.4(a) shows the calculated confinement factor as a function of the gap thickness. The confinement factor, $\Gamma = \int_{gain} \epsilon_g E^2 \mathrm{d}v / \int_{cavity} \epsilon_c E^2 \mathrm{d}v$, is the overlap volume integral of the gain medium with the cavity mode, and E is the electric filed, ϵ_g and ϵ_c are the dielectric constants of the gain medium and cavity, respectively. The "error" bars in this figure are in fact ranges for confinement factor at each gap thickness generated by varying the nanowire geometry over different height and width combinations from 140 nm to 220 nm, respectively. The different combinations of dimensions can successfully support the fundamental mode with essentially very little energy leakage. The practical limitations in fabricating the laser structure also influence the actual design. For example, a perfect gap thickness of less than 5 nm is a challenge in fabrication, as a result, we have chosen to use a gap thickness of 7 nm. This dimension yields a satisfactory $\Gamma \approx 11\%$.

Second, plasmonic and radiative loss must be examined. Thus, the condition for laser oscillation at threshold is achieved when the sum of all losses, α, including physical processes, such as ohmic loss in the metal, emission of SPPs to the outside of the cavity, radiation leakage into the substrate, and far-field emission, is exactly balanced by the gain of the laser medium, γ. The loss factor can be expressed as $\alpha = \omega_r/(v_g Q)$ with ω_r as the optical frequency at cavity resonance and Q is the quality factor. Hence minimizing the cavity loss entails optimizing the quality factor. The quality factor, Q, is obtained by use of 3D-FDTD computation. For this calculation, we use a laser wavelength of $\lambda = 682$nm, which is the free-space emission wavelength of monolayer MoS_2. The results of the quality factor as a function of the nanowire length are shown as the inset in Fig. 6.4(a), where the factor peaks at the cavity length of 0.996 µm with a quality factor of $Q = 91.7$ and a cavity resonance at the free-space wavelength of 640 nm, a value comparable to that reported in [2]. Note

that a small variation in nanowire length will shift the quality factor downwards, thus yielding an increase in laser threshold. However using the literature values for dimensional tolerance on fabrication structures such as this, we believe that relatively high Q values can be obtained. Meanwhile, the extremely small mode volume and the correspondingly large Purcell enhancement, which scales as Q/V_m, compensates for the modest Q. In particular, the mode volume V_m in our design is found to be $\sim \lambda^3/380$ via numerical computation. This small mode volume results in the large Purcell factor, $F = (3/4\pi^2)(Q/V_m)(\lambda/n_{eff})^3$, with a value of 118.3 for this specific design. Lasing at a reduced threshold power is achieved by enhancing the spontaneous emission rate via the Purcell factor, thus leading to an enhanced stimulated emission rate.

The third phenomenon which needs to be considered, is the spontaneous emission factor β. Its generic equation is based on a "one photon per mode"picture [23] and is defined as

$$\beta(\vec{r},\omega) = \frac{\left\langle |\vec{\mu}\cdot\vec{E}_{cav}(\vec{r},\omega)|^2 \middle| |\vec{\mu}\cdot\vec{E}_{cav}(\vec{r},\omega)|^2 \right\rangle}{\sum_i \left\langle |\vec{\mu}\cdot\vec{E}_i(\vec{r},\omega)|^2 \middle| |\vec{\mu}\cdot\vec{E}_i(\vec{r},\omega)|^2 \right\rangle} \tag{6.6}$$

where $|\vec{E}_{cav}(\vec{r},\omega)|^2$ represents the vacuum-field density in the cavity mode at atomic position $\vec{r}$ with frequency ω and where the sum in the denominator runs over all modes with $\vec{\mu}\cdot\vec{E}_i$ as dipolar atom-field interaction Hamiltonian. The device is assumed to work at a constant temperature; thus the temperature dependence of β is ignored. By setting the loss of the laser structure, α, equal to the gain of lasing medium, γ, we calculate the population of optically generated electron-hole pairs ΔN required to reach laser threshold to be on the order of 10^{19}cm^{-3}, and therefore, this population inversion can be used to obtain the corresponding nonlinear light pump curve using the spontaneous emission factor $\beta = 0.376$. This curve, which is shown in Fig. 6.4(b), gives a lasing threshold of 0.62 µW at 300 K, which is a reasonable value compare to

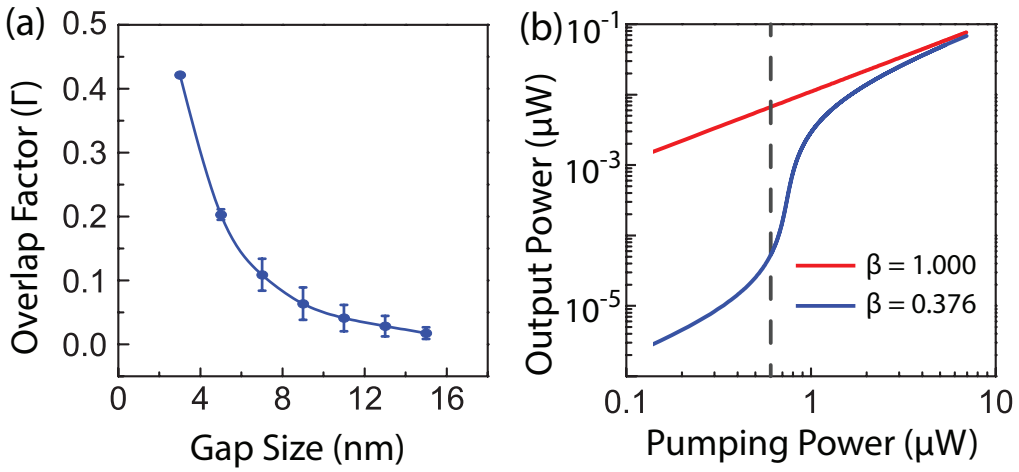

Figure 6.4: (a) Effect of different gap size on the overlap factor Γ. (b) Nonlinear pump curve versus pumping factor for different spontaneous emission factors $\beta = 0.376$ and 1 for the real structure and the ideal thresholdless case, respectively.

nanolaser reported in [7, 10, 21, 24].

Finally note that, in addition to the above approach to the nanolaser, there are several variations in the design that may further improve the device performance. For example, replacing the GaP nanowire with a GaP photonic crystal should lead to slow-light [25] enhancement of the circulating field and better confinement due to the larger group index of the photon crystal, thus further reducing the lasing threshold.

6.6 Summary

In summary, we have demonstrated a new nanolaser design using a 2D TMDC semiconductor as the active medium. We have also examined the lasing threshold requirements based on optically pumped surface-plasmon excitation. A surface mounted GaP nanowire is used to concentrate the light effectively into 2D active medium in order to reach a low lasing threshold. The resulting highly confined hybrid modes allow for subdiffraction-limited localization of electromagnetic-field-energy density at the gap between the metal substrate and a high-dielectric-constant nanowire. This field localization enables a low-threshold, compact integrated laser source.

6.7 References

[1] D. J. Bergman and M. I. Stockman, "Surface plasmon amplification by stimulated emission of radiation: Quantum generation of coherent surface plasmons in nanosystems," *Phys. Rev. Lett.*, vol. 90, p. 027402, Jan 2003.

[2] Y.-J. Lu, J. Kim, H.-Y. Chen, C. Wu, N. Dabidian, C. E. Sanders, C.-Y. Wang, M.-Y. Lu, B.-H. Li, X. Qiu, *et al.*, "Plasmonic nanolaser using epitaxially grown silver film," *Science*, vol. 337, no. 6093, pp. 450–453, 2012.

[3] R. F. Oulton, V. J. Sorger, T. Zentgraf, R.-M. Ma, C. Gladden, L. Dai, G. Bartal, and X. Zhang, "Plasmon lasers at deep subwavelength scale," *Nature (London)*, vol. 461, no. 7264, pp. 629–632, 2009.

[4] X. Meng, R. R. Grote, J. I. Dadap, N. C. Panoiu, and R. M. Osgood, "Engineering metal-nanoantennae/dye complexes for maximum fluorescence enhancement," *Opt. Express*, vol. 22, no. 18, pp. 22018–22030, 2014.

[5] K. F. Mak, C. Lee, J. Hone, J. Shan, and T. F. Heinz, "Atomically thin mos_2: A new direct-gap semiconductor," *Phys. Rev. Lett.*, vol. 105, p. 136805, Sep 2010.

[6] K. M. Goodfellow, R. Beams, C. Chakraborty, L. Novotny, and A. N. Vamivakas, "Integrated nanophotonics based on nanowire plasmons and atomically thin material," *Optica*, vol. 1, no. 3, pp. 149–152, 2014.

[7] S. Wu, S. Buckley, J. R. Schaibley, L. Feng, J. Yan, D. G. Mandrus, F. Hatami, W. Yao, J. Vučković, A. Majumdar, *et al.*, "Monolayer semiconductor nanocavity lasers with ultralow thresholds," *Nature (London)*, vol. 520, no. 7545, pp. 69–72, 2015.

[8] R. S. Sundaram, M. Engel, A. Lombardo, R. Krupke, A. C. Ferrari, P. Avouris, and M. Steiner, "Electroluminescence in single layer mos2," *Nano Lett.*, vol. 13, no. 4, pp. 1416–1421, 2013.

[9] X. Meng, R. Grote, J. Dadap, and R. Osgood, "Threshold analysis in monolayer semiconductor nanolaser by surface plasmon enhancement," in *Laser Science*, pp. LTh3I–3, Optical Society of America, 2015.

[10] Y. Ye, Z. J. Wong, X. Lu, X. Ni, H. Zhu, X. Chen, Y. Wang, and X. Zhang, "Monolayer excitonic laser," *Nat. Photon.*, vol. 9, pp. 733–737, Nov. 2015.

[11] M. Z. Alam, J. S. Aitchison, and M. Mojahedi, "A marriage of convenience: Hybridization of surface plasmon and dielectric waveguide modes," *Laser Photon. Rev.*, vol. 8, no. 3, pp. 394–408, 2014.

[12] L. Cao, N. Panoiu, R. D. Bhat, and R. Osgood Jr, "Surface second-harmonic generation from scattering of surface plasmon polaritons from radially symmetric nanostructures," *Phys. Rev. B*, vol. 79, no. 23, p. 235416, 2009.

[13] D. McLean and A. Maradudin, "Grain boundaries in metals," *Phys. Today*, vol. 11, no. 7, pp. 35–36, 2009.

[14] A. Castellanos-Gomez, N. Agrait, and G. Rubio-Bollinger, "Optical identification of atomically thin dichalcogenide crystals," *Appl. Phys. Lett.*, vol. 96, no. 21, p. 213116, 2010.

[15] L. A. Coldren, S. W. Corzine, and M. L. Mashanovitch, *Diode lasers and photonic integrated circuits*, vol. 218. John Wiley & Sons, 2012.

[16] H. A. Haus, *Waves and fields in optoelectronics*, vol. 464. Prentice-Hall Englewood Cliffs, NJ, 1984.

[17] R. F. Oulton, V. J. Sorger, D. Genov, D. Pile, and X. Zhang, "A hybrid plasmonic waveguide for subwavelength confinement and long-range propagation," *Nat. Photon.*, vol. 2, no. 8, pp. 496–500, 2008.

[18] X. Gonze, "A brief introduction to the abinit software package," *Z. Kristallogr.*, vol. 220, no. 5/6, pp. 558–562, 2005.

[19] J. Yao, G. P. Agrawal, and P. Gallion, "Linewidth enhancement factor and nonlinear gain in znse semiconductor lasers," *IEEE Photon. Technol. Lett.*, vol. 7, no. 2, pp. 149–151, 1995.

[20] A. Ramasubramaniam, "Large excitonic effects in monolayers of molybdenum and tungsten dichalcogenides," *Phys. Rev. B*, vol. 86, no. 11, p. 115409, 2012.

[21] O. Salehzadeh, M. Djavid, N. H. Tran, I. Shih, and Z. Mi, "Optically pumped two-dimensional mos2 lasers operating at room-temperature," *Nano Lett.*, vol. 15, no. 8, pp. 5302–5306, 2015.

[22] A. Yariv and P. Yeh, *Photonics: Optical Electronics in Modern Communications*. Oxford University Press, 2006.

[23] M. Van Exter, G. Nienhuis, and J. Woerdman, "Two simple expressions for the spontaneous emission factor β," *Phys. Rev. A*, vol. 54, no. 4, p. 3553, 1996.

[24] Y.-J. Lu, C.-Y. Wang, J. Kim, H.-Y. Chen, M.-Y. Lu, Y.-C. Chen, W.-H. Chang, L.-J. Chen, M. I. Stockman, C.-K. Shih, *et al.*, "All-color plasmonic nanolasers with ultralow thresholds: autotuning mechanism for single-mode lasing," *Nano Lett.*, vol. 14, no. 8, pp. 4381–4388, 2014.

[25] J. F. McMillan, X. Yang, N. C. Panoiu, R. M. Osgood, and C. W. Wong, "Enhanced stimulated raman scattering in slow-light photonic crystal waveguides," *Opt. Lett.*, vol. 31, no. 9, pp. 1235–1237, 2006.

Chapter 7

Other Nanophotonic Applications

7.1 Graphene Plasmonics

7.1.1 Introduction

Graphene is a single sheet of carbon atoms arranged in a honeycomb lattice [1–3]. Patterned graphene nanoribbons have been shown to support collective charge oscillations, i.e., plasmons [4]. Unlike in metals, the charge density in graphene can be modified by electrostatic gating or chemical doping, resulting in tunable plasmon resonances [5, 6]. Strong light confinement and frequency tunability are two important characteristics of graphene plasmons, which make them good candidates for the enhancement of photon fields in the mid-infrared to terahertz regions of the spectrum [7]. It has already been shown that plasmon resonances in graphene can couple strongly to substrate polar phonons [8, 9] and also to the intrinsic IR-active phonons of bilayer graphene [10]. A closely related, but yet unexplored problem is the interaction of plasmons in graphene with the extrinsic vibrational modes in adsorbed species. Indeed, the possibility of near-field enhancement of light-matter interactions by graphene plasmons has been predicted [7, 11]. However, an experimental demonstration of such a phenomenon is still lacking. The interaction between plasmons in noble metal nanoparticles and vibrational modes in molecules has long been used as an ultrasensitive probe for sensing small molecular concentrations [12–15], a fact that also motivates the current study.

In unpatterned graphene, the electromagnetic boundary conditions and Drude-

like conductivity [16] determine the plasmon frequency, which scales with the charge density (n) and the plasmon wave vector (q) as $\omega \propto n^{1/4}$ and $\omega \propto q^{1/2}$, respectively [17, 18]. In graphene nanoribbons and other forms of nanostructures, localized plasmons can be directly excited by incident light with zero in-plane momentum, and analogous dispersion relations can be obtained in the quasi-static limit [4], which is appropriate for structures much narrower than the incident light wavelength. These graphene plasmons have resonance frequencies which, depending on their size and doping, lie in the infrared or far-infrared range of the spectrum [10, 19]. Thus, the use of nanoribbons, or other forms of patterned graphene, allows for the efficient and selective coupling of infrared light to surface plasmon modes. In this work, we use infrared transmission spectroscopy to study the interaction of graphene plasmons with vibrational modes in surface-adsorbed thin polymer films. Poly(methyl methacrylate) (PMMA) is used as the adsorbates in these experiments, where it contains carbonyl (C=O) groups with vibrational frequencies around 1700 cm^{-1}, which is close to the plasmon resonance of our graphene nanoribbons.

7.1.2 Device Structures

The structure of the fabricated devices is shown in Fig. 7.1a. The nanoribbon array is defined by electron beam lithography and etching of graphene grown by chemical vapor deposition (CVD) (Figure 7.1b). Highly resistive silicon with a 280 nm thick surface oxide is used as the substrate that allows light transmission in the mid-infrared range. PMMA layers are spin-coated onto the nanoribbon-covered substrates. The thicknesses of these layers are determined by ellipsometry and controlled using PMMA solutions of different concentrations. Samples with PVP are also prepared by spin-coating, but the thickness of this film is further decreased by washing in copious amounts of water. This dissolves the portion of the polymer that is not in direct contact with the sample surface, leaving a PVP residue that is only 2-3 nm

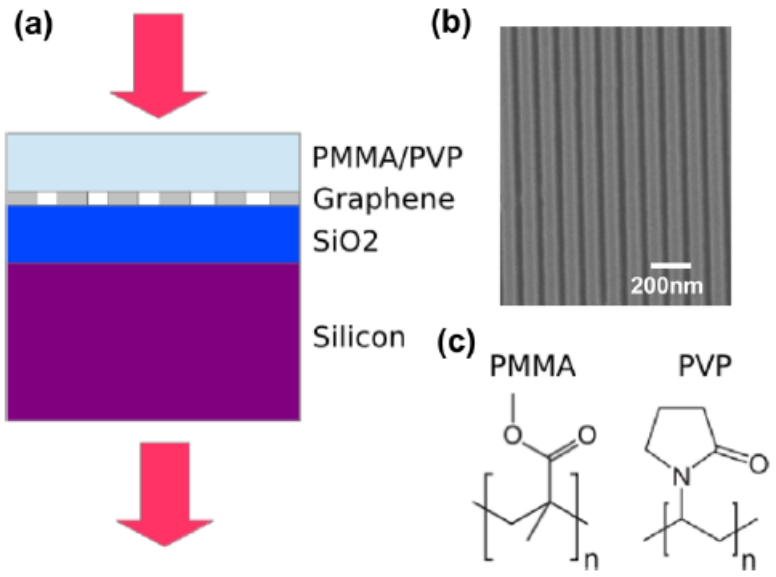

Figure 7.1: (a) Experimental arrangement. Spectroscopic measurements are conducted in the light transmission, as indicated by the arrows. The device is composed of a thin layer of PMMA or PVP, a graphene nanoribbon (GNR) array, and a 280 nm thick SiO_2 layer on top of a bulk Si substrate. (b) SEM image of graphene nanoribbons. (c) PMMA and PVP both contain the carbonyl double-bond (C=O), whose stretching mode has a vibrational frequency around 1700 cm^{-1}.

thick, as determined by height and phase-contrast AFM. The carbonyl-containing structures of PMMA and PVP are shown in Fig. 7.1c. IR spectra of these samples are collected in the transmission configuration using an IR microscope coupled to an FTIR spectrometer (Thermo Scientific Nicolet Continuum Infrared Microscope and Nicolet 8700 FTIR spectrometer). The attenuation of the transmission is defined as $A = 1 - T/T_0$ where T is the transmission spectrum with graphene nanoribbons and T_0 is the transmission spectrum of the same system without graphene nanoribbons. Enhancement of the vibrational absorption is observed in our experiment [20] even when there is only a partial overlap between the plasmon and vibrational frequencies. The localized plasmon frequency depends on the ribbon width W, $\omega \propto W^{-1/2}$, so by using graphene nanoribbons of different widths, the plasmon resonance can be tuned across the vibrational mode resonance.

7.1.3 FDTD Simulations

To understand the origin of the IR absorption enhancement, we performed finite-difference time-domain (FDTD) simulations for the device structures shown in Fig. 7.1a. The plasmon is excited in the nanoribbon by a plane wave whose frequency is in resonance with the plasmon, and periodic boundary conditions are used to simulate the array of nanoribbons. The conductivity of graphene is assumed to follow a Drude form. Furthermore, the DC conductivity and the scattering rate in the Drude form determine the resonance frequency and the width of the plasmon peaks, respectively. In general, the effectiveness of the plasmonic effects of a system is quantified by the quality factor Q given by $Q = -\operatorname{Re}\{\epsilon\}/\operatorname{Im}\{\epsilon\}$, where ϵ is the complex dielectric function of the plasmonic material. The local optical field intensity enhancement responsible for the increase in absorption is proportional to Q^2 (in Raman scattering $\propto Q^4$). It is therefore clear that the quality factor of the plasmonic resonance plays a very important role in the field enhancement and will be a func-

tion of frequency as different decay pathways (damping) may be involved at different energies [10, 17].

Due to the translational symmetry along the ribbons, we only simulated the electromagnetic field in a cross-section of the experimental structure. Periodic boundary conditions are used to simulate an array of nanoribbons with the spacing between the ribbons set equal to the width of the ribbons. The resolution of our simulation is set to be 0.5 nm due to limited computational power, and the thickness of the ribbons is set to 2 nm. The conductivity of the graphene layer is scaled to match its real thickness of $\sim$0.34 nm. We have verified that the transmission and reflection spectrum does not change if a denser grid is employed. We thus conclude that the density of the grid is sufficient for accurate simulation of the electromagnetic wave. The ribbons are excited by a plane wave whose frequency is in resonance with the plasmon. The simulation time is set to be long enough so that the system reaches steady state. The enhancement in the field intensity is obtained by taking the ratio of the electric field intensities (integrated over a period) with and without the nanoribbons at each spatial point. To simulate the conductivity of graphene, we used the Drude form $\sigma(\omega) = \sigma_0/(1 + i\omega/\gamma)$, where $\sigma_0 = 0.003\Omega^{-1}$ is the DC conductivity of graphene and γ is the scattering rate of charge carriers (Figure 7.2). The interband conductivity of graphene in the frequency range of our experiment is negligible due the Pauli blocking.

For continuous graphene, the plasmon dispersion relation (Eq. 7.1) is determined by the Maxwell equations at the boundary [17]. Here σ is the conductivity of graphene, ϵ_{r1} and ϵ_{r2} are the relative dielectric constants of the materials on the two sides of the 2D material, ϵ_0 is the vacuum permittivity, ω is the plasmon resonance frequency, β is the in-plane wave vector of the surface plasmon which is much larger than the wave vector in free space k_0.

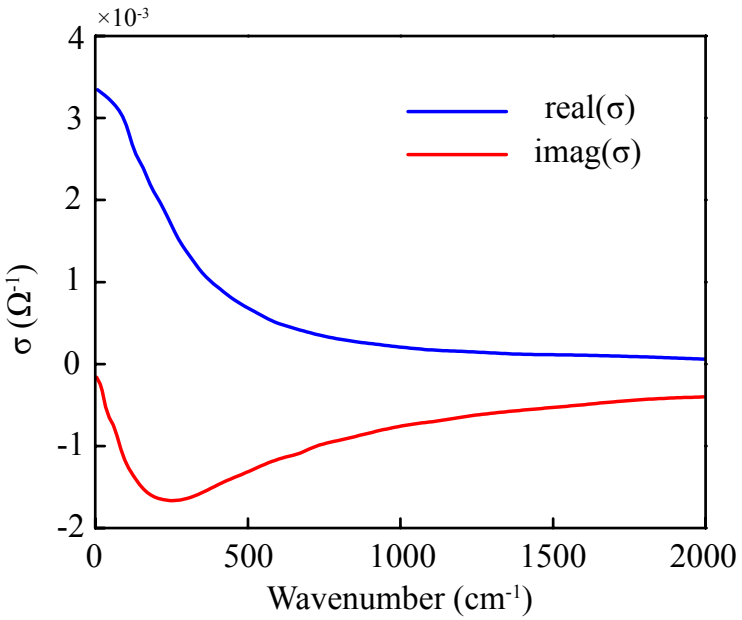

Figure 7.2: Drude conductivity used to model graphene's conductivity in the FIR to MIR range.

$$\frac{\epsilon_{r1}}{\sqrt{\beta^2 - \epsilon_{r1}k_0^2}} + \frac{\epsilon_{r2}}{\sqrt{\beta^2 - \epsilon_{r2}k_0^2}} = -\frac{i\sigma}{\epsilon_0\omega}. \tag{7.1}$$

In the frequency region where interband transitions are forbidden by Pauli blocking, the conductivity of graphene can be approximated by the Drude form where $\sigma \sim 1/\omega$, and thus

$$\omega \sim \sqrt{\frac{1}{\epsilon_{r1}} + \frac{1}{\epsilon_{r2}}}. \tag{7.2}$$

Using values $n_{\mathrm{SiO_2}} \approx n_{\mathrm{PMMA}} \approx 1.4$ [21], we obtain a shift in the plasmon resonance frequency of 18%.

7.1.4 Result and Discussion

In Fig. 7.3 we show results for two different plasmon widths (damping rates) $\gamma = 50cm^{-1}$ and $\gamma = 250cm^{-1}$. The enhancement in the field intensity is expressed by taking the ratio of the electric field intensities with and without the nanoribbons at each spatial point, $|E^2/E_0^2|$. As can be seen from the color-coded intensity map in Fig. 7.3, large enhancements in the field intensity can be generated (more than 3 orders of magnitude) near the edges of the nanoribbon and the field enhancement decays exponentially away from both the edges and the graphene surface. This enhancement in the local electric field is the source of the observed enhancement in the interaction between light and the carbonyl vibration in the polymer film. The enhancement can be potentially further increased through improved graphene sample quality (reduced plasmon damping), and by the use of stacked graphene layers [19]. These optimization procedures deserve further work but are beyond the scope of the present study. Figure 7.4 shows the simulated attenuation spectra of four graphene nanoribbon arrays (80, 90, 110, and 120 nm width) coated with 8 nm of PMMA. The plasmon attenuation peak intensity is normalized, and the vibration appears as a dip in Fig. 7.4. We observe that the vibrational attenuation increases as the de-

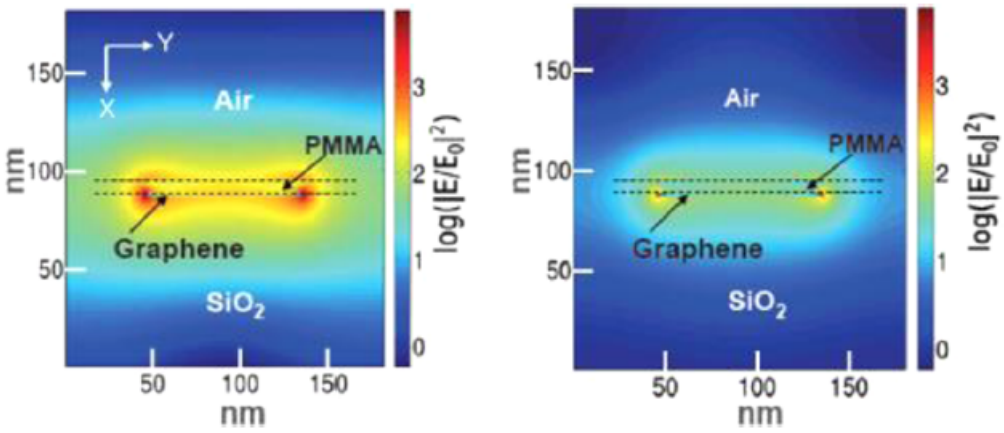

Figure 7.3: Spatial map of the enhancement of electric field intensity near a graphene nanoribbon both perpendicularly to the surface of the nanoribbon (X) and across the nanoribbon (Y). Finite-difference time-domain (FDTD) simulations of the field enhancement in the vicinity of the same nanoribbons for two values of plasmon damping, $\gamma = 50cm^{-1}$ (left) and $\gamma = 250cm^{-1}$ (right).

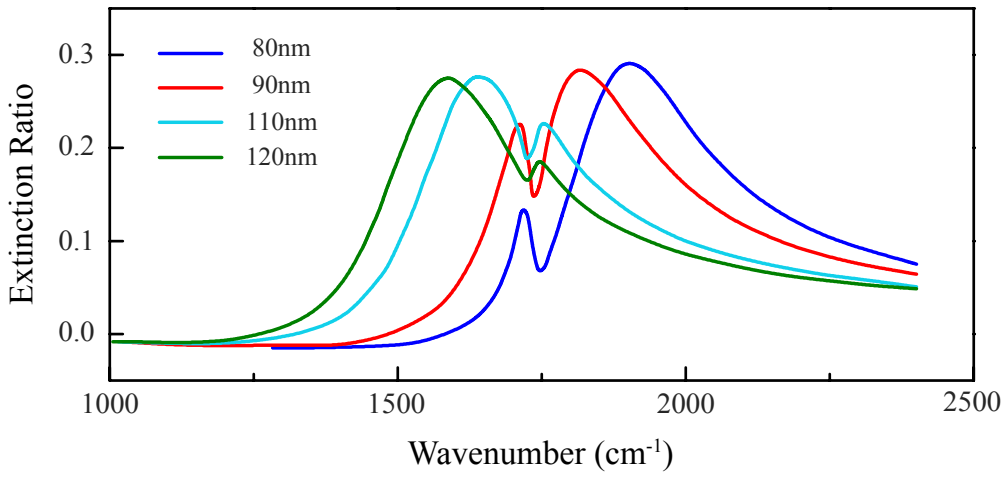

Figure 7.4: FDTD simulation for the graphene plasmon extinction spectra for different graphene nanoribbon widths. The changes in intensity, line shape, and the development of a transmission transparency near the 1750 cm^{-1} C=O vibration are due to the interaction of the graphene plasmon and the molecular vibration in PMMA.

tuning between plasmon and vibrational frequency decreases ($\Delta I \sim 1/\Delta f$), clearly demonstrating that the enhancement is a resonance effect.

In conclusion, we have demonstrated graphene plasmon enhanced vibrational sensing of surface-adsorbed polymers. The detection sensitivity increases by a factor of about 5 compare with device with no graphene, as evident from the height of the induced transparency in the IR attenuation spectra of the coupled plasmon-vibrational mode system. The modulation of the graphene plasmon attenuation spectrum by surface-adsorbed polymers is due to near-field electromagnetic coupling, as supported by FDTD simulations. The large magnitude of this modulation as compared to the absorption of the polymer film is caused by a strong enhancement in the near-field intensity. Furthermore, this plasmonic enhancement is confined to the vicinity of the surface, as the plasmon field decay length is measured to be $\sim$ 10 nm. Lastly, this vibration sensing technique exhibits molecular specificity; that is, different molecular compounds can be differentiated from the peak frequencies of the vibrational mode induced transparencies.

7.2 Dispersion Engineering

7.2.1 Introduction

There are increasing demands on optical interconnections to have high-bandwidth, low-latency, and low-power consumption [22]. Due to the technological advances and increased complexity in optical networks, high-quality connectivity for the optical network is critical. For example, the problem of pulse broadening due to chromatic dispersion is becoming an increasingly important factor for signal degradation. This problem becomes even more serious as the data transmission scales to higher rates [23]. Many techniques have been explored to compensate for interconnect dispersion so as to achieve high-data transmission rates across long-span-length optical-network

systems; these includes adding conformal dielectric overlayers to silicon waveguides [24] or using silicon strip/slot hybrid waveguides [25, 26]. In this section, we investigate in detail the dispersion properties of a silicon/plasmonics hybrid optical interconnect structure, which has the advantage of sending both electric and photonic signals along the same circuitry. This hybrid interconnect approach provides a natural "network-on-chip" platform, which is fully compatible with semiconductor fabrication techniques and which incorporates electric and photonic interconnects that achieve large capacity with low power losses [27, 28]. With an optimal design, this hybrid structure can provide a flat dispersion with zero dispersion at c-band communications wavelengths, which is significant for wavelength-division-multiplexed optical network systems [29].

7.2.2 Theory and Simulations

Our hybrid structure for optical interconnects consists of a high-refractive-index silicon nanowire separated from a plasmonic waveguide by a nanoscale low-refractive-index dielectric gap. At the 1.55μm communication wavelength, a standard waveguide mode is supported in the silicon nanowire, as shown in Fig. 7.5(a), while the surface plasmon polaritons (SPP) are supported by the metal-dielectric interfaces, as indicated in Fig. 7.5(b). For a hybrid structure, the coupling between the plasmonic and waveguide modes across the gap enables a 'gap-mode' that allows energy confinement and propagation through the low-index-gap region with a mode size that is much smaller than the diffraction limit. This gap mode, shown in Fig. 7.5(c), arises from the continuity of the displacement field at the material interface, thus a strong normal electric field component occurs in the gap. The low-index gap also leads to lower long-range SPP propagation loss compared to that obtainable with higher-index materials [30]. Thus, the photonic signals propagate over large distances with low losses. Due to the hybridization mechanism, the analysis in this paper is focused

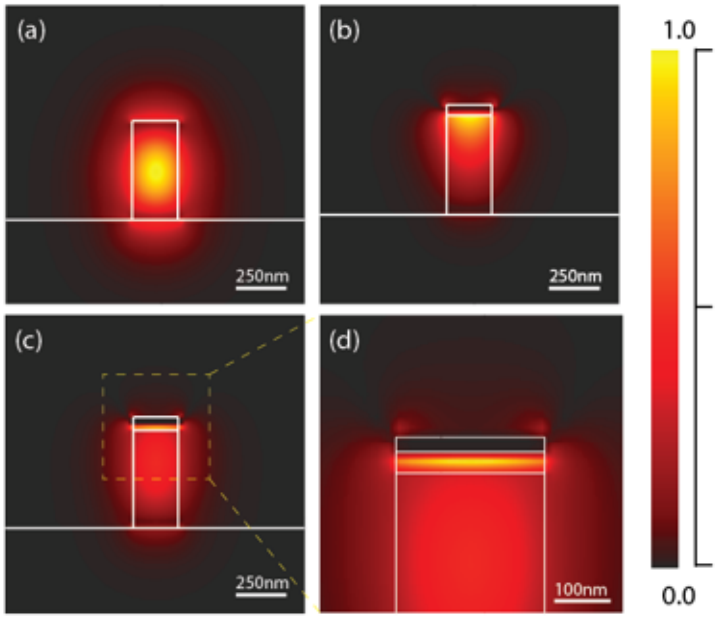

Figure 7.5: The mode profile at 1.55μm for (a) waveguide mode - a silicon waveguide on a SiO_2 substrate; (b) SPP mode - a Au plasmonic waveguide atop a silicon waveguide; (c) hybrid gap mode - with SiO_2 acting as a low dielectric spacer between plasmonic and silicon waveguides; (d) shows a zoom-in of the hybrid mode, which is confined mainly in the SiO_2 region.

upon the properties of the fundamental quasi-TM mode. Based on coupled-mode theory, the hybrid mode can be described as a superposition of the waveguide mode and the SPP mode,

$$\Psi = a\Psi_{si} + b\Psi_{spp} \tag{7.3}$$

where a and b are the amplitudes of the constituent waveguide $\Psi_{si} = [1\ 0]^T$ and SPP $\Psi_{spp} = [0\ 1]^T$ basis modes, respectively. The modes of the coupled system are characterized by the system of equations discussed in [30]

$$\begin{pmatrix} n_{si} & \kappa_{12} \\ \kappa_{21} & n_{spp} \end{pmatrix} \begin{pmatrix} a \\ b \end{pmatrix} = n_{eff} \begin{pmatrix} a \\ b \end{pmatrix} \tag{7.4}$$

where κ is the coupling strength between waveguide and SPP modes and n_{Si}, n_{spp} are the effective refractive indices of the silicon and SPP waveguides, respectively. The index parameter, n_{eff}, is the eigenvalue of this hybrid system, which quantifies the phase velocity of the direction of propagation.

The eigenmodes and effective indices of the hybrid nanostructure are computed using a full-vectorial finite-element mode solver (FemSim, RSoft) over a broad wavelength range. The dispersion properties of each material are automatically taken into considerations in our numerical simulations. The resulting raw effective-index data are fitted with a higher-order polynomial, in order to smooth out small numerical discontinuities introduced by the mode solver. The group velocity dispersion can be obtained according to [24]

$$D_\lambda = \frac{\lambda}{c_0} \frac{d^2 n_{eff}}{d\lambda^2} \tag{7.5}$$

where n_{eff} is the effective index of the structure at free-space wavelength λ and c_0 is the speed of light. Figure 7.6 plots the calculated GVD versus wavelength for different waveguides. The green (waveguide) curve shows the dispersion properties for the waveguide mode, which corresponds to a silicon waveguide placed on top of the SiO_2 substrate; the blue (SPP) curve shows the SPP-mode dispersion, in which a 40-nm-thick gold layer acting as a plasmonic waveguide is on top of the silicon waveguide,

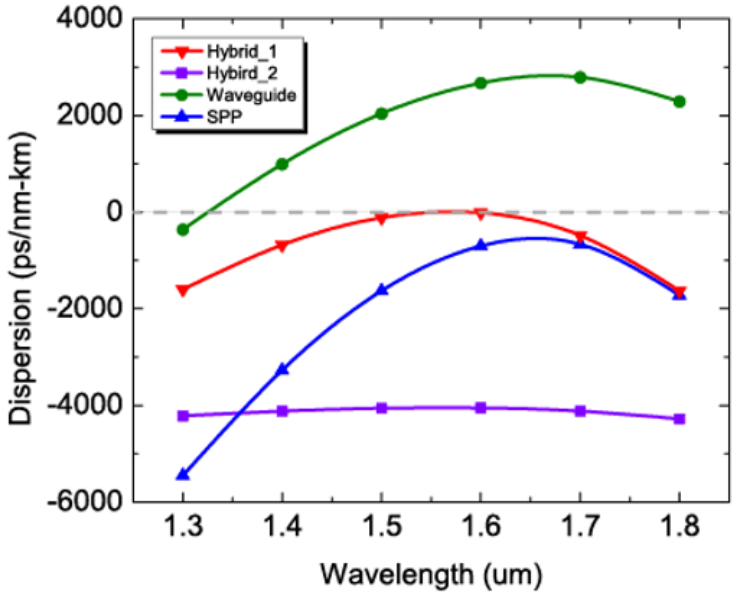

Figure 7.6: The dispersion properties for waveguide mode - silicon waveguide on SiO_2 substrate (green); SPP mode - Au plasmonic waveguide atop silicon waveguide (blue); and hybrid gap mode - with SiO_2 acting as a low-dielectric spacer between the plasmonic and silicon waveguides, where we tune the dimensions so that (i) zero-dispersion is at 1.55μm (red) and (ii) flat-dispersion across 1.3-1.8 μm.

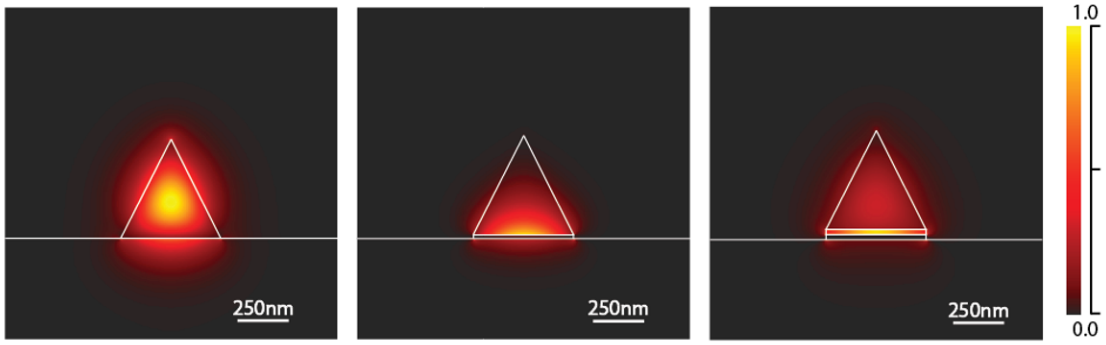

Figure 7.7: The mode profile at 1.55μm for (a) waveguide mode - triangular silicon waveguide on SiO_2 substrate; (b) SPP mode - with Au plasmonic waveguide beneath triangular silicon waveguide; (c) hybrid gap mode - with SiO_2 acting as a low dielectric spacer between plasmonic and triangular silicon waveguides.

where this plasmonic waveguide can also propagate electronic signals. The calculated dispersion of the first hybrid gap mode is demonstrated using the red (Hybrid_1) curve. Our results show that with proper dispersion-engineering, and interconnect of zero dispersion is found at the communications wavelength. For this particular waveguide, we use a 480nm × 440nm (height × width) silicon waveguide with 30-nm SiO2 gap, which has a propagation length over 120μm. We also demonstrated another hybrid gap mode in purple (Hybrid_2) curve, in which we have flat dispersion (i.e. 54ps/km-nm) across 1.3-1.8μm. This hybrid structure has a 300nm × 220nm (height × width) silicon waveguide with a 30-nm SiO_2 spacer and a propagation length of about 45μm. Furthermore, we also investigated other geometries such as the triangular silicon/plasmonics waveguide hybrid structure shown in Fig. 7.7. Our results suggest that a design wherein flat dispersion at zero dispersion rate may be achievable.

7.3 References

[1] K. S. Novoselov, A. K. Geim, S. Morozov, D. Jiang, M. Katsnelson, I. Grigorieva, S. Dubonos, and A. Firsov, "Two-dimensional gas of massless dirac fermions in graphene," *Nature (London)*, vol. 438, no. 7065, pp. 197–200, 2005.

[2] Y. Zhang, Y.-W. Tan, H. L. Stormer, and P. Kim, "Experimental observation of the quantum hall effect and berry's phase in graphene," *Nature (London)*, vol. 438, no. 7065, pp. 201–204, 2005.

[3] A. K. Geim and K. S. Novoselov, "The rise of graphene," *Nat. Mater.*, vol. 6, no. 3, pp. 183–191, 2007.

[4] L. Ju, B. Geng, J. Horng, C. Girit, M. Martin, Z. Hao, H. A. Bechtel, X. Liang,

A. Zettl, Y. R. Shen, *et al.*, "Graphene plasmonics for tunable terahertz metamaterials," *Nat. Nanotechnol.*, vol. 6, no. 10, pp. 630–634, 2011.

[5] Z. Fei, A. Rodin, G. Andreev, W. Bao, A. McLeod, M. Wagner, L. Zhang, Z. Zhao, M. Thiemens, G. Dominguez, *et al.*, "Gate-tuning of graphene plasmons revealed by infrared nano-imaging," *Nature (London)*, vol. 487, no. 7405, pp. 82–85, 2012.

[6] J. Chen, M. Badioli, P. Alonso-González, S. Thongrattanasiri, F. Huth, J. Osmond, M. Spasenović, A. Centeno, A. Pesquera, P. Godignon, *et al.*, "Optical nano-imaging of gate-tunable graphene plasmons," *Nature (London)*, vol. 487, no. 7405, pp. 77–81, 2012.

[7] F. H. Koppens, D. E. Chang, and F. J. García de Abajo, "Graphene plasmonics: a platform for strong light–matter interactions," *Nano Lett.*, vol. 11, no. 8, pp. 3370–3377, 2011.

[8] Z. Fei, G. O. Andreev, W. Bao, L. M. Zhang, A. S. McLeod, C. Wang, M. K. Stewart, Z. Zhao, G. Dominguez, M. Thiemens, *et al.*, "Infrared nanoscopy of dirac plasmons at the graphene–sio2 interface," *Nano Lett.*, vol. 11, no. 11, pp. 4701–4705, 2011.

[9] H. Yan, T. Low, W. Zhu, Y. Wu, M. Freitag, X. Li, F. Guinea, P. Avouris, and F. Xia, "Damping pathways of mid-infrared plasmons in graphene nanostructures," *Nat. Photon.*, vol. 7, no. 5, pp. 394–399, 2013.

[10] H. Yan, T. Low, F. Guinea, F. Xia, and P. Avouris, "Tunable phonon-induced transparency in bilayer graphene nanoribbons," *Nano Lett.*, vol. 14, no. 8, pp. 4581–4586, 2014.

[11] F. Liu and E. Cubukcu, "Tunable omnidirectional strong light-matter interactions mediated by graphene surface plasmons," *Phys. Rev. B*, vol. 88, no. 11, p. 115439, 2013.

[12] B. Luk'yanchuk, N. I. Zheludev, S. A. Maier, N. J. Halas, P. Nordlander, H. Giessen, and C. T. Chong, "The fano resonance in plasmonic nanostructures and metamaterials," *Nat. Mater.*, vol. 9, no. 9, pp. 707–715, 2010.

[13] R. Adato, A. A. Yanik, J. J. Amsden, D. L. Kaplan, F. G. Omenetto, M. K. Hong, S. Erramilli, and H. Altug, "Ultra-sensitive vibrational spectroscopy of protein monolayers with plasmonic nanoantenna arrays," *Proc. Natl. Acad. Sci. U.S.A.*, vol. 106, no. 46, pp. 19227–19232, 2009.

[14] F. Neubrech, A. Pucci, T. W. Cornelius, S. Karim, A. García-Etxarri, and J. Aizpurua, "Resonant plasmonic and vibrational coupling in a tailored nanoantenna for infrared detection," *Phys. Rev. Lett.*, vol. 101, no. 15, p. 157403, 2008.

[15] N. J. Halas, S. Lal, W.-S. Chang, S. Link, and P. Nordlander, "Plasmons in strongly coupled metallic nanostructures," *Chem. Rev.*, vol. 111, no. 6, pp. 3913–3961, 2011.

[16] J. Horng, C.-F. Chen, B. Geng, C. Girit, Y. Zhang, Z. Hao, H. A. Bechtel, M. Martin, A. Zettl, M. F. Crommie, *et al.*, "Drude conductivity of dirac fermions in graphene," *Phys. Rev. B*, vol. 83, no. 16, p. 165113, 2011.

[17] M. Jablan, H. Buljan, and M. Soljačić, "Plasmonics in graphene at infrared frequencies," *Phys. Rev. B*, vol. 80, no. 24, p. 245435, 2009.

[18] E. Hwang and S. D. Sarma, "Dielectric function, screening, and plasmons in two-dimensional graphene," *Phys. Rev. B*, vol. 75, no. 20, p. 205418, 2007.

[19] H. Yan, X. Li, B. Chandra, G. Tulevski, Y. Wu, M. Freitag, W. Zhu, P. Avouris, and F. Xia, "Tunable infrared plasmonic devices using graphene/insulator stacks," *Nat. Nanotechnol.*, vol. 7, no. 5, pp. 330–334, 2012.

[20] Y. Li, H. Yan, D. B. Farmer, X. Meng, W. Zhu, R. M. Osgood, T. F. Heinz, and P. Avouris, "Graphene plasmon enhanced vibrational sensing of surface-adsorbed layers," *Nano Lett.*, vol. 14, no. 3, pp. 1573–1577, 2014.

[21] S. N. Kasarova, N. G. Sultanova, C. D. Ivanov, and I. D. Nikolov, "Analysis of the dispersion of optical plastic materials," *Opt. Mater.*, vol. 29, no. 11, pp. 1481–1490, 2007.

[22] O. Liboiron-Ladouceur, "Efficient interconnection for modern computing systems," in *Frontiers in Optics*, pp. FTu1B–4, Optical Society of America, 2014.

[23] A. Mohan, N. P. Saranya, S. B. Johnson, and A. Sangeetha, "Compensation of dispersion in 5 gbps wdm system by using dcf," in *Green Computing Communication and Electrical Engineering (ICGCCEE), 2014 International Conference on*, pp. 1–5, IEEE, 2014.

[24] X. Liu, W. M. Green, X. Chen, I.-W. Hsieh, J. I. Dadap, Y. A. Vlasov, and R. M. Osgood Jr, "Conformal dielectric overlayers for engineering dispersion and effective nonlinearity of silicon nanophotonic wires," *Opt. Lett.*, vol. 33, no. 24, pp. 2889–2891, 2008.

[25] L. Zhang, Y. Yue, R. G. Beausoleil, and A. E. Willner, "Flattened dispersion in silicon slot waveguides," *Opt. Express*, vol. 18, no. 19, pp. 20529–20534, 2010.

[26] L. Zhang, Q. Lin, Y. Yue, Y. Yan, R. G. Beausoleil, and A. E. Willner, "Silicon waveguide with four zero-dispersion wavelengths and its application in on-chip octave-spanning supercontinuum generation," *Opt. Express*, vol. 20, no. 2, pp. 1685–1690, 2012.

[27] X. Meng, R. R. Grote, J. I. Dadap, N. C. Panoiu, and R. M. Osgood, "Engineering metal-nanoantennae/dye complexes for maximum fluorescence enhancement," *Opt. Express*, vol. 22, no. 18, pp. 22018–22030, 2014.

[28] M. Petracca, B. G. Lee, K. Bergman, and L. P. Carloni, "Design exploration of optical interconnection networks for chip multiprocessors," in *High Performance Interconnects, 2008. HOTI'08. 16th IEEE Symposium on*, pp. 31–40, IEEE, 2008.

[29] B. G. Lee, A. Biberman, P. Dong, M. Lipson, and K. Bergman, "All-optical comb switch for multiwavelength message routing in silicon photonic networks," *IEEE Photon. Technol. Lett.*, vol. 20, no. 10, pp. 767–769, 2008.

[30] R. F. Oulton, V. J. Sorger, D. Genov, D. Pile, and X. Zhang, "A hybrid plasmonic waveguide for subwavelength confinement and long-range propagation," *Nat. Photon.*, vol. 2, no. 8, pp. 496–500, 2008.

Appendix A

Journal Publications

1. **Xiang Meng**, Wencan Jin, Hao Yang, Jerry I. Dadap, Richard M. Osgood., Andrei Dolocan, Peter Sutter and Nicholas Camillone III. "Two-photon field enhancement at a nanoscopic probe tip/surface junction for spationtemporal-resolved photoemission." Optics Letters 42, no. 13 (2017): 2651-2654.

2. **Xiang Meng**, Shang Liu, Jerry I. Dadap, and Richard M. Osgood. "Photoluminescence Enhancement from a Single Silicon Vacancy Center in a Nanodiamond Crystal via Metal Nanoantennae." Physics Review Materirals 1, no. 1 (2017): 015202.

3. **Xiang Meng**, Richard R. Grote, Wencan Jin, Jerry I. Dadap, Nicolae C. Panoiu, and Richard M. Osgood. "Rigorous theoretical analysis of a surface-plasmon nanolaser with monolayer MoS 2 gain medium." Optics Letters 41, no. 11 (2016): 2636-2639.

4. **Xiang Meng**, Richard R. Grote, Jerry I. Dadap, Nicolae C. Panoiu, and Richard M. Osgood. "Engineering metal-nanoantennae/dye complexes for maximum fluorescence enhancement." Optics Express 22, no. 18 (2014): 22018-22030.

5. Li, Yilei, Hugen Yan, Damon B. Farmer, **Xiang Meng**, Wenjuan Zhu, Richard M. Osgood, Tony F. Heinz, and Phaedon Avouris. "Graphene plasmon enhanced vibrational sensing of surface-adsorbed layers." Nano Letters 14, no. 3 (2014): 1573-1577.

6. Hao Yang, **Xiang Meng**, and Richard M. Osgood. "Accurate numerical computation of surface polaritron dispersion in the presence of nonlocal permittivity." *in preparation.*

7. Asif Ahmed, **Xiang Meng**, Jerry I. Dadap, Ramy El-Ganainy, and Richard M. Osgood. "Analysis of Non-Hermitian Signal Amplification via Four Wave Mixing using FDTD method." *in preparation.*

Appendix B

Invited Talks and Presentations

1. **Xiang Meng**, "Nanophotonic applications for high-performance systems." School of Engineering and Applied Science, Columbia University, 2017.

2. **Xiang Meng**, "New advances in nanophotonic device physics." ACM International Conference on Nanoscale Computing and Communication, 2016.

3. **Xiang Meng**, "Emerging plasmonic applications explored with cluster parallel computing." IEEE Photonics North, 2015.

4. **Xiang Meng**, "Two-color assisted field enhancement for vacuum tunneling of a metallic-tip/substrate systems." IEEE Photonics North, 2015.

5. **Xiang Meng**, "Photoluminescence enhancement from a single nitrogen vacancy center in a nanodiamond crystal via metal nanoantennae." Engineering Graduate Student Council, Columbia University, 2014.

Appendix C

Conference Publications

1. **Xiang Meng**, Richard R. Grote, and Richard M. Osgood. "Optical Enhancement of Emission in Three Dimensional Arrays of Metal Nanoparticle Antennae and Quantum-Dot Emitters." In Laser Science, pp. LTh1J-4. Optical Society of America, 2012.

2. **Xiang Meng**, and N. D. Osgood. "Design of the system dynamics longitudinal analysis system: Quantifying the hidden trajectories of system dynamics models." In 30th International Conference of the System Dynamics Society, St. Gallen, Switzerland. 2012.

3. **Xiang Meng**, Richard R. Grote, Abe Wolcott, Jonathan S. Owen, and Richard M. Osgood. "Photoluminescence Enhancement from a Single Nitrogen Vacancy Center in a Nanodiamond Crystal via a Metal Nanoantenna." In Laser Science, pp. LTh3H-1. Optical Society of America, 2013.

4. **Xiang Meng**, Richard R. Grote, and Richard M. Osgood. "Engineering 3d metal nanoantenna for fluorescence enhancement." In CLEO: Applications and Technology, pp. JTu4A-55. Optical Society of America, 2013.

5. Grote, Richard R., **Xiang Meng**, Jeffrey B. Driscoll, Nicolae Panoiu, and Richard M. Osgood. "Design method for critically coupling into a weakly absorbing 1D photonic crystal cavity." In CLEO: Applications and Technology, pp. JTu4A-41. Optical Society of America, 2013.

6. Souhan, Brian, Richard R. Grote, Jeffrey B. Driscoll, **Xiang Meng**, and Richard M. Osgood. "Metal-Semiconductor-Metal Monolithic Silicon-Waveguide Photodiode Design and Analysis." In Frontiers in Optics, pp. FM3E-3. Optical Society of America, 2013.

7. **Xiang Meng**, Richard Grote, Jerry Dadap, and Richard Osgood. "Threshold Analysis in Monolayer Semiconductor Nanolaser by Surface Plasmon Enhancement." In Laser Science, pp. LTh3I-3. Optical Society of America, 2015.

8. **Xiang Meng**, Hao Yang, Jerry I. Dadap, Richard M. Osgood, and N. Camillone. "Two-color assisted field enhancement for vacuum tunneling of a metallic-tip/substrate systems." In Photonics North, 2015, pp. 1-1. IEEE, 2015.

9. **Xiang Meng**, Asif Ahmed, Jerry Dadap, Keren Bergman, and Richard Osgood. "Dispersion Engineering of Silicon/Plasmonics Hybrid Optical Interconnections." In Integrated Photonics Research, Silicon and Nanophotonics, pp. IW2A-2. Optical Society of America, 2015.

10. **Xiang Meng**, Richard Grote, Jerry I. Dadap, Richard M. Osgood, Nicolae Panoiu, Nick Camillone, and Deyu Lu. "Emerging plasmonic applications explored with cluster parallel computing." In Photonics North, 2015, pp. 1-1. IEEE, 2015.

11. **Xiang Meng**, Hao Yang, Richard R. Grote, Jerry I. Dadap, Nicolae C. Panoiu, and Richard M. Osgood. "Designer metal-nanoantennae/dye complexes for maximum fluorescence enhancement." In SPIE Nanoscience+ Engineering, pp. 95473B-95473B. International Society for Optics and Photonics, 2015.

12. **Xiang Meng**, Richard R. Grote, Jerry I. Dadap, and Richard M. Osgood. "Threshold Analysis in Plasmonic Nanolaser with Monolayer Semiconductor as

Gain Medium." In JSAP-OSA Joint Symposia, p. 15p-2D-3. Optical Society of America, 2015.

13. **Xiang Meng**, Jerry Dadap, Asif Ahmed, and Richard M. Osgood. "New Advances in Nanophotonic Device Physics." In Proceedings of the 3rd ACM International Conference on Nanoscale Computing and Communication, p. 22. ACM, 2016.

14. **Xiang Meng**, Wencan Jin, Jerry I. Dadap and Richard M. Osgood. "A rigorous theoretical analysis of a surface-plasmon-enhanced monolayer nanolaser." In Photonics North, IEEE, 2015.

15. Ahmed, Asif, **Xiang Meng**, Jerry I. Dadap, Ramy El-Ganainy, and Richard M. Osgood. "Non-Hermitian Parametric Amplification via Four Wave Mixing." In Frontiers in Optics, pp. FTu2D-4. Optical Society of America, 2016.

16. **Xiang Meng**, Jerry I. Dadap, Nick Camillone and Richard M. Osgood. "Plasmonic Enhancement for Two-Color Ultrafast Time-Resolved Photoemission." In JSAP-OSA Joint Symposia, p. 14a-C302-5. Optical Society of America, 2016.